



Mathematisch-Naturwissenschaftliche Fakultät  
Ernst-Moritz-Arndt-Universität Greifswald

Diplomarbeit

# **Magnetic resonance imaging as an instrument for temperature measurements during cancer treatment**

Silke Hey

6. Juli 2007

Gutachter:

PD. Dr. Ralf Schneider

Prof. Dr. Peter Wust, Universitätsklinikum Charité Berlin



# Contents

|          |                                                                                              |           |
|----------|----------------------------------------------------------------------------------------------|-----------|
| <b>1</b> | <b>Introduction</b>                                                                          | <b>7</b>  |
| <b>2</b> | <b>Basic physics</b>                                                                         | <b>9</b>  |
| 2.1      | Spin dynamics . . . . .                                                                      | 9         |
| 2.1.1    | Spins . . . . .                                                                              | 9         |
| 2.1.2    | External magnetic field . . . . .                                                            | 10        |
| 2.2      | Spatial encoding . . . . .                                                                   | 13        |
| 2.2.1    | Slice encoding . . . . .                                                                     | 13        |
| 2.2.2    | Frequency encoding . . . . .                                                                 | 14        |
| 2.2.3    | Phase encoding . . . . .                                                                     | 14        |
| 2.3      | Basic sequences . . . . .                                                                    | 15        |
| 2.3.1    | Spin echo . . . . .                                                                          | 15        |
| 2.3.2    | Gradient echo . . . . .                                                                      | 15        |
| 2.4      | Image reconstruction . . . . .                                                               | 17        |
| 2.5      | Influence of field inhomogeneities . . . . .                                                 | 19        |
| 2.5.1    | Slice selection . . . . .                                                                    | 19        |
| 2.5.2    | Frequency encoding . . . . .                                                                 | 20        |
| 2.5.3    | Phase encoding . . . . .                                                                     | 20        |
| 2.6      | Temperature measurements . . . . .                                                           | 21        |
| 2.6.1    | Molecular diffusion coefficient . . . . .                                                    | 21        |
| 2.6.2    | Longitudinal Relaxation time . . . . .                                                       | 22        |
| 2.6.3    | Proton resonance frequency shift . . . . .                                                   | 22        |
| 2.6.4    | Further methods . . . . .                                                                    | 23        |
| 2.7      | Analytical solutions of Laplace's equation for simple objects in an external field . . . . . | 24        |
| 2.7.1    | Derivation of Laplace's equation . . . . .                                                   | 24        |
| 2.7.2    | Solutions of Laplace's equation using Fourier transform . . . . .                            | 25        |
| 2.7.3    | Analytical solution for simple geometries . . . . .                                          | 26        |
| 2.8      | Magnetic field inhomogeneities and temperature measurements . . . . .                        | 27        |
| 2.9      | Subsumption . . . . .                                                                        | 30        |
| <b>3</b> | <b>Numerical techniques</b>                                                                  | <b>31</b> |
| 3.1      | Finite volumes . . . . .                                                                     | 31        |
| 3.1.1    | Generalization to three dimensions . . . . .                                                 | 33        |
| 3.1.2    | Boundary conditions . . . . .                                                                | 33        |
| 3.1.3    | Solution of the problem . . . . .                                                            | 34        |

|          |                                                                                                     |           |
|----------|-----------------------------------------------------------------------------------------------------|-----------|
| 3.1.4    | Comparison between analytical and numerical results . . . . .                                       | 36        |
| 3.2      | Fourier transformation . . . . .                                                                    | 39        |
| 3.2.1    | Comparison between analytical and numerical results . . . . .                                       | 39        |
| 3.3      | Comparison between fast Fourier transformation and finite volumes . . . .                           | 41        |
| 3.4      | Phase unwrapping algorithm . . . . .                                                                | 42        |
| 3.5      | Field maps . . . . .                                                                                | 49        |
| 3.6      | Correction algorithms . . . . .                                                                     | 50        |
| 3.6.1    | Correction in the frequency domain . . . . .                                                        | 51        |
| 3.6.2    | Correction in the spatial domain . . . . .                                                          | 53        |
| 3.7      | Comparison between different correction algorithms . . . . .                                        | 55        |
| 3.8      | Subsumption . . . . .                                                                               | 57        |
| <b>4</b> | <b>Experimental results</b>                                                                         | <b>59</b> |
| 4.1      | Experimental setup . . . . .                                                                        | 59        |
| 4.2      | Technical aspects . . . . .                                                                         | 60        |
| 4.2.1    | Signal-to-noise-ratio . . . . .                                                                     | 60        |
| 4.2.2    | Readout bandwidth . . . . .                                                                         | 62        |
| 4.2.3    | Different susceptibilities . . . . .                                                                | 64        |
| 4.3      | Evaluation of the imaging series . . . . .                                                          | 65        |
| 4.3.1    | Temperature dependency of the image artifacts . . . . .                                             | 65        |
| 4.3.2    | Influence of the image resolution on image artifacts and tempera-<br>ture information . . . . .     | 69        |
| 4.3.3    | Comparison between experimental acquired temperature maps and<br>temperature probes . . . . .       | 72        |
| 4.4      | Subsumption . . . . .                                                                               | 76        |
| <b>5</b> | <b>Results</b>                                                                                      | <b>77</b> |
| 5.1      | Comparison between numerical and experimental results . . . . .                                     | 77        |
| 5.1.1    | Magnetic field . . . . .                                                                            | 77        |
| 5.2      | Correction of temperature maps . . . . .                                                            | 79        |
| 5.2.1    | Validation of the correction algorithm . . . . .                                                    | 79        |
| 5.2.2    | Application to experimental data . . . . .                                                          | 82        |
| <b>6</b> | <b>Conclusions</b>                                                                                  | <b>85</b> |
| <b>A</b> | <b>Determination of the magnetic field at the position of the nucleus for simple<br/>geometries</b> | <b>87</b> |
| A.1      | Homogeneous sphere . . . . .                                                                        | 87        |
| A.2      | Homogeneous cylinder . . . . .                                                                      | 90        |
| <b>B</b> | <b>Gradients</b>                                                                                    | <b>95</b> |

# Zusammenfassung

Im Verlauf der letzten Jahre hat die Bedeutung der Magnetresonanztomographie (MRT) stark zugenommen. In der Diagnostik sowie zur Vorbereitung chirurgischer Eingriffe oder im Rahmen neuartiger Techniken wie funktioneller Bildgebung oder MR-Angiographie ist sie heute unentbehrlich geworden. Da die erreichbare Bildqualität in all diesen Verfahren durch Artefakte limitiert wird, steigt die Notwendigkeit effektiver Korrekturverfahren für diese Bildstörungen.

Auch in der Krebstherapie kann die MR-Bildgebung genutzt werden. So werden am Universitätsklinikum Charité in Berlin Patienten mit einer neuartigen Therapie, der Hyperthermie, behandelt, die durch gezielte Erwärmung des Tumors dessen Empfindlichkeit für Bestrahlung und Chemotherapie erhöhen soll. Zur besseren Kontrolle der dabei applizierten Energie wird der Temperaturverlauf während der Therapie mit Hilfe des MRT überwacht (MR-Thermometrie). Da ein Kompromiss zwischen einer möglichst hohen Endtemperatur im Tumorgebiet und dem Schutz des umliegenden gesunden Gewebes gefunden werden muss, sind exakte und störungsfreie Temperaturmessungen von großer Bedeutung. Leider treten auch hier Bildstörungen in Folge von Lufteinschlüssen auf und erfordern dringend eine Korrektur. Das Ziel dieser Arbeit ist es daher, die Ursachen und Auswirkungen dieser Bildartefakte zu untersuchen, wobei insbesondere die bei der MR-Thermometrie auftretenden Effekte berücksichtigt werden. Die hierbei gewonnenen Erkenntnisse werden anschließend zur Entwicklung von angepassten Korrekturverfahren für die MR-Thermometrie genutzt. Zu diesem Zweck werden analytische, numerische sowie experimentelle Verfahren angewandt, wobei letztere zur Validierung der entwickelten Korrekturmethode eingesetzt werden.



# 1 Introduction

During the last decade magnetic resonance imaging (MRI) has become a very important tool for medical diagnostics. Recent developments enable physicians to monitor important characteristics of the human body, such as the blood flow (MR angiography), brain activity (functional MRI) or the concentration of metabolites (MR spectroscopy). With the aid of these new methods MRI has become a basic instrument in other medical fields, like cancer therapy. Among many existing treatments hyperthermia is one of the most promising for certain cancer species. This method is based on local heating of cancer tissue up to a temperature of  $43^{\circ}\text{C}$  making it more susceptible to additive medical treatments like “chemo-therapy”. The use of radio-frequency allows for non-invasive heating being one advantage of this method. The success of this therapy mainly depends on the precision of the heating, both concerning the location and the achieved temperature. For this reason online temperature control is mandatory which can be accomplished using MRI (MR thermometry). At the university hospital Charité in Berlin patients are already treated with this procedure for several years with great success [44, 45, 15, 16, 14, 42]. Despite these encouraging results, the method is not free of challenges which have to be overcome to implement the technique as a standard tool for the clinical practice. One of these challenges is to deal with image distortions, which occur especially in the vicinity of air cavities such as the lungs or the intestinal and lead to disturbances in the acquired temperature maps (Fig. 1.1).

These image artifacts are also known from anatomic MR images of structures in the vicinity of metallic implants. Consequently, methods for artifact correction are of great interest and have thus been developed and studied for many applications. First studies date back to 1985 by Lüdeke et al [27] who discovered, that one key problem of distortion correction is related to the determination of the magnetic field inhomogeneities. Since that, these distortions have been tackled by several groups and solutions were proposed using a large variety of approaches [1, 7, 25, 4, 35, 36, 22, 23]. Nevertheless, only a few groups also applied the achieved results to experimental data to correct them [35]. Furthermore, most of them focus mainly on the correction of geometric distortions, and thus studies related to temperature measurements are rare [37].

In this context we combine the methods used so far and emphasise their applicability to MR thermometry. The focus will be on studying the causes of image artifacts with respect to their temperature dependence as well as the development of correction procedures for both geometrical image artifacts and related temperature deviations.

As a consequence this work combines numerical, analytical and experimental techniques leading to the following structure. The second chapter will give an overview over the ba-

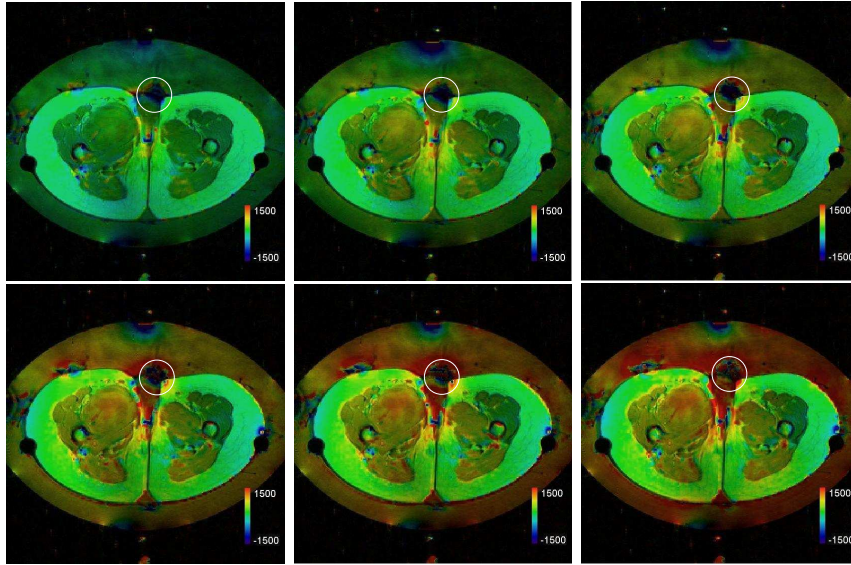


**Figure 1.1:** Time temperature series acquired at the university hospital Charité in Berlin during the EORTC study 62961. The images show a high grade soft tissue sarcoma in the right leg (left side in the picture). As can be seen, the encircled air-cavity leads to a false temperature calculation in its vicinity. This also disturbs the temperature control in the area nearby that is to be treated by heating it locally.

sis principles of magnetic resonance imaging, especially concerning the spatial encoding. Based on this, the influences of magnetic field inhomogeneities on the image restoration process are examined to find the causes of geometric image distortions. To validate the numerical algorithm, we solve analytically Laplace’s equation for simple geometries as a reference result. Furthermore, different methods for temperature measurements with MRI are presented and compared. Finally, the effects of magnetic field distortions on temperature measurements are analysed and used to derive a promising way to correct for these deviations. The third chapter deals with the basic numerical techniques which are applied in this work. Starting with a presentation of different numerical methods for the solution of Laplace’s equation focusing on finite volumes and Fourier transform this chapter also presents a self-developed unwrapping algorithm for phase images and two different geometrical correction algorithms. The analysis of the experimental data is the subject of the fourth chapter which also includes a discussion of the signal-to-noise-ratio of the acquired images. Additionally, the effect of an altered readout bandwidth on the image quality is examined and the susceptibility of a mixture used in the experiment is calculated. The fifth chapter presents the results obtained by combining experiment and numerical modelling concerning the magnetic field and temperature. Finally, we conclude by summarising the achieved results and proposing possible further applications and developments.



## 2 Basic physics

This chapter will provide the principles of magnetic resonance imaging. Thus, the influences of magnetic field inhomogeneities on the imaging process will be explained in detail. Afterwards, various methods for temperature measurements with MRI will be described and evaluated. Finally, a method for the correction of temperature maps in the presence of field deviations is presented.

### 2.1 Spin dynamics

#### 2.1.1 Spins

Basic quantum mechanics tells us that elementary particles like electrons, protons and neutrons possess, in addition to the classical known angular momentum, an intrinsic property called spin which is a quantity related to the symmetry of the particle with respect to rotations around its axis. As MRI mainly works with protons we will further concentrate on them. The z-component of the spin of a proton can only take the two distinct values  $s_z = +\frac{1}{2}$  and  $s_z = -\frac{1}{2}$  corresponding to “spin up” or “spin down”. This also corresponds to two different energy states in the hyperfine structure of the hydrogen atom divided only by an energy difference  $\Delta E$  on the order of  $\mu\text{eV}$  (Fig. 2.1 a). In thermal equilibrium<sup>1</sup> the distribution of spins within a sample can be described by the Boltzmann distribution

$$\frac{n_{\uparrow}}{n_{\downarrow}} = e^{-\frac{\Delta E}{kT}} \quad (2.1.1)$$

---

<sup>1</sup>The thermal equilibrium of a system defines a balanced state and is characterised by the minimum of a thermodynamic potential.

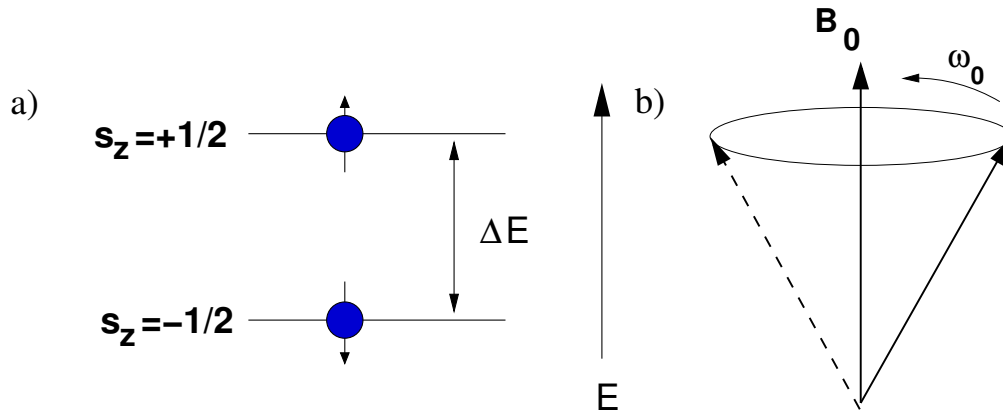


**Figure 2.1:** a) Energy states for a spin 1/2 system like hydrogen divided by an energy gap of  $\Delta E$ . b) Precession of a proton spin around the direction of an external magnetic field with the Larmor frequency  $\omega_0$ .

### 2.1.2 External magnetic field

If we apply an external homogeneous magnetic field  $\vec{B} = B_0 \vec{e}_z$ , for convenience into the  $z$  direction to a probe of protons, the spins will align along the direction of the magnetic field and precess with the Larmor frequency (Fig. 2.1 b)

$$\omega_0 = \gamma B_0, \quad (2.1.2)$$

where  $\gamma = 2.67522205 \cdot 10^{-8} \text{s}^{-1} \text{T}^{-1}$  denotes the gyromagnetic ratio of the proton. An additional high frequency pulse with the resonance frequency  $\omega_0$  will induce a transition between adjacent energy levels resulting in a spin flip (Fig. 2.2). Depending on the duration of this pulse the number of spin-flips in the sample increases leading to a change in the ratio between “spin up” and “spin down”.

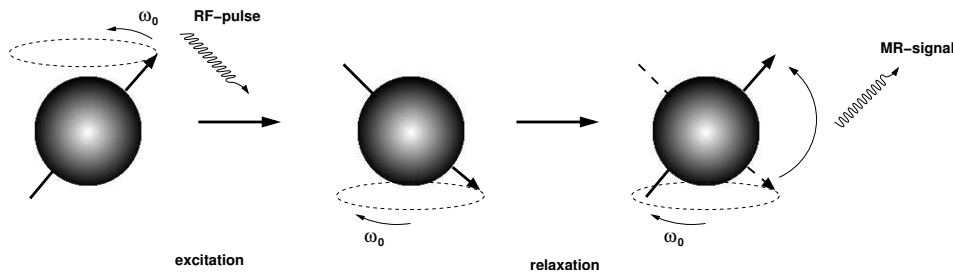


**Figure 2.2:** Principle of spin excitation. An applied RF-pulse induces a spin flip. After some time relaxation takes place leading to a change in magnetisation with time. This can be detected as an induced voltage which is the MR signal.

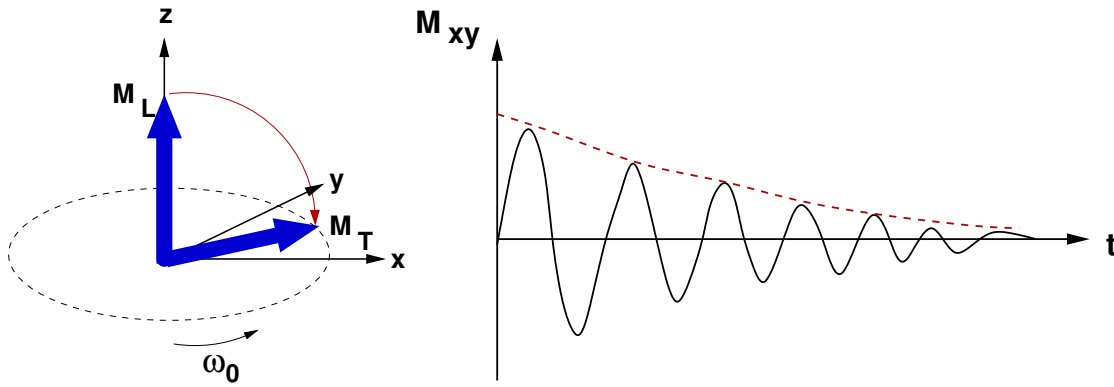


**Figure 2.3:** Effect of a high frequency pulse with resonance frequency  $\omega_0$ . The magnetisation vector  $M$  is switched into the  $xy$ -plane giving rise for a transverse magnetisation  $M_T$ . As relaxation takes place the transverse magnetisation decreases again which can be detected as a sinusoidal signal, the so-called free induction decay.

As a result the macroscopic magnetisation vector is turned from the  $z$ -direction into the  $xy$ -plane (Fig. 2.3), where the angle between the new direction of the magnetisation vector and the  $z$ -axis is called *flip angle*. After some time the longitudinal magnetisation will recover again. This process is influenced by two effects. Due to spin-lattice interactions the magnetisation vector will turn back into the  $z$ -direction reducing the transversal magnetisation (Fig. 2.4). Additionally the spins in the  $xy$ -plane are dephasing under the influence of spin-spin interactions (Fig. 2.5). Both effects are characterised by the *longitudinal relaxation time*  $T_1$  and the *transverse relaxation time*  $T_2$ , respectively. The resulting so-called *free induction decay* of the transverse magnetisation can be detected by the induction voltage in receiver coils nearby generating such the MR signal. As the strength of the signal depends on the excess of “spin up” to “spin down”, according to (2.1.1) this leads to a very weak signal. At room temperature this relation is close to one. Hence, the fraction of protons that remains for signal production is only in the order of  $10^{-6}$ .

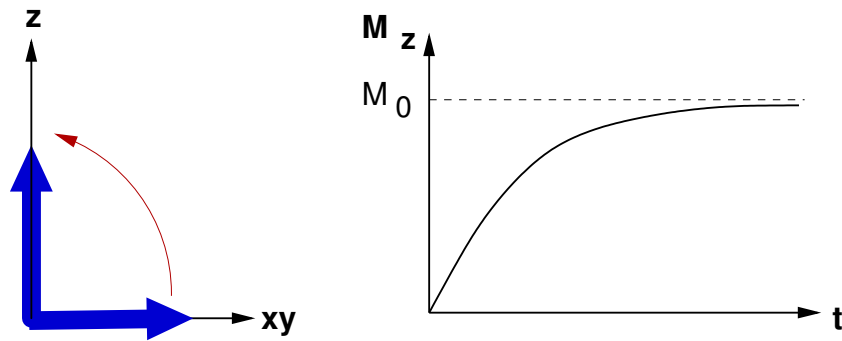


**Figure 2.4:** Interaction of the spin with its molecular neighbourhood increases the longitudinal magnetisation  $M_z$  again. This process is characterised by the longitudinal relaxation time  $T_1$ .

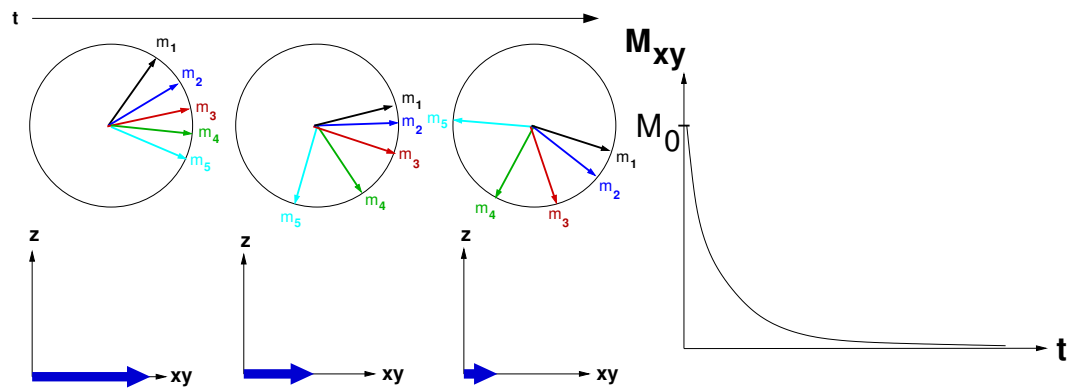


**Figure 2.5:** Spin-spin interactions result in a locally varying precession frequency which gives rise to a dephasing in the  $xy$ -plane. Here  $m_i$  denotes the magnetic moment of a single spin. This leads to a decreasing transverse magnetisation which is characterised by the transverse relaxation time  $T_2$ .

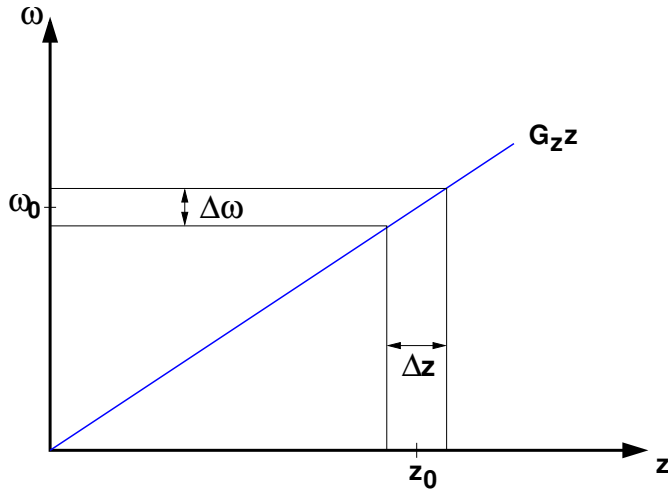


**Figure 2.6:** Principle of slice selection. A gradient  $G_z$  along the  $z$  direction changes the local magnetic field linearly. An applied RF-pulse with a certain bandwidth  $\Delta\omega$  will excite a slice with thickness  $\Delta z$ .

## 2.2 Spatial encoding

The described principle works very well. But how can we find out from where the signal originates? At this point we have to consider the local magnetic field structure which is the sum of a constant contribution  $B_0$  plus the gradient terms

$$\vec{G} = (G_x, G_y, G_z)^T = \left( \frac{\partial B_z}{\partial x}, \frac{\partial B_z}{\partial y}, \frac{\partial B_z}{\partial z} \right)^T. \quad (2.2.1)$$

Consequently, the local magnetic field is

$$\vec{B}(\vec{r}) = \left( B_0 + \vec{r} \cdot \vec{G}(\vec{r}, t) \right) \vec{e}_z. \quad (2.2.2)$$

The basic principle of spatial encoding [28] using these gradients is the subject of this section.

### 2.2.1 Slice encoding

If we do not want to excite the whole volume but only a single slice of the object we have to tailor the RF-pulse accordingly. With a suitable pulse it is possible to excite all spins precessing with a Larmor frequency  $\omega^*$  in the range  $\omega_0 - \Delta\omega/2 \leq \omega^* \leq \omega_0 + \Delta\omega/2$  where  $\Delta\omega$  denotes the bandwidth of the radio-frequency pulse. An additional linear gradient  $G_z$  along the  $z$ -direction changes the magnetic field locally. Thus, all spins precess with the changed Larmor frequency  $\omega^*$  corresponding to the new local magnetic field  $\vec{B} = B_0\vec{e}_z + G_z\vec{z}$ . Consequently, when the RF-pulse is applied only the spins in a slice of thickness  $\Delta z$  which precess with the right frequency are excited (Fig. 2.6).

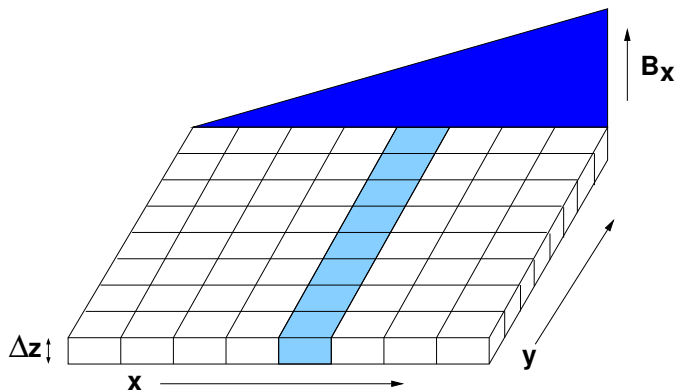


**Figure 2.7:** Principle of frequency encoding. A gradient along the x-axis changes the Larmor frequency of the spins dependent on their position along the readout direction.

## 2.2.2 Frequency encoding

After a slice has been chosen there is still no information available about the origin of the signal within the xy-plane. For this purpose an additional gradient  $G_x$  along the x-axis, generally denoted as the readout or frequency encoding direction, is applied (Fig. 2.7), leading to an altered magnetic field  $\vec{B} = B_0\vec{e}_z + G_x x \vec{e}_z$ . This changes the Larmor frequency of the spins in dependence of their position along the readout direction.

$$\omega(x) = \omega_0 + \gamma \int_0^{t_{\text{acq}}} G_x(\tau) x \, d\tau \quad (2.2.3)$$

Here  $t_{\text{acq}}$  denotes the acquisition time. Therefore, the measured signal contains a spectrum of frequencies which can be used to decode the exact position in one dimension by means of a Fourier transform.

## 2.2.3 Phase encoding

The position encoding along the y-axis, denoted as phase encoding direction, is accomplished by a third gradient  $G_y$  along this direction. The locally varying magnetic field  $\vec{B} = B_0\vec{e}_z + G_y y \vec{e}_z$  induces a spin dephasing which leads to a spatially varying phase for each spin. The resulting phase change depends on the duration of the gradient  $t_{\text{ph}}$

$$\Phi(y) = \Phi_0 + \int_0^{t_{\text{ph}}} G_y(\tau) y \, d\tau \quad (2.2.4)$$

with  $\Phi_0 = \omega_0 t_{\text{acq}}$ .

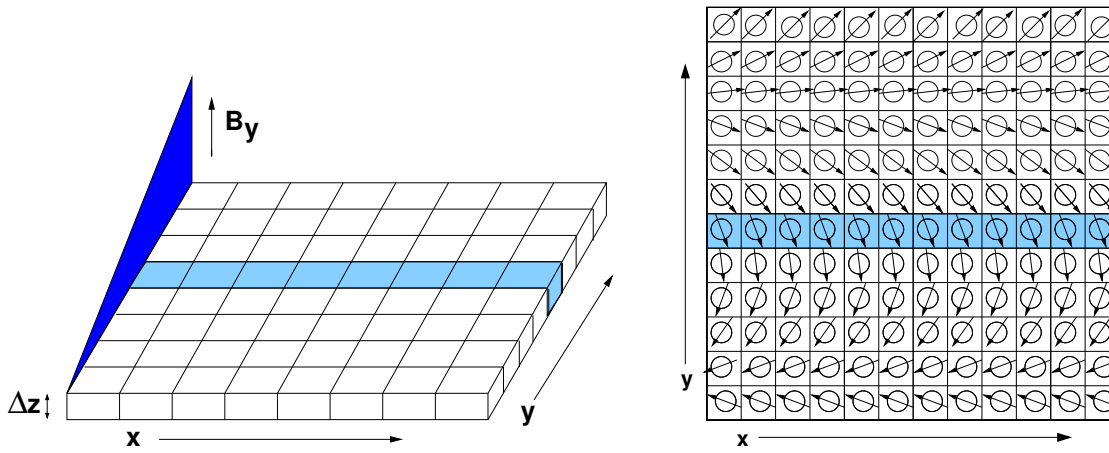


**Figure 2.8:** Principle of phase encoding. A gradient along the  $y$  axis causes a spin dephasing which results in a phase depending on the position of the spin along the phase encoding direction.

## 2.3 Basic sequences

### 2.3.1 Spin echo

Based on the results of Sect. (2.1) we now want to apply these basic concepts to image acquisition. The mentioned *free induction decay* (FID) gives a MR signal which however is relatively weak. Therefore, already in the middle of the last century another method for image acquisition based on a stimulated signal was implemented [17]. Figure 2.9 shows the basic scheme for the so called *spin echo sequence* (SE). The spins in a specific slice are excited by a RF-pulse of  $90^\circ$  which turns the magnetisation into the  $xy$ -plane. Now the usual relaxation effects take place reducing the transverse magnetisation. In contrast to the FID after half of the so-called *echo time*  $TE$  an  $180^\circ$  inversion pulse is applied which is equivalent of mirroring the magnetisation at the  $xy$ -plane. This pulse now has an interesting effect on the dephasing of the spins. It induces a re-phasing of the spins which finally leads to an echo at time  $TE$ . After the *acquisition time*  $TR$  the sequence is finished and can be started again.

Due to the mentioned  $180^\circ$  refocusing pulse all influences arising from local field inhomogeneities are also compensated which makes the spin echo sequence very robust against artifacts. One disadvantage is that it is very slow due to the number of applied RF-pulses.

### 2.3.2 Gradient echo

The search for a faster acquisition method led to the development of the *gradient echo sequence* (GE) which in contrast to the SE sequence does not include an inversion pulse (Fig. 2.10). Thus, a shorter acquisition time is achieved but on the other hand dephasing effects due to field inhomogeneities are not refocused at  $TE$  which leads to a higher sensitivity for artifacts. Another interesting consequence arising from the lack of refocusing is a non-vanishing signal phase which will be very important for this work.

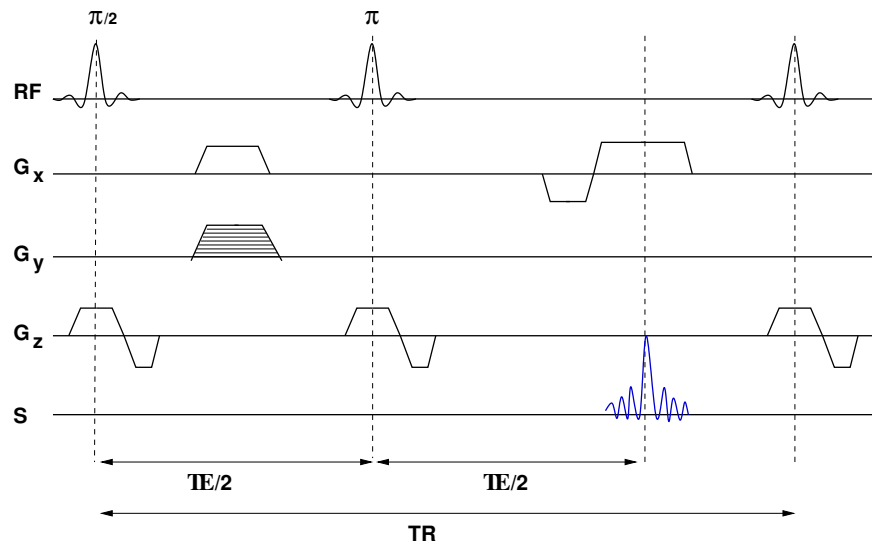


**Figure 2.9:** Diagram of the spin echo sequence. After a  $90^\circ$  excitation pulse (RF-pulse) a  $180^\circ$  inversion pulse at half of the echo time  $TE$  re-phases the spins inducing a spin echo (S) after the echo time  $TE$ . During the course of the sequence, slice encoding gradients  $G_z$ , phase encoding gradients  $G_y$  and readout gradients  $G_x$  are applied to ensure the correct spatial encoding. At the end of the acquisition time  $TR$  a new sequence starts.

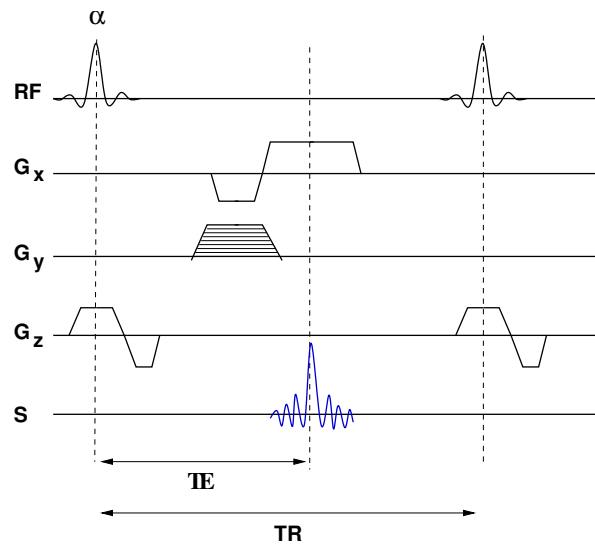


**Figure 2.10:** Diagram of the gradient echo sequence. After an excitation pulse (RF) with flip angle  $\alpha$  the echo at the echo time  $TE$  is induced by switching the gradients  $G_x$  in the readout direction. Again spatial encoding is accomplished by the gradients  $G_z$  and  $G_y$  in the slice encoding and the phase encoding direction, respectively. After the acquisition time  $TR$  a new sequence can start.



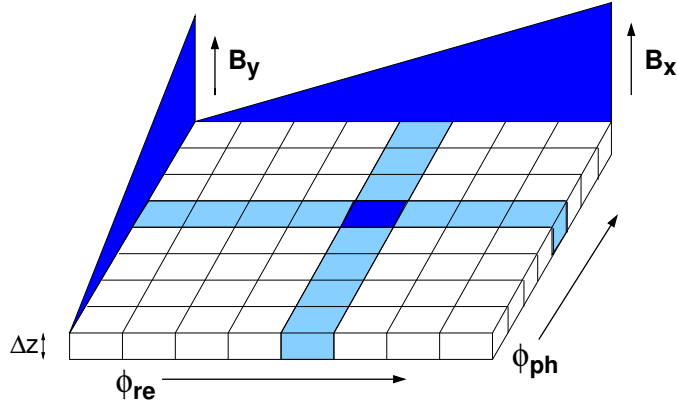


**Figure 2.11:** Due to the frequency and phase encoding gradients the spins in the image plane have position dependent phases.

## 2.4 Image reconstruction

For the case of a simple spin echo (2.3.1) and neglected relaxation effects at the moment of data acquisition the spins precess with spatially dependent phases  $\Phi_{\text{ph}}$  along the phase encoding and  $\Phi_{\text{re}}$  along the frequency encoding direction (Fig. 2.11):

$$\Phi_{\text{ph}} = \gamma \int_0^{t_{\text{ph}}} G_y(\tau) y \, d\tau$$

$$\Phi_{\text{re}} = \gamma \int_0^{t_{\text{acq}}} G_x(\tau) x \, d\tau$$

The resulting signal depends on the spatial magnetisation distribution  $m(x, y)$  and reads

$$M_T(t_{\text{acq}}, G_y) = \frac{1}{\sqrt{2\pi}} \int \int_{\text{slice}} m(x, y) e^{i\Phi_{\text{re}}} e^{i\Phi_{\text{ph}}} \, dx dy. \quad (2.4.1)$$

If we rewrite the phases as  $\Phi_{\text{re}} = k_x x$ ,  $\Phi_{\text{ph}} = k_y y$  it becomes obvious that they define the position within a frequency space with coordinates

$$k_x = \gamma \int_0^{t_{\text{acq}}} G_x(\tau) \, d\tau \quad , \quad k_y = \gamma \int_0^{t_{\text{ph}}} G_y(\tau) \, d\tau .$$

As these quantities have the dimension of an inverse length the largest appearing  $k$  values define the image resolution in the spatial domain

$$\Delta x = \frac{2\pi}{k_x^{\max}} \quad , \quad \Delta y = \frac{2\pi}{k_y^{\max}} \quad ,$$

where  $\Delta x$  and  $\Delta y$  denote the resolution in the x and y direction. In combination with the slice thickness  $\Delta z$ , which is influenced by the bandwidth of the RF-pulse and the slice selection gradient (2.2.1), the smallest resolvable volume element (“*voxel*”)  $\Delta V$  is given by

$$\Delta V = \Delta x \Delta y \Delta z . \quad (2.4.2)$$

On the other hand the image size is given by the smallest k values  $k_x^{\min}$  and  $k_y^{\min}$  and often denoted as the *field of view* (FOV)

$$FOV = N_x \Delta x N_y \Delta y , \quad (2.4.3)$$

where we have assumed a 2D image consisting of  $N_x$  pixels in the x- and  $N_y$  pixels in the y-direction. Finally, the required complex image of a slice in the spatial domain can be obtained as the result of a simple two dimensional Fourier transform.

$$m(x, y) = \frac{1}{\sqrt{2\pi}} \int \int M_T(k_x, k_y) e^{-ik_x x} e^{-ik_y y} dk_x dk_y . \quad (2.4.4)$$

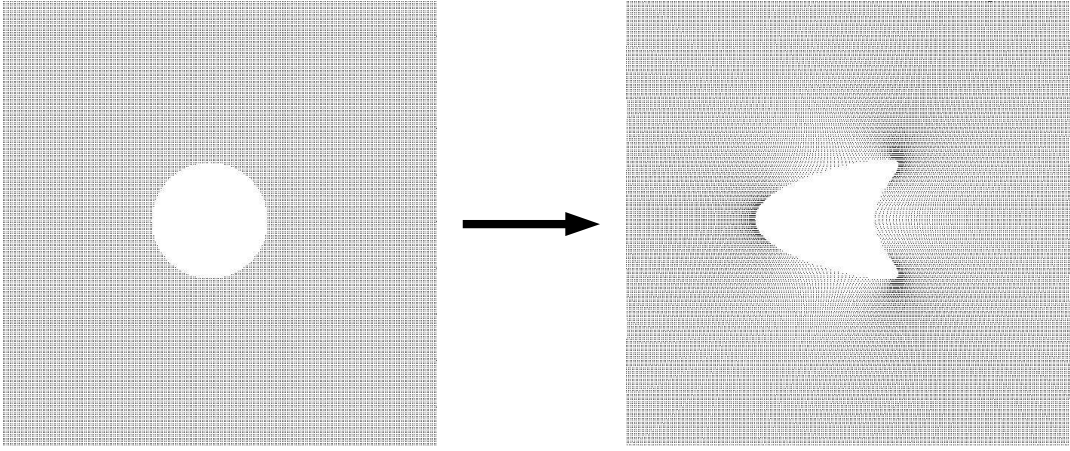


**Figure 2.12:** Simulation of the distortion of the MR image by a circle of susceptibility  $\chi_i = -100 \cdot 10^{-6}$  in a medium of susceptibility  $\chi_e = 0$  on a grid with  $256 \times 256$  data points.

## 2.5 Influence of field inhomogeneities

The spatial encoding as outlined in Sect. (2.2) is only valid for the ideal case of an entirely homogeneous main magnetic field  $B_0$  and linear gradients. This is never the case because for the neglect of eddy currents (2.2.2) does not fulfil the Maxwell equation  $\vec{\nabla} \times \vec{B} = 0$  which always introduces some problems due to gradient non-linearities [21]. Additionally every object that is brought into the area of the main magnetic field leads to local field changes. Usually a calibration prior to the measurement (“shimming”) removes deviations down to  $10^{-6}$  T which is sufficient for the imaging process. However in the case of magnetic materials or air, larger field deviations remain, leading to sometimes severe image distortions (Fig. 2.12).

During the spatial encoding magnetic field inhomogeneities  $\Delta B$  have a similar effect as the gradients and lead to locally changing precession frequencies of the spins. Because  $\Delta B \ll B_0$  holds for these field deviations,  $\Delta B$  can be regarded as only having a  $z$ -component. As the scanner cannot distinguish between the effects of gradients and field inhomogeneities this results in false spatial encoding [27, 35].

### 2.5.1 Slice selection

If a slice at position  $z = z_0$  is to be selected a gradient field  $(z - z_0)G_z$  is applied. As a result a RF-pulse with carrier frequency  $\omega_0$  and bandwidth  $\Delta\omega$  excites all spins which satisfy the equation

$$\omega_0 - \Delta\omega \leq \omega^* \leq \omega_0 + \Delta\omega \quad \text{with} \quad \omega^* = \gamma(B_0 + (z - z_0)G_z). \quad (2.5.1)$$

In the presence of field inhomogeneities  $\Delta B$  this condition changes accordingly

$$\omega'_0 - \Delta\omega \leq (\omega^*)' \leq \omega'_0 + \Delta\omega \quad \text{with} \quad (\omega^*)' = \gamma (B_0 + \Delta B + (z' - z_0)G_z) . \quad (2.5.2)$$

Consequently all voxels  $z'$  with

$$z_0 - \frac{\Delta\omega}{\gamma G_z} \leq z' + \frac{\Delta B}{G_z} \leq z_0 + \frac{\Delta\omega}{\gamma G_z} \quad (2.5.3)$$

are influenced by the excitation pulse leading to a voxel shift

$$\Delta z = \frac{\Delta B}{G_z} . \quad (2.5.4)$$

### 2.5.2 Frequency encoding

To find the voxel position along the readout direction  $x$  a gradient is applied, which leads to the modified magnetic field

$$B_z = B_0 + xG_x .$$

An additional inhomogeneity  $\Delta B$  changes the Larmor frequency of a spin at position  $x_0$  according to

$$\omega'_0 = \gamma (B_0 + \Delta B + x_0 G_x) . \quad (2.5.5)$$

Consequently it will be assigned to a position  $x'$  which fulfils the resonance condition

$$\omega'_0 = \gamma (B_0 + x' G_x) .$$

The result is a voxel shift

$$\Delta x = \frac{\Delta B}{G_x} . \quad (2.5.6)$$

### 2.5.3 Phase encoding

In a spin echo sequence (2.3.1) the dephasing effects of magnetic field inhomogeneities are refocused by the  $180^\circ$  pulse. Therefore, there is no effect on the phase encoding.

As in a gradient echo sequence there is no refocusing pulse, the effects of the field deviations accumulate during the acquisition. As a result the phase after echo time  $TE$  reads

$$\Phi = \Phi_0 + \gamma \Delta B TE . \quad (2.5.7)$$

This has several consequences. If the phases of the spins within one voxel add to zero (intra-voxel dephasing) no signal from this voxel can be detected. As a result, in addition to the already mentioned geometrical shift, gradient echo images show flower-like distortions close to susceptibility boundaries (Fig. 2.13).

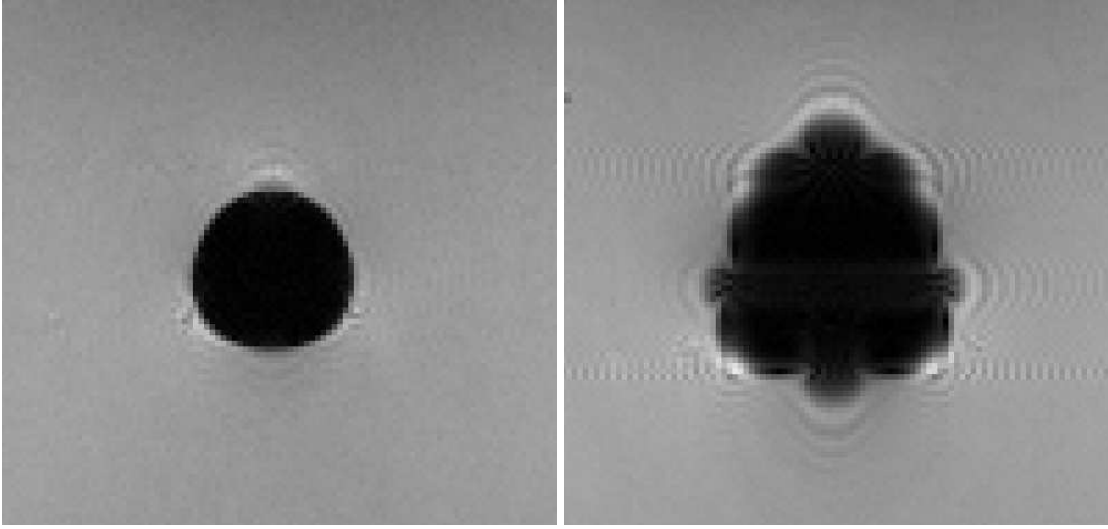


**Figure 2.13:** Left: GE double echo image of an air-filled cylinder ( $\chi = 0.38 \cdot 10^{-6}$ ) with high bandwidth (TR=600ms,  $TE = (3.77/10.8)$ ms, 10 slices à 5.5mm, FOV=(280×192)mm<sup>2</sup>, BW=930 Hz/pixel); Right: GE double echo image of a cylinder filled with contrast agent Magnevist ( $\chi \approx 3.6 \cdot 10^{-5}$ ) with low bandwidth (TR=600ms,  $TE = (3.77/10.8)$ ms, 10 slices à 5.5mm, FOV=(280×192)mm<sup>2</sup>, BW=260 Hz/pixel). In the right image the susceptibility difference leads to both geometric distortions as well as signal cancellation due to intra-voxel dephasing.

## 2.6 Temperature measurements

In addition to the possibility of getting information about the relaxation properties of the tissue in the human body, the MR signal also contains information about several other quantities. As an example, many parameters in MR imaging are temperature dependent and can be used for measurements [8]:

- diffusion coefficient
- longitudinal relaxation time  $T_1$
- proton resonance frequency

### 2.6.1 Molecular diffusion coefficient

The molecular diffusion coefficient  $D$  is known to change with temperature, as

$$D \sim e^{-E_a/kT}, \quad (2.6.1)$$

which leads to the following temperature dependence

$$\frac{1}{D} \frac{dD}{dT} = \frac{E_a}{kT^2}. \quad (2.6.2)$$

The activation energy  $E_a$  is relatively high, about 0.2 eV, resulting in a high sensitivity of 2.4 %/°C over a large temperature range [6]. Despite this good resolution, the applicability of this method is limited [3]. Membranes and other structures influence the diffusion of water in the body. Furthermore, the mobility of the water molecules strongly depends on the temperature and is direction-dependent. Therefore, for a complete description the full diffusion tensor has to be known. As the diffusion coefficient is strongly influenced by microcirculation of blood it is very difficult to extract the effect of temperature. Finally, this method is very sensitive to motion because it is based on the measurement of diffusional displacements between successive scans. Absolute temperature measurements are theoretically possible by acquiring several images with varying diffusion weighting constant in the sequence to calculate the exact value of  $D$  with a multi-point fit. In the human body this is not applicable because important characteristic parameters like the strength of the blood flow and the temperature dependence of the tissue perfusion are not known and differ from person to person.

### 2.6.2 Longitudinal Relaxation time

Similar to the diffusion coefficient the longitudinal relaxation time  $T_1$  shows the temperature dependence

$$T_1 \sim e^{-E_a/kT} \quad (2.6.3)$$

with an activation energy  $E_a$  in the range of 0.6 to 1.5 eV. Hence the temperature dependence of  $D$  is approximately linear with a sensitivity of (0.8-2.0)%/°C [29, 18] which is slightly lower than for the diffusional case. Even though  $T_1$ -weighted images are easily acquired the direct measurement of longitudinal relaxation times is difficult and requires multiple measurements and fast gradient software to acquire  $T_1$  as a result of a fit. Recently also faster sequences with higher accuracy like the TOMROP sequence (T One by Multiple Read Out Pulse) have been applied to this case [43]. Once carried out this method allows for absolute temperature measurements in phantoms. Nevertheless the  $T_1$  method has some disadvantages. Namely, the longitudinal relaxation time is tissue dependent and also changes strongly if coagulation occurs. Additionally its accuracy decreases with growing field strength and it is very sensitive to motion and susceptibility artifacts. For this reasons absolute temperature measurements in the human body are difficult because even small displacements lead to artifacts due to the tissue dependence of  $T_1$ .

### 2.6.3 Proton resonance frequency shift

The screening constant due to orbital electrons of the atoms increases with temperature, leading to a decrease in the local magnetic field and hence to a shift in the proton resonance frequency (PRF) of water. Up to 50°C, the PRF varies linearly with a temperature sensitivity of  $\frac{\partial\delta(T)}{\partial T}$  of 0.0107 ppm°K<sup>-1</sup> in pure water [19] and 0.007 to 0.009 ppm°K<sup>-1</sup> in muscle and other tissues. The PRF of fat is shown to be approximately independent

of temperature. Furthermore, the temperature dependent screening  $\sigma$  has an effect on the image phase

$$\begin{aligned}\Phi &= -\gamma B_0 \sigma(T) \mathbf{IE} \\ &= \gamma B_0 \left( -\sigma_0 - \frac{\partial \delta(T)}{\partial T} \cdot T \right) \mathbf{IE} .\end{aligned}\quad (2.6.4)$$

As  $\sigma_0$  is usually not known two phase images are subtracted to yield the temperature change compared to a reference image. Secondly, also phase changes due to field inhomogeneities are removed.

$$\Delta T = -\frac{\Phi_T - \Phi_{\text{ref}}}{\gamma B_0 \frac{\partial \delta}{\partial T}} .\quad (2.6.5)$$

Apart from the fact that it is only possible to measure temperature differences the PRF method shows high accuracy and is easy to implement. Usually a gradient echo image with enabled phase image is acquired before and after heating. After subtracting the phase values the temperature change is extracted applying (2.6.5). Nevertheless, this approach still leaves unsolved problems. For example, the velocity of the high frequency field depends on the temperature of the medium leading to phase and temperature disturbances in areas of high temperature gradients. Hence, one improvement of the method is the use of a double echo sequence which allows to remove disturbing effects which are not dependent on the echo time [14]. This approach works in all tissues and is not influenced by alterations like necrosis caused by coagulation. Of course, the use of GE sequences makes this method very sensitive to susceptibility artifacts. Even though the effects on the phase are eliminated by the subtraction, signal void and pixel displacements are always a problem.

Nevertheless for the application in hyperthermia treatment covering a temperature range up to  $43^\circ\text{C}$  and the necessity for high accuracy the PRF method is the best choice [43, 3, 34] and will therefore be applied in this work.

#### 2.6.4 Further methods

**MR-spectroscopy** Via MR-spectroscopy it is possible to measure the proton resonance frequency shift directly enabling an absolute temperature measurement. Unfortunately the measured shift depends on the ratio between water and fat within the pixel. As this is difficult to determine, the applicability of this method is rather limited.

**Temperature sensitive contrast agents** Recently, contrast agents have been developed which are temperature sensitive either due to incorporated temperature sensitive liposomes or because of their intrinsic magnetic properties that lead to a temperature induced transition from the diamagnetic to the paramagnetic state [13, 2]. Even though this ansatz seems to be very promising the strong nonlinear temperature dependence is one disadvantage that has to be solved first.

## 2.7 Analytical solutions of Laplace's equation for simple objects in an external field

According to Sect. (2.5) the correction of geometrical distortions requires the knowledge of the local magnetic field. For this reason we first have to derive a basic formalism from where we can start to calculate the magnetic field by means of analytical or numerical methods.

### 2.7.1 Derivation of Laplace's equation

The magnetic field at the location of the nucleus is determined by three components

$$\vec{B}_{\text{nuc}}(\vec{r}) = \vec{B}_{\text{ext}}(\vec{r}) + \vec{B}_{\text{scr}}(\vec{r}) + \vec{B}_{\text{lor}}(\vec{r}). \quad (2.7.1)$$

- $\vec{B}_{\text{ext}}(\vec{r})$ : external magnetic field in medium of susceptibility  $\chi(\vec{r})$

$$\vec{B}_{\text{ext}}(\vec{r}) = \mu_0 (1 + \chi(\vec{r})) \left( \vec{H}_0(\vec{r}) + \vec{h}_{\text{in}}(\vec{r}) + \vec{h}_{\text{obj}}(\vec{r}) \right) \quad (2.7.2)$$

$\vec{H}_0(\vec{r})$ : homogeneous main field,  $\vec{H}_0(\vec{r}) = (H_0, 0, 0)$

$\vec{h}_{\text{in}}(\vec{r})$  magnetic field inhomogeneities

$\vec{h}_{\text{obj}}(\vec{r})$  demagnetising field of the object

- $\vec{B}_{\text{scr}}(\vec{r})$ : screening by the orbital electrons

$$\vec{B}_{\text{scr}}(\vec{r}) = -\sigma \vec{B}_{\text{ext}}(\vec{r}) \quad (2.7.3)$$

$\sigma$  is the screening coefficient.

- $\vec{B}_{\text{lor}}(\vec{r})$ : effect of the sphere of Lorentz [26, 12, 9]. This term accounts for the fact that it is not possible to assume a continuous medium, as done in Maxwell's equations, while thinking microscopically. Rather, the existence of discrete atoms and molecules has to be considered. For this purpose the nucleus is placed inside an imaginary sphere where coincidental magnetic fluctuations lead to an effective zero susceptibility. The resulting magnetic field shift is given by

$$\vec{B}_{\text{lor}}(\vec{r}) = -\frac{2}{3}\chi(\vec{r})\vec{B}_{\text{ext}}(\vec{r}). \quad (2.7.4)$$

Combining the given quantities we get the resulting magnetic field at the location of the nucleus.

$$\begin{aligned} \vec{B}_{\text{nuc}}(\vec{r}) &= \left( 1 - \sigma - \frac{2}{3}\chi(\vec{r}) \right) \vec{B}_{\text{ext}}(\vec{r}) \\ &= \mu_0 (1 + \chi(\vec{r})) \left( 1 - \sigma - \frac{2}{3}\chi(\vec{r}) \right) \vec{H}_{\text{ext}}(\vec{r}). \end{aligned}$$



As  $\chi(\vec{r})$  is a small quantity and  $\vec{h}_{\text{in}}(\vec{r}), \vec{h}_{\text{obj}}(\vec{r}) \ll B_0$  we can neglect higher order terms. The same argument holds for the transverse components of the magnetic field. Hence, we can assume  $B_{\text{nuc}} \approx B_{\text{nuc},z}$ .

$$\begin{aligned} B_{\text{nuc}} &\approx B_{\text{nuc},z} \approx \mu_0 H_0 \left( 1 - \sigma + \frac{1}{3} \chi(\vec{r}) \right) + \mu_0 h_{\text{in},z} + \mu_0 h_{\text{obj},z} \\ &\approx B_0 \left( 1 - \sigma + \frac{1}{3} \chi(\vec{r}) \right) + b_{\text{in},z} + b_{\text{obj},z}. \end{aligned} \quad (2.7.5)$$

From classical electrodynamics [21] we know  $\vec{\nabla} \times \vec{H}(\vec{r}) = \vec{j}(\vec{r})$ . As we do not use strong gradients in our measurements, we can neglect eddy currents in our derivations. Consequently, we can define a scalar magnetostatic potential for which  $\vec{H}(\vec{r}) = -\vec{\nabla} \cdot \Phi$  holds. Maxwell's equations also contain the following expressions

$$\begin{aligned} \vec{\nabla} \cdot \vec{B}_{\text{ext}}(\vec{r}) &= \mu_0 \vec{\nabla} \cdot \left( (1 + \chi(\vec{r})) \vec{H}(\vec{r}) \right) = -\mu_0 \vec{\nabla} \cdot \left( (1 + \chi(\vec{r})) \vec{\nabla} \cdot \Phi(\vec{r}) \right) = 0 \\ \implies \vec{\nabla} \cdot \chi(\vec{r}) \vec{\nabla} \cdot \Phi(\vec{r}) &+ (1 + \chi(\vec{r})) \vec{\nabla}^2 \cdot \Phi(\vec{r}) = 0. \end{aligned} \quad (2.7.6)$$

Now the magnetostatic potential can be found by just adding the different contributions

$$\Phi = \Phi_0 + \Phi_{\text{in}} + \Phi_{\text{obj}} \quad \text{with} \quad \Phi_0 = -H_0 z.$$

With (2.7.6) we get

$$-H_0 \frac{\partial \chi(\vec{r})}{\partial z} - \vec{\nabla} \cdot \chi(\vec{r}) \left( \vec{h}_{\text{in}}(\vec{r}) + \vec{h}_{\text{obj}}(\vec{r}) \right) + (1 + \chi(\vec{r})) \left( \vec{\nabla}^2 \cdot \Phi_{\text{in}}(\vec{r}) + \vec{\nabla}^2 \cdot \Phi_{\text{obj}}(\vec{r}) \right) = 0.$$

As this equation has to be valid also without any disturbing object, i.e. for  $\chi = 0$ ,  $\Phi_{\text{obj}} = 0$ , the condition  $\vec{\nabla}^2 \cdot \Phi_{\text{in}} = 0$  must hold. If we neglect again higher order terms we find the final equation that has to be solved

$$\vec{\nabla}^2 \Phi_{\text{obj}}(\vec{r}) = -H_0 \frac{\partial \chi(\vec{r})}{\partial z}. \quad (2.7.7)$$

## 2.7.2 Solutions of Laplace's equation using Fourier transform

The discrete Fourier transform of  $\Phi_{\text{obj}}$  and  $\chi(\vec{r})$  is defined in the standard way

$$\begin{aligned} \mathcal{F}(\tilde{\Phi}_{\text{obj}}(\vec{r})) &= \Phi_{\text{obj}}(\vec{k}) = \sum_k \Phi_{\text{obj}}(\vec{r}) e^{-i\vec{k}\vec{r}}, \\ \mathcal{F}(\tilde{\chi}(\vec{r})) &= \chi(\vec{k}) = \sum_k \chi(\vec{r}) e^{-i\vec{k}\vec{r}}. \end{aligned}$$

Using

$$\begin{aligned}\vec{\nabla}^2 \Phi_{\text{obj}}(\vec{k}) &= -k^2 \Phi_{\text{obj}}(\vec{k}), \\ \frac{\partial \chi(\vec{k})}{\partial z} &= -ik_z \chi(\vec{k}),\end{aligned}$$

the Fourier transform of (2.7.7) reads

$$\Phi_{\text{obj}}(\vec{k}) = -iH_0 \frac{k_z}{k^2} \chi(\vec{k}). \quad (2.7.8)$$

As we are looking for a solution for  $h_{\text{obj},z}$ , we find

$$\begin{aligned}h_{\text{obj},z} &= -\frac{\partial \Phi_{\text{obj}}}{\partial z} = -\mathcal{F}^{-1} \left[ ik_z \Phi_{\text{obj}}(\vec{k}) \right] \\ &= -H_0 \mathcal{F}^{-1} \left[ \frac{k_z^2}{k^2} \chi(\vec{k}) \right],\end{aligned} \quad (2.7.9)$$

which leads to the final solution for the magnetic field at the location of the nucleus

$$B_{\text{nuc},z} = \mu_0 H_0 + \mu_0 h_{\text{in},z} + \mu_0 H_0 \left( -\sigma + \mathcal{F}^{-1} \left[ \left( \frac{1}{3} - \frac{k_z^2}{k^2} \right) \chi(\vec{k}) \right] \right). \quad (2.7.10)$$

### 2.7.3 Analytical solution for simple geometries

For a sphere with homogeneous susceptibility  $\chi_i$  surrounded by a medium of susceptibility  $\chi_e$  we find for the magnetic field at the position of the nucleus inside the sphere  $B_{\text{nuc},i}(\vec{r})$  and outside the sphere  $B_{\text{nuc},e}(\vec{r})$  (A.1.12)

$$\begin{aligned}(B_{\text{nuc},i})_x &= (b_{\text{in}})_x \\ (B_{\text{nuc},i})_y &= (b_{\text{in}})_y \\ (B_{\text{nuc},i})_z &= B_0 \frac{3 + 3\chi_i}{3 + 2\chi_e + \chi_i} + (b_{\text{in}})_z - B_0 \left( \sigma + \frac{2}{3}\chi_i \right) \\ (B_{\text{nuc},e})_x &= -B_0 \frac{\chi_e - \chi_i}{3 + \chi_i + 2\chi_e} a^3 \frac{xz}{r^5} + (b_{\text{in}})_x \\ (B_{\text{nuc},e})_y &= -B_0 \frac{\chi_e - \chi_i}{3 + \chi_i + 2\chi_e} a^3 \frac{yz}{r^5} + (b_{\text{in}})_y \\ (B_{\text{nuc},e})_z &= B_0 \left( 1 - \frac{\chi_e - \chi_i}{3 + \chi_i + 2\chi_e} a^3 \frac{2z^2 - x^2 - y^2}{r^5} \right) + (b_{\text{in}})_z - B_0 \left( \sigma + \frac{2}{3}\chi_e \right).\end{aligned} \quad (2.7.11)$$

In the case of an infinitely long cylinder of susceptibility  $\chi_i$  in a medium of susceptibility  $\chi_e$  we get for the magnetic field inside the cylinder  $B_{\text{nuc},i}(\vec{r})$  and outside  $B_{\text{nuc},e}(\vec{r})$  (A.2.14)

$$\begin{aligned}
 (B_{\text{nuc},i})_x &= B_0 + \frac{3\chi_e - \chi_i + 2\chi_i\chi_e}{6 + 3\chi_i + 3\chi_e} B_0 - B_0\sigma + (b_{\text{in}})_x \\
 (B_{\text{nuc},i})_y &= (b_{\text{in}})_y \\
 (B_{\text{nuc},i})_z &= (b_{\text{in}})_z \\
 (B_{\text{nuc},e})_x &= B_0 + B_0 a^2 \frac{(\chi_i - \chi_e)}{(2 + \chi_i + \chi_e)} \frac{(x^2 - y^2)}{\rho^4} + \frac{1}{3}\chi_e B_0 - B_0\sigma + (b_{\text{in}})_x \\
 (B_{\text{nuc},e})_y &= B_0 a^2 \frac{(\chi_i - \chi_e)}{(2 + \chi_i + \chi_e)} \frac{2xy}{\rho^4} + (b_{\text{in}})_y \\
 (B_{\text{nuc},e})_z &= (b_{\text{in}})_z \quad .
 \end{aligned} \tag{2.7.12}$$

## 2.8 Magnetic field inhomogeneities and temperature measurements

After we have discussed the effects of magnetic field inhomogeneities on the spatial encoding in (2.5) and the available procedures for temperature measurements in (2.6) we now want to examine the influence of field changes on temperature maps acquired with the PRF method. As outlined in the previous sections (2.5.7) and (2.6.4) the phase in the presence of field inhomogeneities reads

$$\Phi(T(\vec{r}), \vec{r}) = \gamma \mathbf{TE} \left( -B_0\sigma(T(\vec{r})) + \Delta B(\vec{r}) \right) . \tag{2.8.1}$$

Here we have neglected the term containing  $\Delta B(\vec{r})\sigma(T(\vec{r}))$  as it is a very small quantity.

On the other hand if we also take into account the temperature dependence of the magnetic susceptibility, the field deviations are not constant with temperature any more. Consequently in contrast to the simple case with a non-varying susceptibility where the phase change is given by

$$\begin{aligned}
 \Delta\Phi(\vec{r}) &= \gamma \mathbf{TE} \left( -B_0 \cdot \frac{\Delta\delta}{\Delta T(\vec{r})} (T_2(\vec{r}) - T_1(\vec{r})) + \Delta B(\vec{r}) \right) \\
 &= \gamma \mathbf{TE} B_0 \left( -\frac{\Delta\delta}{\Delta T(\vec{r})} + \frac{1}{B_0} \frac{\Delta B(\vec{r})}{\Delta T(\vec{r})} \right) \Delta T(\vec{r}),
 \end{aligned} \tag{2.8.2}$$

and  $\Delta T(\vec{r}) = T_2(\vec{r}) - T_1(\vec{r})$ , we now get a more complicated expression

$$\Delta\Phi(\vec{r}) = \gamma \mathbf{TE} \left[ \frac{\Delta B(T_2(\vec{r})) - \Delta B(T_1(\vec{r}))}{\Delta T(\vec{r})} - B_0 \frac{\Delta\delta}{\Delta T(\vec{r})} \right] \Delta T(\vec{r}) . \tag{2.8.3}$$

Here a closed solution of the problem for a correction procedure is not possible. Hence, we have to apply some simplifications. After Fourier transform (2.8.2) reads

$$\Delta\Phi(\vec{k}) = \gamma \mathbf{IE} B_0 \left[ -\frac{\partial\delta(T(\vec{k}))}{\partial T(\vec{k})} + \frac{1}{B_0} \frac{\Delta B(T(\vec{k}))}{\Delta T(\vec{k})} \right] \Delta T(\vec{k}). \quad (2.8.4)$$

Considering the solution for  $\Delta B$  in (2.7.10)

$$\Delta B(\vec{k}) = B_0 \left( \frac{1}{3} - \frac{k_z^2}{k^2} \right) \chi(\vec{k})$$

and assuming a linear temperature dependency of  $\chi(T)$  and  $\delta(T)$  we obtain the correct temperature change.

$$\Delta T_{\text{corr}}(\vec{k}) = -\Delta\Phi(\vec{k}) \left( \gamma \mathbf{IE} B_0 \frac{\partial\delta}{\partial T} \left[ 1 - \left( \frac{\partial\delta}{\partial T} \right)^{-1} \frac{\partial\chi(T(\vec{k}))}{\partial T} \left( \frac{1}{3} - \frac{k_z^2}{k^2} \right) \right] \right)^{-1} \quad (2.8.5)$$

Without this correction procedure one would calculate the temperature change as

$$\Delta T_{\text{meas}}(\vec{k}) = -\frac{\Delta\Phi_{\text{meas}}(\vec{k})}{\gamma \mathbf{IE} B_0 \frac{\partial\delta}{\partial T}}. \quad (2.8.6)$$

Combining (2.8.5) and (2.8.6) we find an expression which can be used to correct temperature maps with respect to the influence of the magnetic susceptibility [37].

$$\Delta T_{\text{meas}}(\vec{k}) = \left[ 1 - \left( \frac{\partial\delta}{\partial T} \right)^{-1} \cdot \frac{\partial\chi(T(\vec{k}))}{\partial T} \left( \frac{1}{3} - \frac{k_z^2}{k^2} \right) \right] \Delta T_{\text{corr}}(\vec{k}). \quad (2.8.7)$$

Even though this result seems to be very promising its applicability is very limited due to the assumptions made. A linear temperature dependence of  $\chi(T)$  is usually not existing. It has been shown that this condition is approximately fulfilled for pure water with a temperature dependence of  $\frac{\partial\chi}{\partial T} \approx 3 \cdot 10^{-9} \text{K}^{-1}$  [31]. Examining the exact temperature dependence of water [32]

$$\begin{aligned} \chi_{\text{water}}(T) &= \chi_0 [1 + a(T - T_0) + b(T - T_0)^2 + c(T - T_0)^3] & (2.8.8) \\ \text{with } a &= 1.38810 \cdot 10^{-4} \text{K}^{-1} \\ b &= -1.2685 \cdot 10^{-7} \text{K}^{-2} \\ c &= 8.09 \cdot 10^{-10} \text{K}^{-3} \\ T_0 &= 273.15 \text{K} \\ \chi_0 = \chi(T_0) &= -9.09 \cdot 10^{-6} \end{aligned}$$

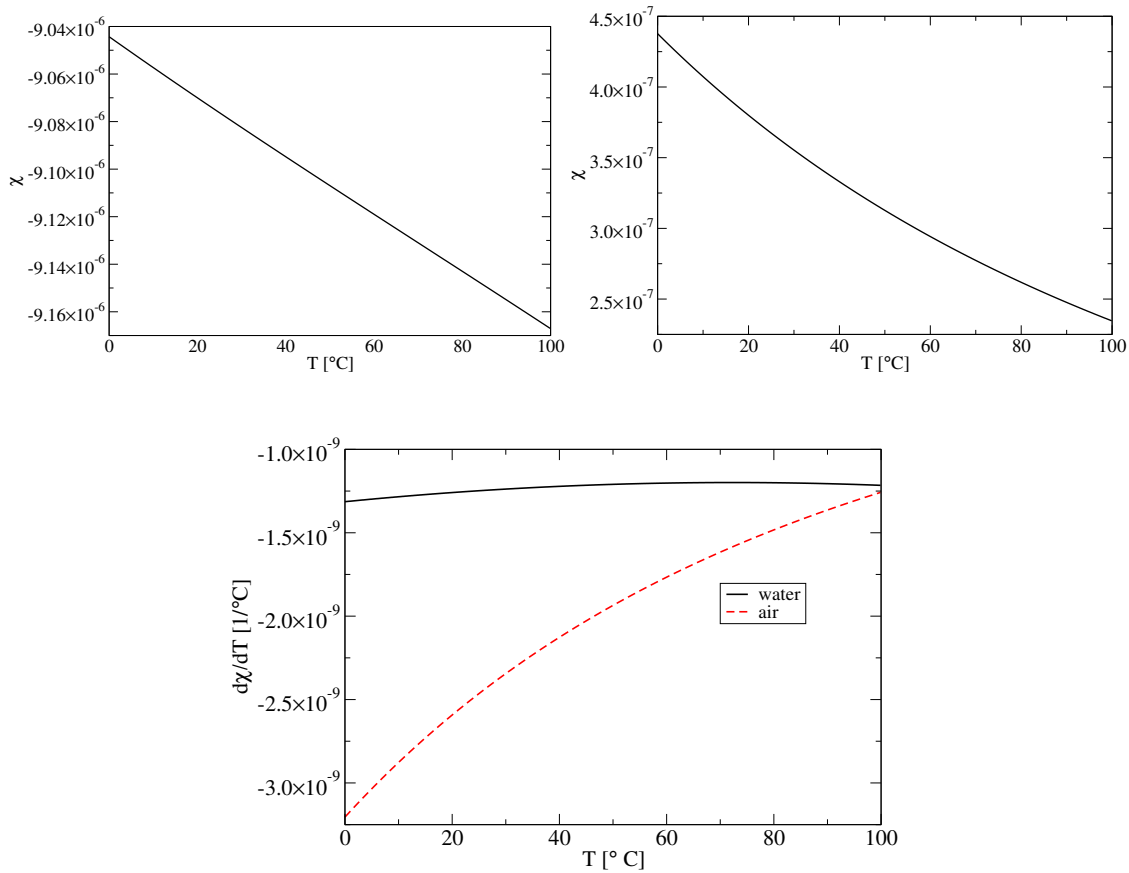


**Figure 2.14:** Temperature dependence of the susceptibilities of water and air. Top left  $\chi(T)$  for water; Top right  $\chi(T)$  for air; Bottom:  $\partial\chi/\partial T$  for air (red dotted line) and water (black line)

we found a different value of  $\frac{\partial\chi}{\partial T} \approx -1.23 \cdot 10^{-9}/^{\circ}C$  for a temperature of  $37^{\circ}C$ . As most tissues in the body show similar magnetic properties like water this relationship also holds for them. In contrast, the susceptibility of air shows a stronger temperature dependence [41].

$$\chi_{\text{air}}(T) = \chi(293.15K) \left( \frac{293.15K}{273.15K + T[K]} \right)^2, \quad \chi(293.15K) = 0.38 \cdot 10^{-6}. \quad (2.8.9)$$

Consequently, it is more difficult to treat air-filled cavities with this approach because the linear assumption for  $\chi(T)$  does not hold any more. In Fig. 2.14 we can see clearly that for water the temperature dependence is constant over a large temperature range, whereas  $\frac{\partial\chi}{\partial T}$  for air still changes by approximately  $2 \cdot 10^{-10} \text{ K}^{-1}$ . Likewise, all kind of magnetic materials show more complex temperature dependencies and have to be treated differently.

## 2.9 Subsumption

In this chapter the principles of MR imaging and temperature measurements were introduced. The proton resonance frequency method seems to be the best choice for our applications and delivers temperature information via the expression

$$\Delta T = \frac{\Phi_T - \Phi_{\text{ref}}}{\gamma B_0 \delta(T) TE}.$$

Furthermore, the effects of field deviations on the spatial encoding were explained yielding one fundamental equation for the pixel displacement in the presence of a field inhomogeneity  $\Delta B$

$$\Delta x = \frac{\Delta B}{G_x}.$$

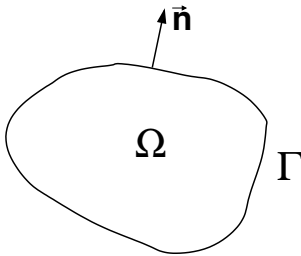
Finally, the influence of temperature dependent susceptibilities was discussed. This allows the development of correction procedures for both geometrical distortions and temperature deviations.

### 3 Numerical techniques

In the previous chapter we discussed the causes of image distortions and possibilities to correct them. All these correction procedures require the knowledge of the local magnetic field. There exist many different approaches to solve this problem which can generally be divided into two categories. One uses the general solution of Laplace’s equation in integral form for a general susceptibility distribution and solves this equation for the magnetic field. This can be done by the use of finite elements [1], the uniqueness of the solution of boundary value problems [25] or by restriction to simple geometries like cylinders or spheres [7]. The other group tries to solve Laplace’s equation directly for a given susceptibility distribution with the help of iterative solvers [4, 35] or Fourier transform [36, 22, 23]. In this work, we solve Laplace’s equation by means of finite volumes and Fourier transform. The basic principles of these methods will be explained and validated by comparison with analytical results.

The application of the PRF approach for temperature measurements requires unwrapped phase images. Hence, in a second part of this chapter a new algorithm for this purpose is presented and applied to experimental data. Finally, the previously derived basic equation for geometrical distortions is utilized in two different correction procedures which are evaluated and compared in connection with experimental data.

#### 3.1 Finite volumes



The solution of partial differential equations by finite volume methods is based on the application of the Gauss integral theorem (Fig. 3.1):

$$\int_{\Omega} \vec{\nabla} \cdot \vec{f} \, d\vec{r} = \int_{\Gamma} \vec{f} \cdot \vec{n} \, ds. \tag{3.1.1}$$

The Gauss’ theorem allows to reduce the required order of the derivative to be calculated by one (from second to first), because instead of calculating the divergence of the fluxes  $\vec{f}$  integrated over the volume of one element the sum of the fluxes integrated over the boundary surfaces of these elements needs to be known. Consequently, the solution of Laplace’s equation

**Figure 3.1:** Integration volume  $\Omega$ , edge  $\Gamma$  and the surface normal  $\vec{n}$

for the magnetostatic potential  $\Phi$  in one dimension is given by the following expression, where the subscripts e and w denote the integrated value of the derivative over the eastern and western boundary surface of the volume element, respectively.

$$\frac{d}{dx} \left( \mu \frac{d\Phi}{dx} \right) = 0 \Rightarrow \left( \mu \frac{d\Phi}{dx} \right)_e - \left( \mu \frac{d\Phi}{dx} \right)_w = 0. \tag{3.1.2}$$

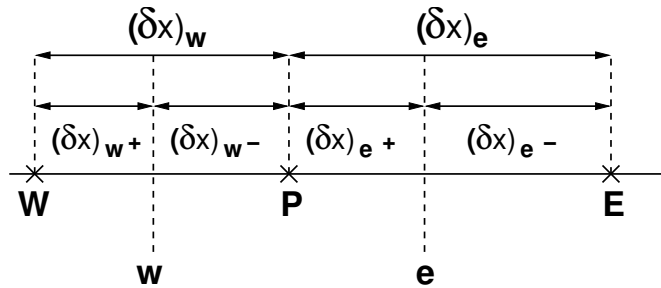


**Figure 3.2:** Metrics of the grid in 1D.

Transferring this to a discrete grid using first order Taylor expansion we obtain

$$\frac{\mu_e (\Phi_E - \Phi_P)}{(\delta x)_e} - \frac{\mu_w (\Phi_P - \Phi_W)}{(\delta x)_w} = 0, \quad (3.1.3)$$

where e(east) and w(west) denote the values of the potential on the interface between two adjacent cells (Fig. 3.2). Finally, a simplified expression reads

$$a_P \Phi_P = a_E \Phi_E + a_W \Phi_W$$

$$a_E = \frac{\mu_e}{(\delta x)_e}, \quad a_W = \frac{\mu_w}{(\delta x)_w}, \quad a_P = a_E + a_W. \quad (3.1.4)$$

The permeabilities on the interfaces have to be calculated for the fluxes  $B = \mu \cdot \mu_0 \vec{\nabla} \cdot \Phi$  through the interfaces based on the values of  $\mu$  in the adjacent cells.

$$\mu_e = \left( \frac{1 - f_e}{\mu_P} + \frac{f_e}{\mu_e} \right)^{-1} \quad \text{with} \quad f_e = \frac{(\delta x)_{e+}}{(\delta x)_e}.$$

For  $f_e = 0.5$  we obtain the harmonic mean of the neighboring permeabilities

$$a_E = \left( \frac{(\delta x)_{e-}}{\mu_P} + \frac{(\delta x)_{e+}}{\mu_e} \right)^{-1}.$$



### 3.1.1 Generalization to three dimensions

The generalization to three dimensions can be carried out easily by just adding the coefficients and potentials for the two new neighbours in the y-direction B(back) and F(front) as well as the two neighbours in the z-direction N(north) and S(south) to (3.1.4) (Fig. 3.3). Furthermore, according to the theorem of Gauss, we also have to consider the surfaces of the interfaces as a result of the integration. Consequently, the magnetostatic potential for the central point P is given by

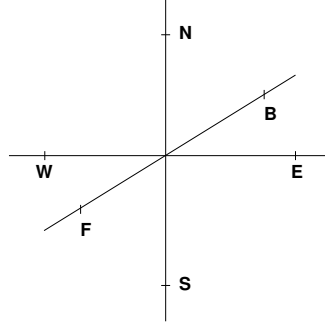


Figure 3.3: Metrics for 3D

$$a_P \Phi_P = a_E \Phi_E + a_W \Phi_W + a_F \Phi_F + a_B \Phi_B + a_S \Phi_S + a_N \Phi_N \quad (3.1.5)$$

with  $a_E = \left( \frac{(\delta x)_{e-}}{\mu_P} + \frac{(\delta x)_{e+}}{\mu_E} \right)^{-1} \cdot A_E$  and similar expressions for the other coefficients.

### 3.1.2 Boundary conditions

As the unique solution of a partial differential equation requires the specification of boundary conditions, these are especially important also for the case of Laplace's equation. For the geometry described in appendix A the correct boundary conditions are such that far away from the cylinder the value of  $\Phi$  for the undisturbed case, given by  $B_\infty = \frac{B_0}{\mu_0 \mu_a} \cdot x$  for the field aligned along the x-direction (A.1.4), is valid. For the z-direction the fluxes  $B_N$  through the upper boundary,  $B_S$  through the lower boundary respectively, are set to zero. This ensures independence of the solution of the z-direction as demanded by the geometry of an infinitely long cylinder.

$$0 = B_N = \frac{\Phi_N - \Phi_P}{(\delta z)_{n-} + (\delta z)_{n+}} A_N \implies \Phi_N = \Phi_P,$$

$$0 = B_S = \frac{\Phi_P - \Phi_S}{(\delta z)_{s-} + (\delta z)_{s+}} A_S \implies \Phi_S = \Phi_P.$$

Introducing this condition into (3.1.5) leads to an altered expression for the magnetostatic potential at the point P situated at the upper boundary

$$(a_P - a_N) \Phi_P = a_E \Phi_E + a_W \Phi_W + a_F \Phi_F + a_B \Phi_B + a_S \Phi_S, \quad (3.1.6)$$

and at the lower boundary

$$(a_P - a_S) \Phi_P = a_E \Phi_E + a_W \Phi_W + a_F \Phi_F + a_B \Phi_B + a_N \Phi_N, \quad (3.1.7)$$

respectively.

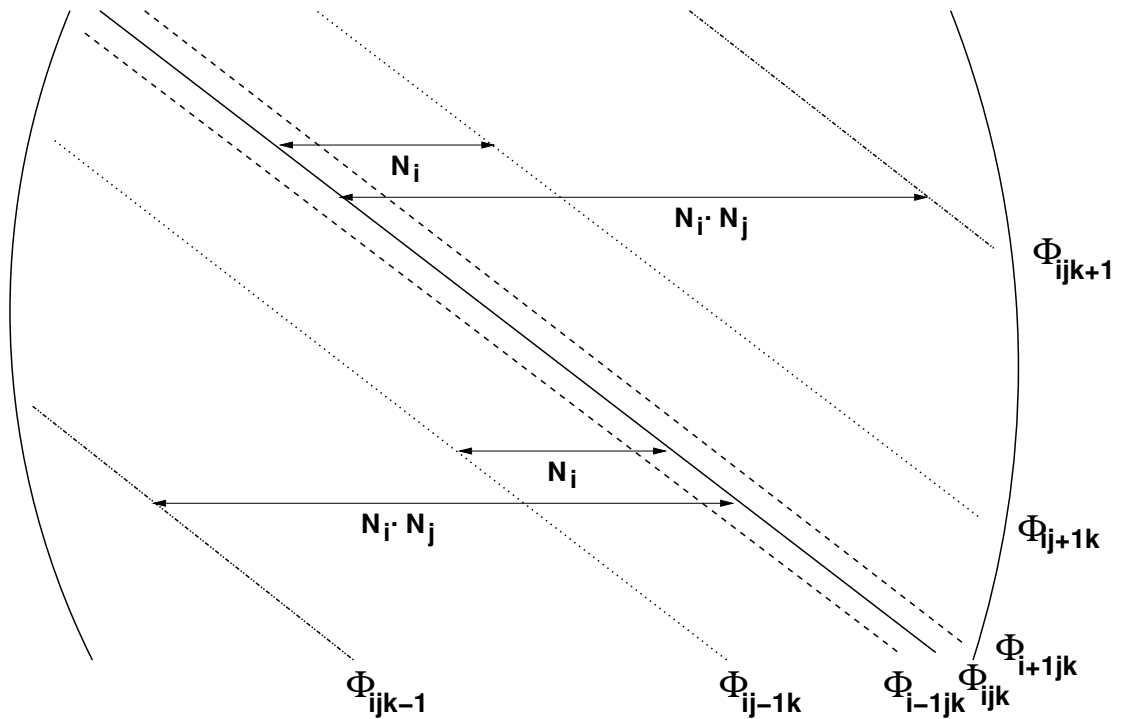


Figure 3.4: Structure of the coefficient matrix for three dimensions.

### 3.1.3 Solution of the problem

To obtain the magnetostatic potential (3.1.5) has to be solved for every grid point. Consequently we have to find the solution for a linear system of  $N = N_x N_y N_z$  equations where  $N_i$  denotes the size of the system in this direction. This can be formulated as

$$\mathbf{A}\vec{\Phi} = \vec{b}. \quad (3.1.8)$$

$\mathbf{A}$  is the coefficient matrix of size  $N \times N$ ,  $\vec{\Phi}$  the demanded solution for the magnetostatic potential of length  $N$  and  $\vec{b}$  contains the inhomogeneous parts of the partial differential equation. In our case  $\vec{b} = \vec{0}$ , because we do not include any electric charges or currents. For the three dimensional case the matrix  $\mathbf{A}$  is a sparse band-matrix (Fig. 3.4). In this case the vector  $\vec{\Phi}$  has the following form

$$\vec{\Phi} = (\Phi_0, \Phi_1 \dots \Phi_m \dots \Phi_{N-2}, \Phi_{N-1})^T$$

where  $m$  denotes a one dimensional running index given by  $m = k \cdot N_x \cdot N_y + j \cdot N_x + i$  ( $k = 0 \dots N_z - 1$ ,  $j = 0 \dots N_y - 1$ ,  $i = 0 \dots N_x$ ).

There are two basic methods for solving this matrix equation. Explicit methods solve (3.1.5) for each grid point separately whereas implicit techniques seek to solve the complete system using matrix operations.

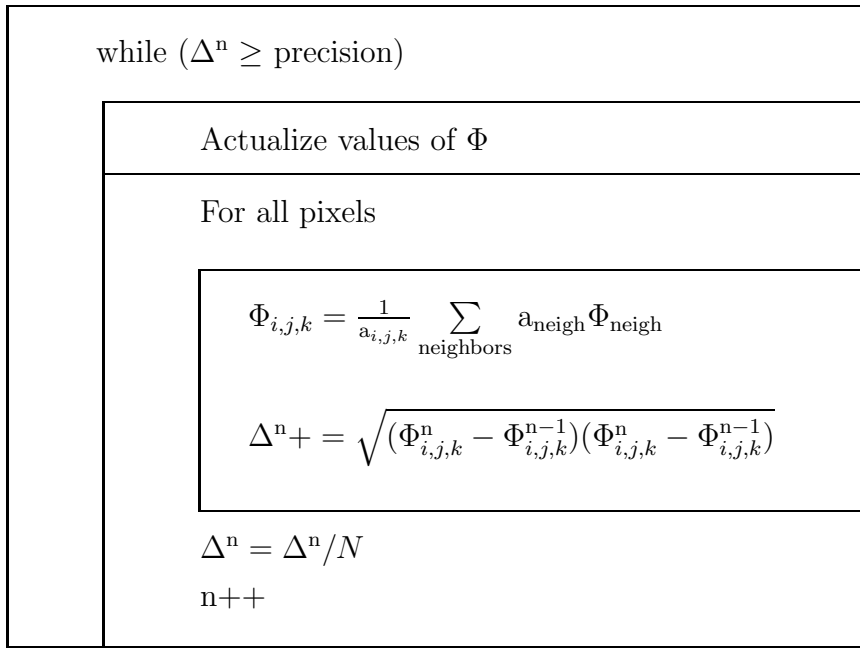


**Figure 3.5:** Iterative relaxation algorithm for the explicit calculation of the magnetostatic potential. During the  $n^{\text{th}}$  iteration step the potential for each pixel position is calculated using the neighbouring potential values. Additionally the root mean square change  $\Delta^n$  compared to the previous iteration step is calculated.

### Explicit calculation

Here, a relaxation algorithm is used which calculates  $\Phi_P$  for each grid point iteratively until steady-state is achieved. The basic algorithm is displayed in Fig. 3.5. For each iteration the potential at each pixel position is calculated using (3.1.5). Additionally, the root mean square change  $\Delta^n$  compared to the previous iteration step is calculated to monitor the relaxation behavior of the system.

$$\Delta^n = \frac{1}{N} \sum_{i=0}^{N-1} \sqrt{(\Phi_i^n - \Phi_i^{n-1})(\Phi_i^n - \Phi_i^{n-1})}.$$

Here  $i$  counts the pixels and  $n$  marks the current iteration step. If the value of  $\Delta^n$  drops below a previously defined tolerance the procedure stops yielding the value of the magnetostatic potential.

### Implicit calculation

For the implicit algorithm we use the direct solver ma28 for the solution of linear equation systems with sparse coefficient matrices [10, 20], which supplies different routines

depending on the structure of the considered matrix. At first, the ILU factorization<sup>1</sup> of the matrix  $\mathbf{A}$  is performed and stored in an intermediate array. In a second step, the system is solved by iterative refinement using the results of the previous calculations. The input consists of three arrays containing the row and column number of non-zero entries as well as their values. As the ILU algorithm is very memory consuming, its applicability is restricted to small systems up to 40000 grid points on the used system (Intel Pentium 4, 3.80GHz).

### 3.1.4 Comparison between analytical and numerical results

To verify the implementation of the numerical methods we compare it with known analytical results. As a test case we take an infinitely long homogeneous cylinder with its axis perpendicular to the applied field  $\vec{B} = (B_0, 0, 0)$  and compare the analytical results (2.7.12) with the results obtained using finite volumes.

Figures 3.6 and 3.7 show the effect of different resolutions on the accuracy of the results obtained by the finite volume technique. The computational error is determined by the deviation of the calculated magnetic field from the known analytical solution (2.7.12). As expected, the results achieved with the explicit and implicit implementation are similar. Both show an increased accuracy with growing resolution even though there are still deviations from the analytical solution. For the implicit method the resolution was limited to 40000 data points by the enormous memory consumption of the sparse matrix solver.

---

<sup>1</sup>The ILU factorization yields an upper triangular matrix U, a lower triangular matrix L and a residual R which fulfill  $A=LU+R$ . This is often applied as a preconditioning step to improve the convergence for a given problem.

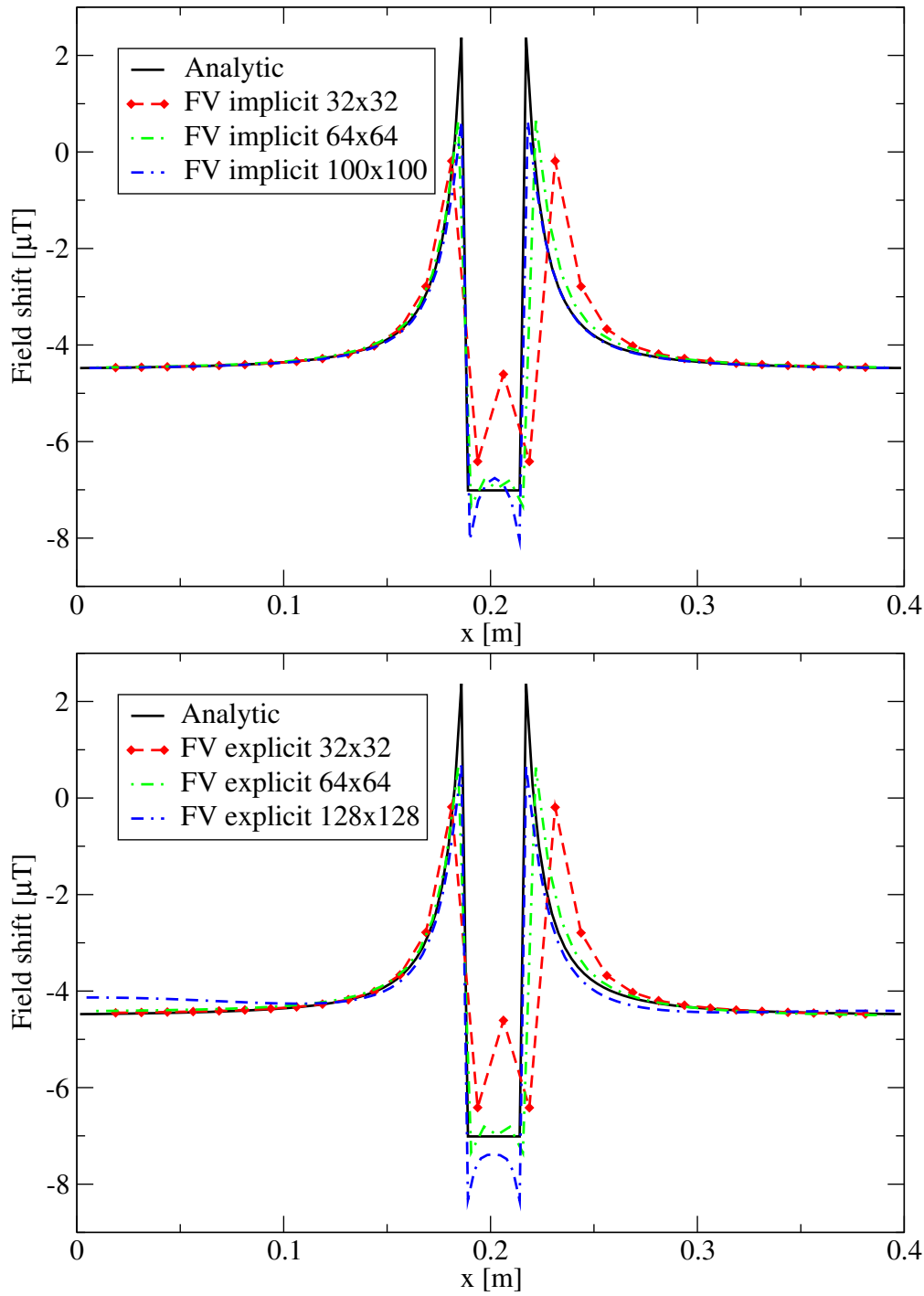


**Figure 3.6:** Numerical calculations using the explicit and implicit finite volume technique versus the analytical solution for a resolution of  $32 \times 32$ ,  $64 \times 64$  and  $100 \times 100$  with a tolerance of  $\Delta^n = 10^{-10}$ . The profiles along the  $x$ -axis through the center of the cylinder show the resulting field shift along  $x$  for  $\chi_i = 0.928 \cdot 10^{-6}$ ,  $\chi_e = -9.0763 \cdot 10^{-6}$ ,  $\text{FOV} = (0.4 \times 0.2) \text{ m}^2$ . As the results were independent of  $z$ , a low resolution of 10 grid points along the  $z$ -direction was used.

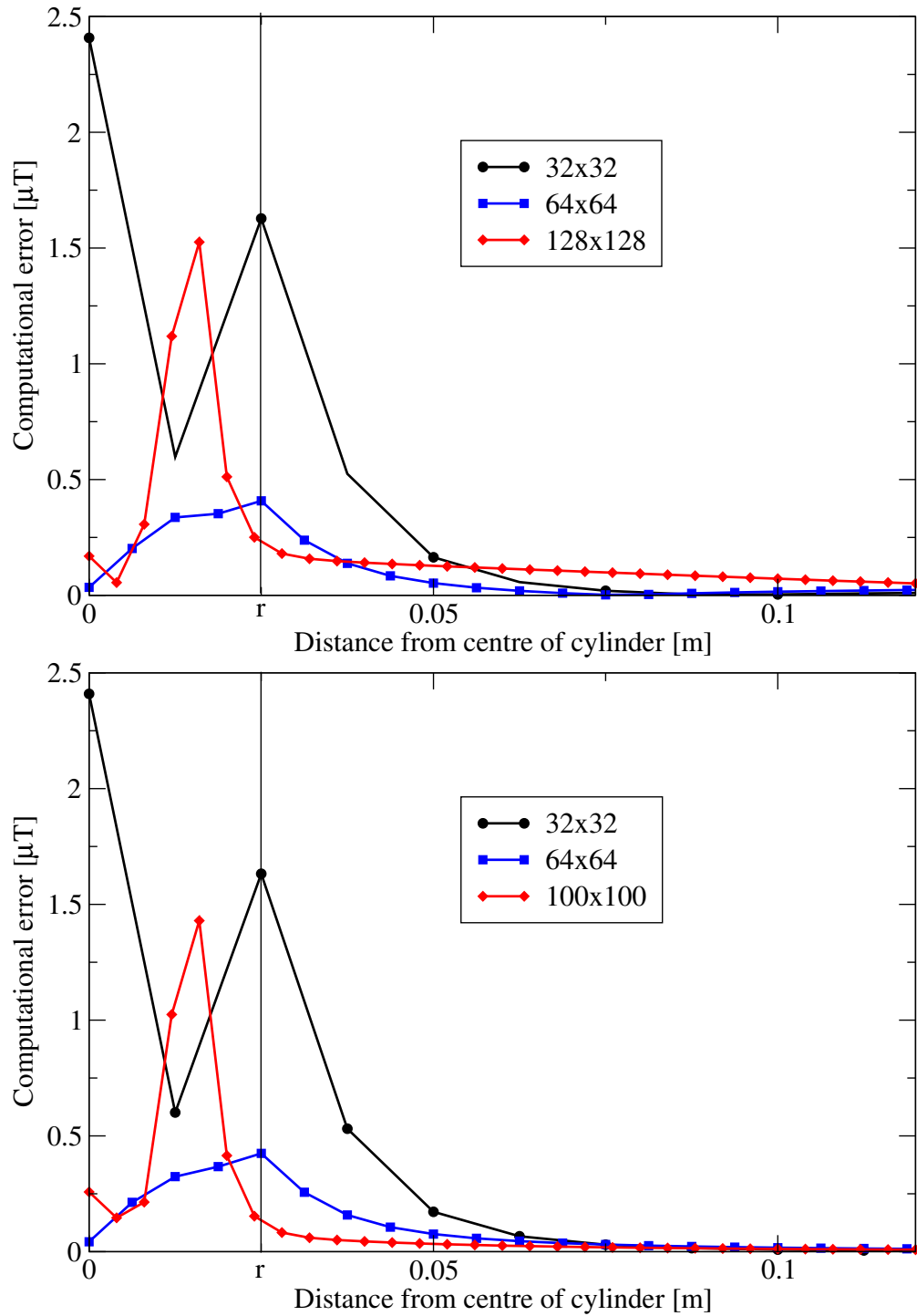


**Figure 3.7:** Computational error of the simulations using the finite volume techniques versus the distance from the center of the cylinder along the x-axis for different resolutions; Top: Explicit calculation with a resolution of 32x32, 64x64 and 100x100,  $\Delta^n = 10^{-10}$ ; Bottom: Implicit calculation with a resolution of 32x32, 64x64 and 128x128.

## 3.2 Fourier transformation

The Fourier transformation offers another powerful possibility to solve Laplace's equation by transforming the spatial derivative of the magnetostatic potential into a simple multiplication in the frequency domain.

Following the deduction of Salomir and Moonen [36], the equation to be solved for the magnetostatic potential reads (2.7.2):

$$\vec{\nabla}^2 \cdot \Phi_{\text{nuc}} = -H_0 \frac{\partial \chi(\vec{r})}{\partial z} \quad (3.2.1)$$

Here  $H_0$  is the value of the homogeneous main magnetic field in z-direction and  $\chi(\vec{r})$  is the position dependent magnetic susceptibility.

The transition to the frequency space enables us to simplify the problem yielding an expression for the z-component of the magnetic field at the location of the nucleus (2.7.2).

$$B_{\text{nuc},z} = \mu_0 H_0 + \mu_0 h_{\text{in},z} + \mu_0 H_0 \left( -\sigma + \mathcal{F}^{-1} \left[ \left( \frac{1}{3} - \frac{k_z^2}{k^2} \right) \chi(k) \right] \right) \quad (3.2.2)$$

This expression contains contributions both from the homogeneous main magnetic field  $\mu_0 H_0$  and the magnetic field inhomogeneities  $\mu_0 h_{\text{in},z}$ . The last term describes the disturbing field induced by the object and depends on the absolute value of the k-space coordinate  $k$ , its projection on the z-axis  $k_z$  and the Fourier transform of the susceptibility distribution  $\chi(\vec{k})$ .

### 3.2.1 Comparison between analytical and numerical results

For the case of an infinitely long homogeneous cylinder with its axis perpendicular to the applied field  $\vec{B} = (B_0, 0, 0)$  we now compare the analytical results (A.2.14) with the results obtained using fast Fourier transform.

In Figs. 3.8 and 3.9 we can see the effect of different resolutions on the accuracy of the results obtained by the fast Fourier transform. As expected, the error decreases with increasing resolution. For a resolution of  $256 \times 256$  data points in the xy-plane the Fourier transform technique achieves deviations of only  $0.58 \mu\text{T}$  at the susceptibility boundary and less than  $0.1 \mu\text{T}$  in the regions far away from the cylinder. A comparison with results obtained by [22] and [23] shows good agreement as they achieved maximum errors of approximately  $0.15 \mu\text{T}$ ,  $0.1 \mu\text{T}$  respectively, which is on the same order for similar susceptibility differences.

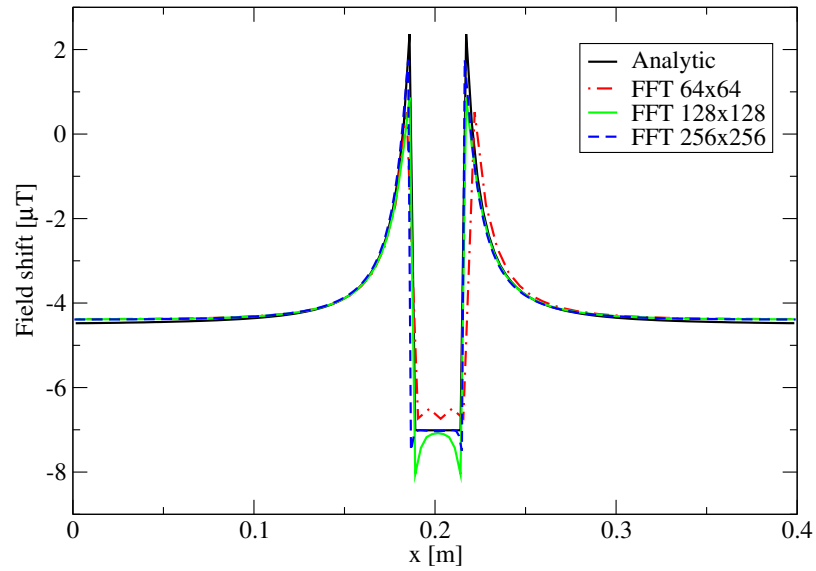


**Figure 3.8:** Numerical calculations using the Fourier transform method versus analytical solution for a resolution of  $64 \times 64 \times 16$ ,  $128 \times 128 \times 16$  and  $256 \times 256 \times 16$ . The profiles along the x-axis through the center of the cylinder show the resulting field shift values for  $\mu_0 = 1.2566 \times 10^{-6}$  T,  $\mu_0 = 0.2709 \times 10^{-6}$  T,  $\text{FOV} = (0.4)$ .

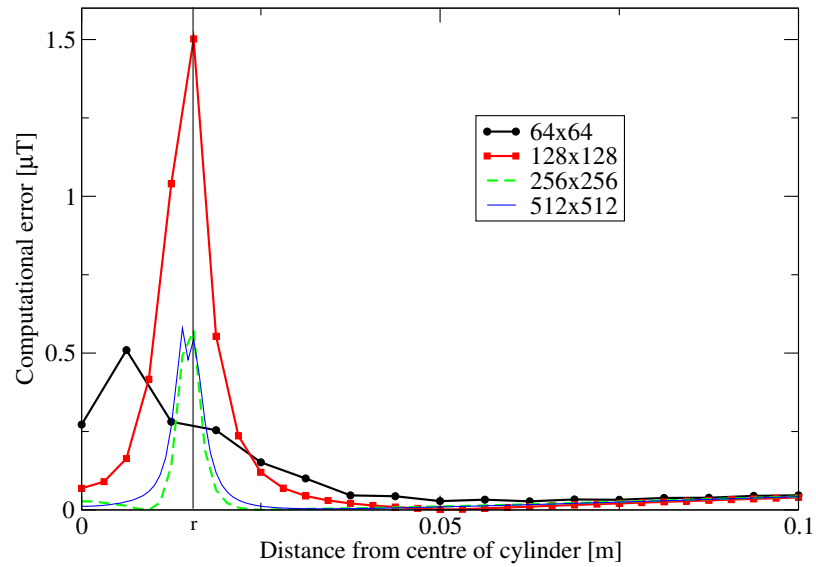


**Figure 3.9:** Computational error of the simulations using the Fourier transform method versus the distance from the center of the cylinder along the x-axis for different resolutions  $64 \times 64 \times 16$ ,  $128 \times 128 \times 16$ ,  $256 \times 256 \times 16$ ,  $512 \times 512 \times 16$ .



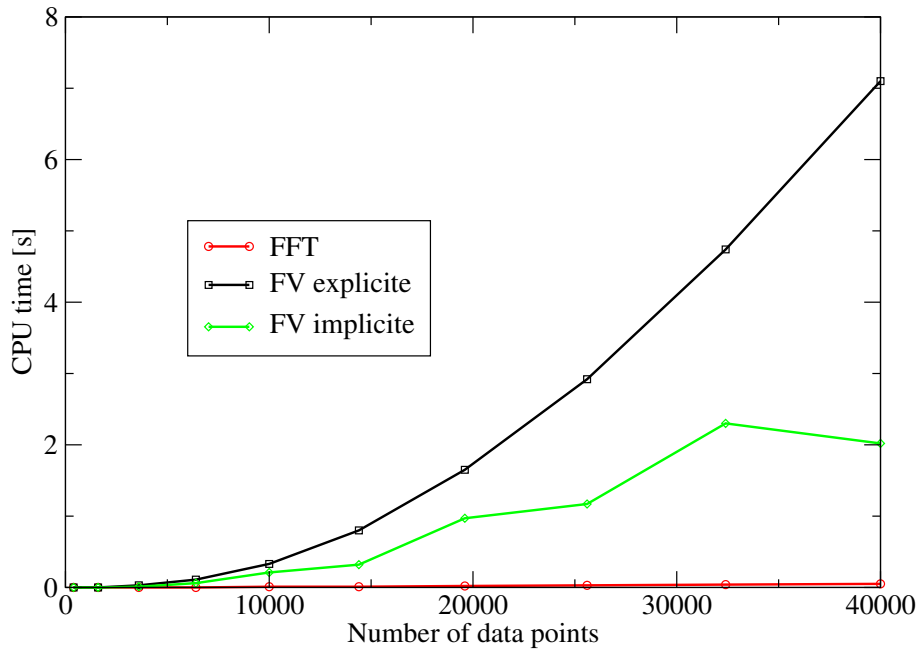


**Figure 3.10:** Required CPU time for the solution and an accuracy for the explicit finite volume scheme of  $\Delta^n = 10^{-10}$  versus the number of data points for the different numerical techniques.

### 3.3 Comparison between fast Fourier transformation and finite volumes

If we compare the results for a small resolution of  $32 \times 32$  in the  $xy$ -plane (Fig. 3.7, 3.9) the Fourier transform method obtains already very good results whereas both the explicit and the implicit finite volume approach still show great deviations from the analytical solution. This is mainly because a small number of larger pixels can only give a rough step-wise estimate of the true curved surface of the cylinder. Even though the finite volume technique improves for a higher number of data points the Fourier transform is still superior. Comparing the required calculation times (Fig. 3.10) this statement is further confirmed because the fast Fourier transform method only needs milliseconds in contrast to both finite volume methods which take minutes. After being validated for simple geometries both methods are able to handle all kind of susceptibility distributions without further changes in the implementation. This is advantageous for the application in the human body where a variety of substances with different susceptibilities are close together.

Because of its speed and accuracy the fast Fourier transformation will be used for all further calculations in this work.

|                                                  |
|--------------------------------------------------|
| <b>Segmentation</b>                              |
| <b>Search for phase jumps</b>                    |
| <b>Region definition</b>                         |
| <b>Determination of the phase jump direction</b> |
| <b>Correct phase jumps of proper regions</b>     |
| <b>Correction of special pixels</b>              |

Figure 3.11: Unwrapping method

### 3.4 Phase unwrapping algorithm

As already mentioned in Sect. (2.6.3) the acquired experimental images contain both magnitude and phase information, where the second one is more important for our purpose. Due to the intrinsic properties of the Fourier transform used to recover the image from the frequency space data, the phase values are periodic within  $2\pi$ . That means that all phase values are mapped into the interval  $[-\pi, \pi[$ , which in the scale of image pixels is rescaled to the interval  $[-4096, 4096[$ . This process is called wrapping. As outlined in Sect. (2) the temperature calculations are based just on phase differences which leads to a problem that can be visualized by the following example. Consider the same pixel in two successive images of a time series with the values  $2\pi/3, 5\pi/3$  respectively. The mentioned mapping to the interval  $[-\pi, \pi[$  leads to the new values  $2\pi/3$  and  $-1\pi/3$ . If we now calculate the phase difference between these two time series we gain for the unwrapped case  $\pi$  and for the wrapped case  $-\pi$  which gives a completely different temperature development. Therefore, unwrapping is mandatory. At first glance this seems to be easy, but it is complicated by several factors. One of them is noise overlaying the true image information. Very fast phase changes close to susceptibility boundaries, which occur frequently in the experimental data, can also lead to false unwrapping.

Several methods have been proposed to tackle this problem as it is not only important in magnetic resonance imaging but also for example in interferometry. The present solutions for phase unwrapping [5, 40, 46] can be divided into two major groups: path-following methods and minimum normalization methods. For both the problem can be formulated as

$$\Psi = \Phi + 2\pi n = W[\Phi], \quad (3.4.1)$$

where  $W$  is the wrapping operator,  $\Phi$  is the unwrapped and  $\Psi$  is the wrapped phase,

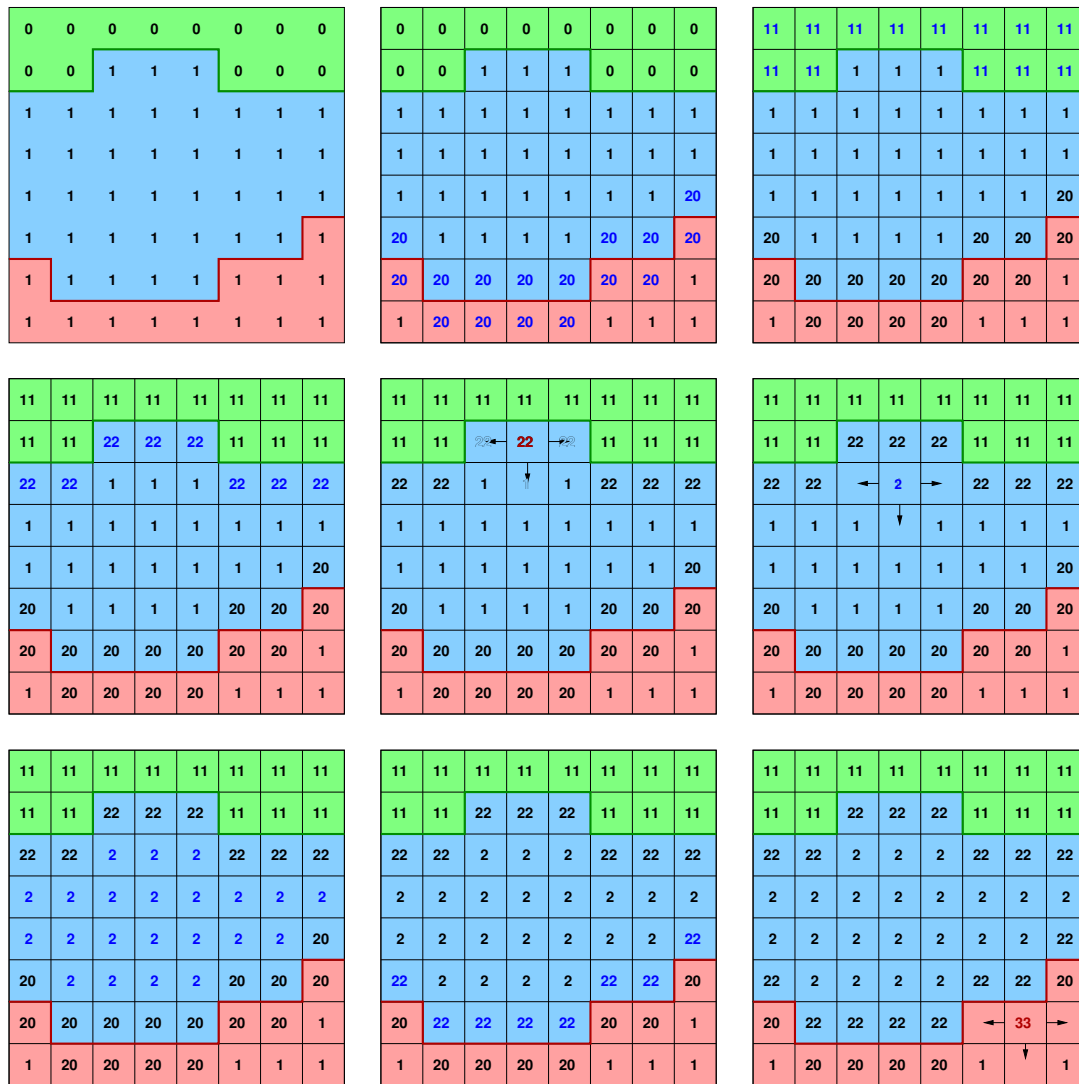


**Figure 3.12:** Process of region definition within the unwrapping algorithm. The red line denotes the position of a phase jump between neighboring pixels whereas the green line defines the border between noisy and image pixels. We start with a segmentation where all noisy pixels get an index 0 and the image pixels an index 1. Second all pixels are searched for phase jumps to their neighbors and get a new index 20 if the condition is fulfilled. Afterwards, the outer noisy region of the image is filled with index 11. The pixels with index 1 adjoining them get a new index 22 indicating that they belong to a border of the region with index 2. In the next step, a starting point for the region filling algorithm is selected which needs to have a neighbor with index 1 as well as one with index 11 to ensure that the filling will be successful. From there the whole area excluding the borders is marked with index 2. Finally, the pixels at the inner border get the new index 22. Now, a new level can start with the search for a starting point at the border to the region with index 2. This area will get the index 3 and so on until no further starting point fulfilling the requirements can be found.

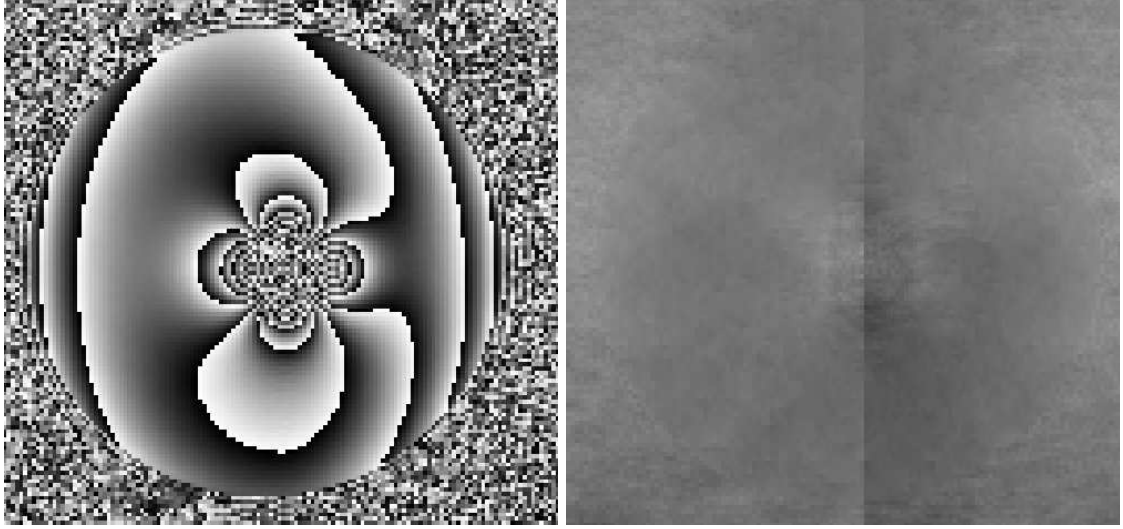


**Figure 3.13:** Phase unwrapping with a least-squares ansatz for an experimentally acquired phase image (TR=600ms, FOV (400×200)mm<sup>2</sup>, matrix 128×256, TE =20ms). As the method is based on a complete unwrapping solution for the whole grid it cannot cope with noisy pixels outside the box and inside the cylinder. Left: uncorrected image; Right: corrected image.

which obeys  $\Psi \in [-\pi, \pi[$ . If the phase difference between neighbouring pixels obeys  $\Delta\Phi \in [-\pi, \pi[$ , a simple line integration of the gradients along any path will result in an unwrapped phase. As soon as this is no longer fulfilled, e.g. if phase jumps larger than  $2\pi$  occur or strong noise is present along the path, this ansatz will lead to errors. In the given problem the central cylindrical object which does not give any phase information heavily disturbs the result. In this case, methods based on a least-squares ansatz are superior. One of these methods outlined in [33] leads for the two dimensional case to the following expression which has to be minimized:

$$\sum_{j,k} (\Phi_{j+1,k} - \Phi_{jk} - (\Psi_{j+1,k} - \Psi_{jk}))^2 + \sum_{j,k} (\Phi_{j,k+1} - \Phi_{jk} - (\Psi_{j,k+1} - \Psi_{jk}))^2. \quad (3.4.2)$$

In essence, this corresponds to a discretized version of Poisson's equation which can be solved easily by various means. A very general and fast way is the fast Fourier transform which was also used here with a slight variation. To directly include the boundary conditions for this special problem, a cosine transform was used. As the present numerical cosine transforms are not as fast as the present Fourier transform methods, a Fourier transform was modified via a mirror reflection of the transformed data to work like a cosine transform without loosing its intrinsic velocity. Nevertheless, this method was not able to cope with the disturbances produced by the central cylinder (Fig. 3.13) and had to be discarded.

Finally, a new algorithm for these special requirements was implemented (Fig. 3.11). It is based on a hierarchical division of the image into areas of the same phase, bounded by pixels, which contain one or more phase jumps. It starts with a segmentation of the

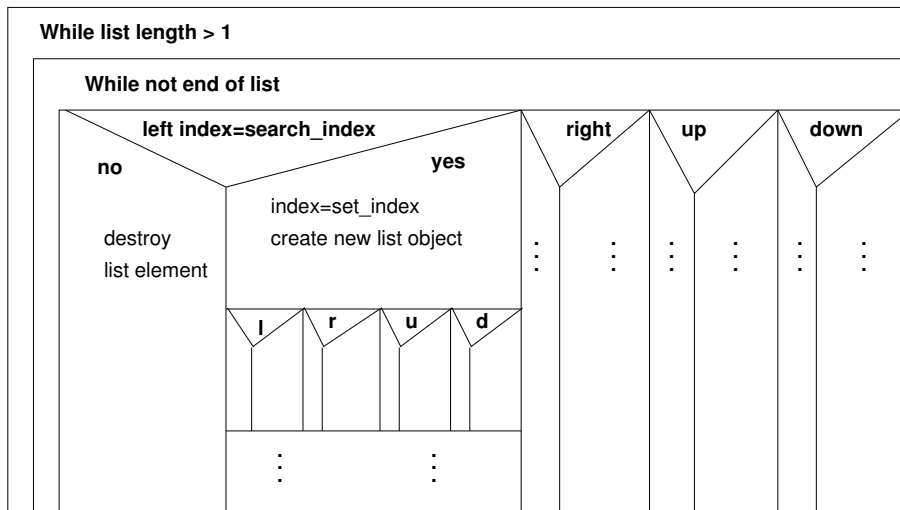


**Figure 3.14:** Region filling algorithm: After being given a starting point the algorithm searches all neighbors for the search index and in case of a hit changes its index to the set index. For this purpose, a list is built, where each list element contains the coordinates of a point whose neighbours are to be searched at the moment. When no neighbour has the right index, the search is stopped at this special point and the list element is deleted. This process continues until the list contains nothing but its starting element.

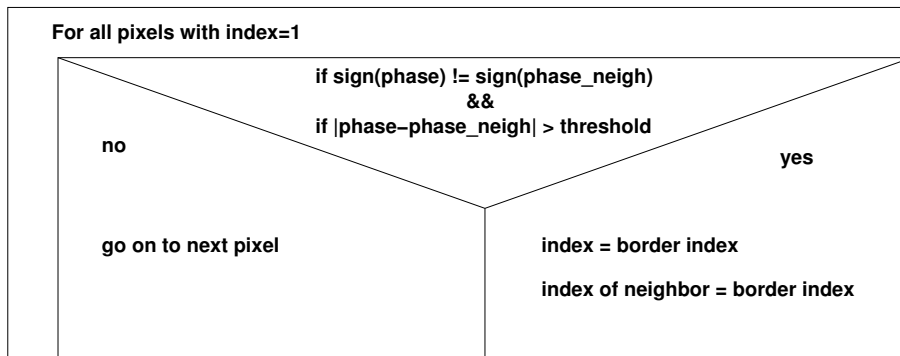
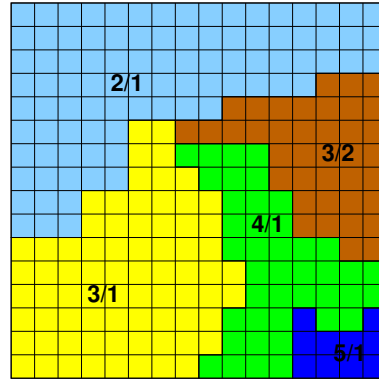


**Figure 3.15:** Algorithm for the detection of phase jumps. All pixels with index 1 are checked for phase jumps to one of the neighboring pixels. The requirements to be fulfilled are: a change in the phase sign and a phase difference greater than a certain threshold. If this is the case both the pixel and its neighbor get a new special border index.

**Figure 3.16:** Distribution of the different levels and regions over the grid. The algorithm starts with level 2. All areas adjoining it belong to level 3. Obviously this criterion is not unique giving rise to a new index denoting the number of the region. For example level 3 in the image is divided into two regions. Following this strategy all pixels are assigned one index for the level and one for the actual region on that level.



image, based on the information of the magnitude image. Here, pixels, whose values are below a certain threshold, get index 0 and index 1 if the value is higher. As a result both the noisy area around the imaged object and the air filled object inside are excluded and do not disturb the unwrapping result any more. As a next step the whole area with index 1, from now on denoted as image area, is searched for phase jumps between adjacent pixels. This is considered to be the case if the sign of the phase changes and the phase difference exceeds a certain value, in our case  $\pi/2$ . The detected pixel and its corresponding neighbour get a special index for border pixels (Fig. 3.15). After these preparation steps the basic part of the algorithm is initiated as visualized in Fig. 3.12. Starting on a grid which only contains indices 0 and 1, the area both adjoining the edge of the field of view and the image area are filled with index 11 by the region filling algorithm (Fig. 3.14). Secondly, the pixels neighbouring such a pixel get a new border index 22 and also deliver the starting point for a new filling algorithm, which fills the whole area up to the next border with the index 2. Finally, the pixels close to the next lower level also get the border index 22. This region owning level index 2 represents the reference for the phase correction and will therefore not undergo any changes. Consequently, it is only possible to unwrap the phase with a remaining offset to the true phase values depending on the starting region.

After the definition of the starting area the process is repeated with increasing filling indices and additional region indices. Another index becomes necessary, because, as can be seen in Fig. 3.16, it is always possible to get more than one area on the same hierarchical level, which have to be distinguished. This process continues until a certain index is reached. This is why this method only works for a moderate number of phase jumps per area. If there are no enclosed areas any more but only borders, additional corrections are necessary.

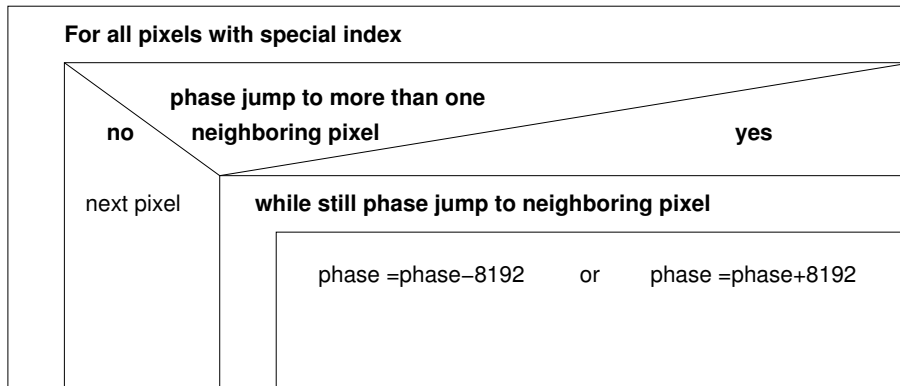


**Figure 3.17:** Correction algorithm for the remaining uncorrected pixels. They are systematically checked for phase jumps to more than one neighbor. If this requirement is fulfilled they are added or subtracted the value of 8096, which equals  $2\pi$  in radians, until there are no phase jumps to neighboring pixels any more.

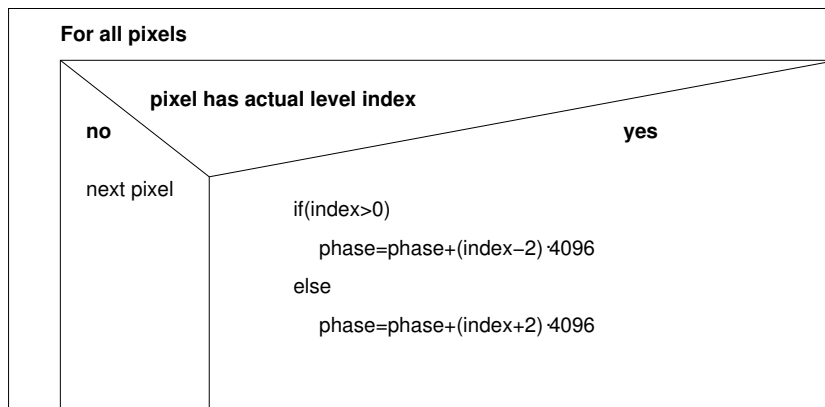


**Figure 3.18:** Correction algorithm for regular pixels. According to the level index the phase value is corrected where level index 2 is regarded as the true phase.

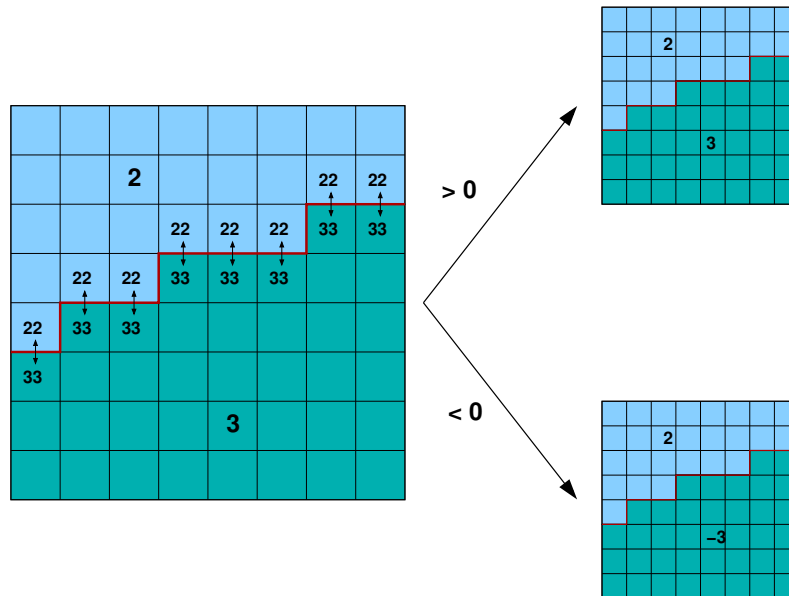


**Figure 3.19:** Determination of the phase jump direction along a border between different levels. For all pixels belonging to the periphery of a region the direction of the phase jumps to the next higher level, which means a lower level index, is determined giving a negative value for a phase decrease and a positive one for an increase. After integration and normalization over the whole border the absolute value has to exceed the threshold of 0.5 to be considered significant. If this is the case the index of the whole region is multiplied by this sign. Otherwise, the pixels get a special index to be treated again in the correction algorithm.

Up to now nothing is known about the direction of the phase jumps. The algorithm outlined in Fig. 3.19 searches the whole border of a level to the next higher one for the direction of the phase jump, giving a positive value for a phase increase and a negative one for a phase decrease. If the integrated and normalized values exceed the value of 0.5 the direction of the phase jump is regarded significant and the index of every member of this area is multiplied by this sign. Pixels that do not fulfill this requirement get a special index and have to be treated by a special correction subroutine (Fig. 3.17). Before, all pixels which were determined to be regular are corrected according to their index (Fig. 3.18). This means for an area of level index -3 a correction of  $-8192$ , or  $-2\pi$  in radians, as the level with index 2/-2 is regarded as the reference phase. Unfortunately, this procedure does not always lead to correct results. Figure 3.20 shows a case where the outlined algorithm imprints a wrong hierarchy on the regions. This is possible, because the starting region is considered to be unique. If this is not the case, other regions actually belonging to the same level will be given a wrong index. To avoid such problems a correction algorithm examines the connections between successive levels. It works similar to the already mentioned algorithm to detect the direction of phase jumps and determines integrated and normalized phase jumps along the whole border. Starting at the highest level, the border to the lower levels is checked and corrected by adding or



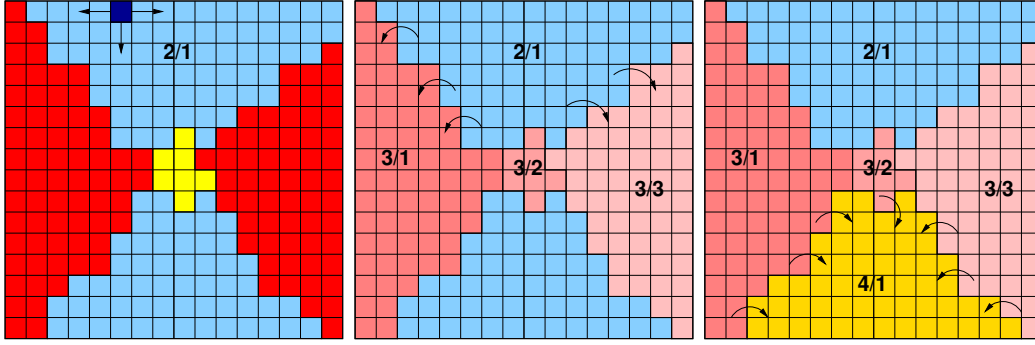


**Figure 3.20:** Problem of region definition. The left image shows a case, where the light blue areas actual belong to the same level. Starting the unwrapping algorithm in the dark blue point in the upper region, a false hierarchy is produced. As shown in the middle and right picture, the light blue region at the bottom is given the level index 4 instead of index 2.

subtracting 8192 until a smooth transition without phase jumps is achieved.

Finally, a correction algorithm for some special pixels is applied (Fig. 3.17). Here all pixels, which have not been treated by now are examined for phase jumps to more than one neighbor. If this is the case, their phase and index are changed according to the differences. This process is repeated until no irregularities can be found any more.

Figure 3.21 shows the resulting image in comparison to the uncorrected phase values for two different echo times. For the short echo time the phase changes were relatively small leading to a successful unwrapping. The image acquired with the longer echo time still shows some artifact pixels in the vicinity of the cylinder and at the edge of the image area. Here, as mentioned before, there are too many phase jumps close to the cylinder resulting in a less successful unwrapping.

## 3.5 Field maps

We have already discussed three different procedures to determine the magnetic field distortion by solving Laplace's equation. These methods rely on the given experimental parameters and are not able to include all disturbing factors like gradient nonlinearities, deviations in the main magnetic field or material imperfections. These problems can be circumvented by directly using the image information for determining the magnetic field distortions. As already mentioned a gradient echo image, in contrast to a spin echo image, also contains phase information due to field imperfections.

$$\Phi = -\gamma(B_0 + \Delta B)\sigma(T)\mathit{IE} + \gamma\Delta B\mathit{IE} + \Phi_0(T). \quad (3.5.1)$$

Here  $\Phi_0(T)$  contains temperature dependent phase contributions like changes of local conductivity which are independent of the echo time  $\mathit{IE}$ . Consequently, neglecting temperature effects for the moment, we can extract  $\Delta B$  out of the phase images of a

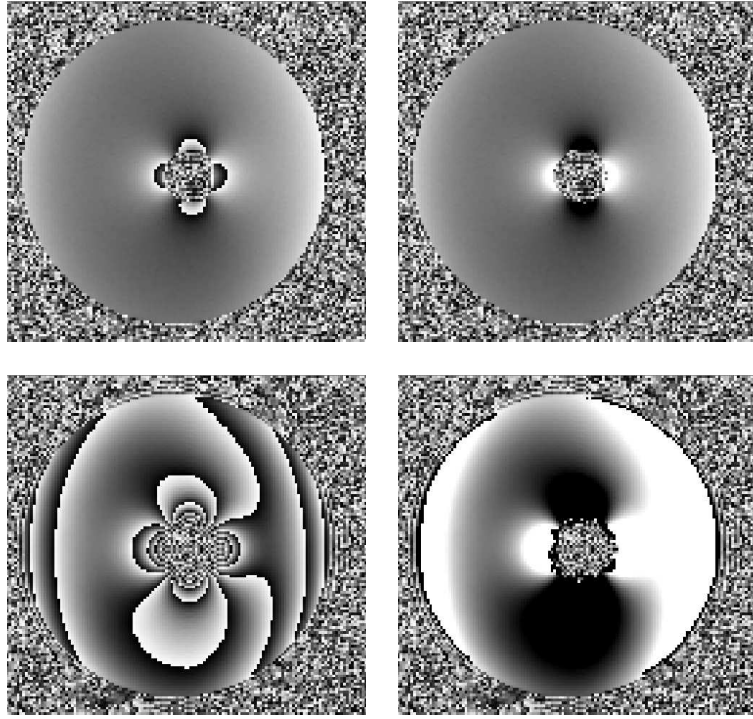


**Figure 3.21:** Result of the unwrapping algorithm for a gradient echo image (TR=600ms, FOV 400, matrix  $128 \times 256$ ). Top:  $TE = 3.77$ ms, Bottom  $TE = 20$ ms; Top left: uncorrected image; Top right: corrected image; Bottom left: uncorrected image; Bottom right: corrected image

gradient echo image.

$$\Delta B = \frac{\Phi}{\gamma TE}. \quad (3.5.2)$$

For a spin echo image this can be accomplished by adding a shifted echo after time  $\delta T$  in the sequence. Then the magnetic field distortions are obtained using a similar expression as for the gradient echo sequence.

$$\Delta B = \frac{\Phi}{\gamma \delta T}. \quad (3.5.3)$$

In this work gradient images will be used because they are already available from the temperature measuring sequence.

The phase images of a gradient echo image cannot be used directly because they have to be unwrapped first (3.4). From the unwrapped phase images we get directly the field distortions. As gradient echo images greatly suffer from image distortions the shortest possible echo time should be used for these phase maps.

### 3.6 Correction algorithms

As outlined in Sect. (2.5) magnetic field inhomogeneities lead to false frequency encoding and therefore to geometric and intensity distortions within the image. According to Sect.

(2.5.6) a field change  $\Delta B$  causes a shift from the true pixel position  $(x, y)$  to  $(x', y')$ .

$$\begin{aligned} x' &= x + \frac{\Delta B(x, y)}{G_x}, \\ y' &= y. \end{aligned} \quad (3.6.1)$$

Here we assume  $G_x$  to be the read-out gradient. There is also a change in intensity which cannot be expressed that simple. Additionally one has to take into account that as soon as several pixels are mapped onto the same new pixel position, it is impossible to recover the true intensity by back-mapping.

In principle, the distortion correction is possible both in the frequency and in the spatial domain [24].

### 3.6.1 Correction in the frequency domain

For a spin echo image the magnetization distribution  $m'(x)$  in the presence of a magnetic field inhomogeneity  $\Delta B$  is recovered for a profile in read-out direction by [28]

$$m'(x) = \frac{1}{\sqrt{2\pi}} \exp\left(-\frac{\mathbf{TE}}{T_2}\right) \int_{k_{\min}}^{k_{\max}} \left[ M_T(k_x) \exp\left(\frac{-k_x}{\gamma G_x T_2}\right) \exp\left(\frac{-ik_x \Delta B}{G_x}\right) \right] \exp(-ik_x x) dk_x, \quad (3.6.2)$$

where  $M_T(k_x)$  denotes the Fourier transform of the transverse magnetization which in the one dimensional case depends on the frequency space coordinate  $k_x$ .

In gradient echo imaging the missing refocusing pulse results in two changes: transverse relaxation takes place with  $T_2^*$  instead of  $T_2$  and there is an additional phase factor due to the field inhomogeneity

$$\begin{aligned} m'(x) &= \frac{1}{\sqrt{2\pi}} \exp\left(-\frac{\mathbf{TE}}{T_2^*}\right) \exp(-i\gamma \Delta B \mathbf{TE}) \times \\ &\times \int_{k_{\min}}^{k_{\max}} \left[ M_T(k_x) \exp\left(\frac{-k_x}{\gamma G_x T_2^*}\right) \exp\left(\frac{-ik_x \Delta B}{G_x}\right) \right] \exp(-ik_x x) dk_x \end{aligned} \quad (3.6.3)$$

Equivalently, we could transform our image into the distorted frame of reference  $x'$  resulting in an expression which is almost similar to the undistorted case. Of course, the altered relaxation of the transverse magnetization from  $T_2$  to  $T_2^*$  cannot be compensated for by a simple coordinate shift.

$$\begin{aligned} m'(x') &= \exp\left(-\frac{\mathbf{TE}}{T_2^*}\right) \exp(-i\gamma \Delta B \mathbf{TE}) \times \\ &\times \int_{k_{\min}}^{k_{\max}} \left[ M_T(k_x) \exp\left(\frac{-k_x}{\gamma G_x T_2^*}\right) \right] \exp(-ik_x x') dk_x \end{aligned} \quad (3.6.4)$$

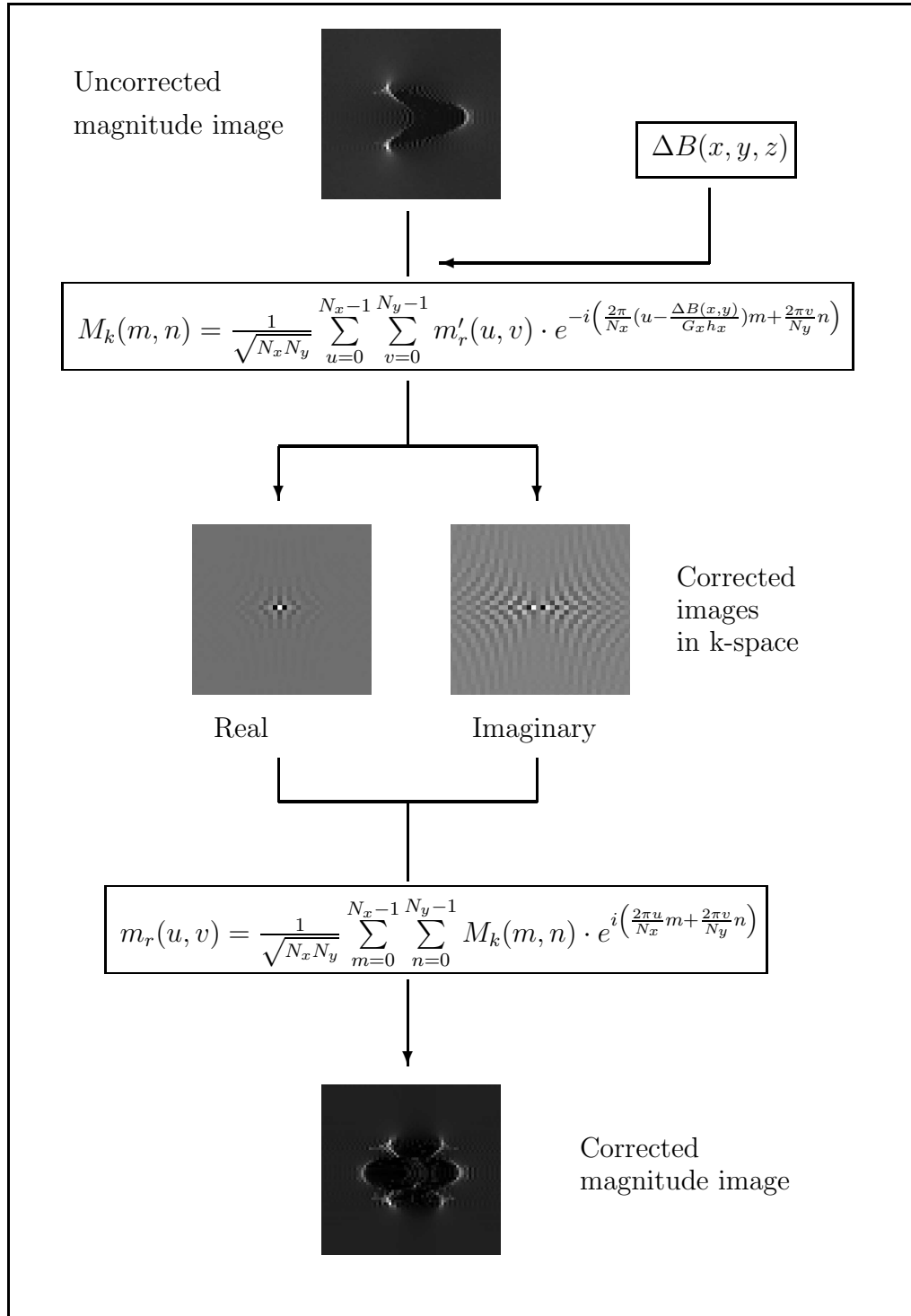


**Figure 3.22:** Correction algorithm in the frequency domain. First, the distorted image is transformed back into the frequency space by applying a Fourier transform with an inverse geometrical shift using the calculated magnetic field deviation. The corrected image is found after an inverse Fourier transform.

According to these equations it should be possible to obtain the true image by a Fourier transform of the distorted image  $m'_r(u, v)$  with the inverse shift  $\Delta x = \frac{\Delta B}{G_x}$ . For a discrete domain the transformation into the k-space with inverse shift reads

$$M_k(m, n) = \frac{1}{\sqrt{N_x N_y}} \sum_{u=0}^{N_x-1} \sum_{v=0}^{N_y-1} m'_r(u, v) \cdot e^{-i\left(\frac{2\pi}{N_x}(u - \frac{\Delta x}{N_x})m + \frac{2\pi v}{N_y}n\right)}. \quad (3.6.5)$$

Finally the corrected image  $m_r(u, v)$  can be obtained using the usual Fourier transform.

$$m_r(u, v) = \frac{1}{\sqrt{N_x N_y}} \sum_{m=0}^{N_x-1} \sum_{n=0}^{N_y-1} M_k(m, n) \cdot e^{i\left(\frac{2\pi u}{N_x}m + \frac{2\pi v}{N_y}n\right)}. \quad (3.6.6)$$

Figure 3.22 shows the basic algorithm for this correction procedure.

### 3.6.2 Correction in the spatial domain

With the help of the calculated shift in the spatial domain  $\Delta x$  it is also possible to directly correct the geometrical distortions. Figure 3.23 shows the principal procedure for  $\Delta B > 0$  and with distortions in both  $x$  and  $y$ . As in the previous section, we try to find the original magnetization distribution  $m(x, y)$  using the distorted image  $m'(x, y)$ . First, the magnetic field variation  $\Delta B(i, j)$  at the position of the pixel, which is to be corrected, is calculated delivering the geometrical shifts  $\Delta x(i, j)$  and  $\Delta y(i, j)$ . The position after a hypothetical displacement is calculated using

$$\begin{aligned} I' &= i + \Delta x(i, j), \\ J' &= j + \Delta y(i, j). \end{aligned} \quad (3.6.7)$$

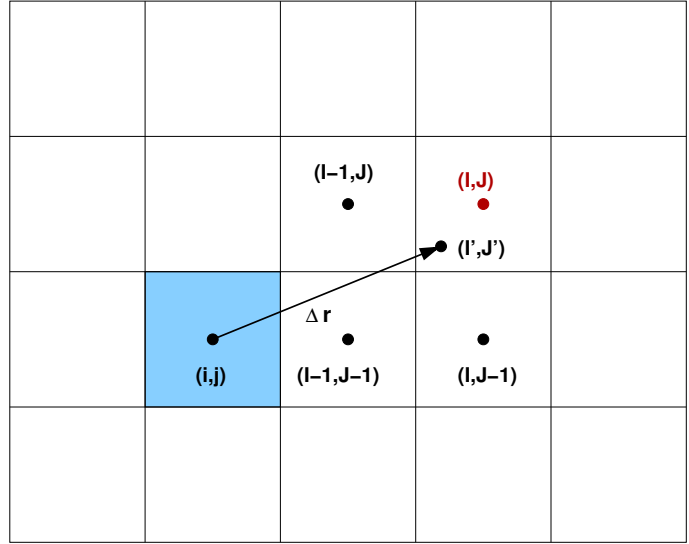
As  $\Delta x$  and  $\Delta y$  are not necessarily integer,  $I'$  and  $J'$  do not coincide with grid points. To achieve a smooth intensity distribution the pixel intensity has to be distributed somehow onto the neighbouring grid points  $(I, J)$ . A commonly used weighting scheme [38] depends on the relative position of  $(I', J')$  within the cell  $(I, J)$ . This leads to an expression for the corrected pixel intensity  $m_c(i, j)$ .

$$\begin{aligned} m_c(i, j) &= (1 - |I' - I|)(1 - |J' - J|) \cdot m'(I, J) + |I' - I|(1 - |J' - J|) \cdot m'(I - 1, J) \\ &\quad + (1 - |I' - I|)|J' - J| \cdot m'(I, J - 1) + |I' - I||J' - J| \cdot m'(I - 1, J - 1) \end{aligned} \quad (3.6.8)$$

Due to the fact that  $\Delta B$  is position dependent, the pixels are not only shifted but also slightly distorted in their shape and area. Consequently, we also have to correct for that effect. The transformation from one reference frame  $(x, y)$  to another  $(x', y')$  is mathematically accomplished by the Jacobian-matrix  $\frac{\partial(x', y')}{\partial(x, y)}$ .

$$\begin{pmatrix} x' \\ y' \end{pmatrix} = \frac{\partial(x', y')}{\partial(x, y)} \begin{pmatrix} x \\ y \end{pmatrix} \quad (3.6.9)$$

**Figure 3.23:** Distortion correction in the spatial domain for  $\Delta B > 0$  and distortions in  $x$  and  $y$ . Using the calculated shifts  $\Delta B(i, j)/G_x$  and  $\Delta B(i, j)/G_y$  the new pixel index  $(I', J')$  is determined as a real number. As a next step, the index is rounded to the discrete values of the grid yielding the new pixel position after the shift  $(I, J)$ . Due to the rounding, this would lead to a very rough estimate of the real distortion, of course. Therefore, the new pixel intensity is weighted with a factor which is influenced by the intensities of the neighboring pixels according to the deviation of the calculated real index to the rounded value. Finally, the obtained pixel value is assigned to the pixel  $(i, j)$ .



with

$$\frac{\partial(x', y')}{\partial(x, y)} = \begin{pmatrix} \frac{\partial x'}{\partial x} & \frac{\partial x'}{\partial y} \\ \frac{\partial y'}{\partial x} & \frac{\partial y'}{\partial y} \end{pmatrix} = \begin{pmatrix} 1 + \frac{\partial(\Delta B(x, y))}{G_x \cdot \partial x} & \frac{\partial(\Delta B(x, y))}{G_x \cdot \partial y} \\ \frac{\partial(\Delta B(x, y))}{G_y \cdot \partial x} & 1 + \frac{\partial(\Delta B(x, y))}{G_y \cdot \partial y} \end{pmatrix} \quad (3.6.10)$$

The change of the pixel area is given by the determinant of the Jacobian matrix.

$$dxdy = \left| \frac{\partial(x', y')}{\partial(x, y)} \right| dx' dy' \quad (3.6.11)$$

with

$$\begin{aligned} \left| \frac{\partial(x', y')}{\partial(x, y)} \right| &= \begin{vmatrix} \frac{\partial x'}{\partial x} & \frac{\partial x'}{\partial y} \\ \frac{\partial y'}{\partial x} & \frac{\partial y'}{\partial y} \end{vmatrix} = 1 + \frac{\partial(\Delta B(x, y))}{G_y \cdot \partial y} + \frac{\partial(\Delta B(x, y))}{G_x \cdot \partial x} \\ &\quad + \frac{\partial(\Delta B(x, y))}{G_x \cdot \partial x} \frac{\partial(\Delta B(x, y))}{G_y \cdot \partial y} - \frac{\partial(\Delta B(x, y))}{G_y \cdot \partial x} \frac{\partial(\Delta B(x, y))}{G_x \cdot \partial y}. \end{aligned}$$

Restricting ourselves to first order in  $\Delta B$  we get

$$\left| \frac{\partial(x', y')}{\partial(x, y)} \right| \approx 1 + \frac{\partial(\Delta B(x, y))}{G_y \cdot \partial y} + \frac{\partial(\Delta B(x, y))}{G_x \cdot \partial x}. \quad (3.6.12)$$

Thus, the final corrected image is given by

| matrix  | spatial domain [s] | frequency domain [s] |
|---------|--------------------|----------------------|
| 256×128 | 0.7                | 444.6                |

**Table 3.1:** Computing times for correction in the spatial domain(SD) and in the frequency domain(FD)

$$m(i, j) = m_c(i, j) \cdot \left| \frac{\partial(x', y')}{\partial(x, y)} \right|_D \quad (3.6.13)$$

with the discretized form of the determinant and  $h_x$  and  $h_y$  the original pixel size

$$\left| \frac{\partial(x', y')}{\partial(x, y)} \right|_D = 1 + \frac{\Delta B(i+1, j) - \Delta B(i-1, j)}{G_x \cdot 2h_x} + \frac{\Delta B(i, j+1) - \Delta B(i, j-1)}{G_y \cdot 2h_y}. \quad (3.6.14)$$

### 3.7 Comparison between different correction algorithms

For the correction of geometric image distortions two methods have been proposed: correction in the spatial domain and correction in the frequency domain. Applying both methods to distorted images of the phantom film can filled with different materials we compare them with respect to accuracy and performance.

In the case of weak distortions, e.g. for an air-filled cylinder ( $\chi = 0.38 \cdot 10^{-6}$ ), both algorithms yield similar good results (Fig. 3.24). For stronger distortions present in the case of a titanium cylinder ( $\chi \approx -180.7 \cdot 10^{-6}$ ) however, the two algorithms behave differently (Fig. 3.25). While the correction in the frequency domain is not able to correct for the strong distortions as it just mirrors the arrow-like structure, the spatial correction shows good results and is able to reproduce the correct geometry. Nevertheless, there are still insufficiencies in the intensity of the image. Even though the area of the cylinder should appear black as it does not give any signal, the corrected image shows similar intensities both inside and outside the cylinder.

From the point of view of computing time the correction in the spatial domain is superior to the correction in the frequency domain as the second one is about a factor of 500 slower than the first one which can be seen in Tab. 3.1 for a grid of 256×128 grid points. This is due to the inefficiency of the Fourier transform with Fourier shift which cannot be handled by standard fast Fourier transform routines. Thus, spatial correction is the most favorable method both in terms of correction results and computation times.

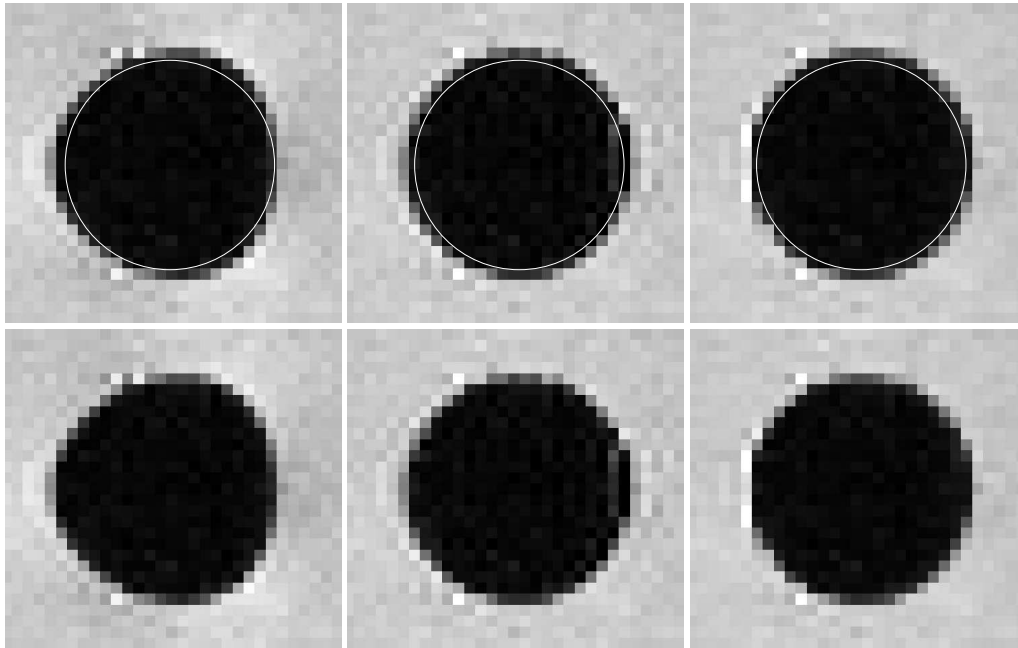


**Figure 3.24:** Comparison of different correction algorithms. The magnetic field was calculated with the Fourier transform method; From left to right: uncorrected image, correction in the spatial domain, correction in the frequency domain. In the top images the real cylinder is indicated by a white circle.

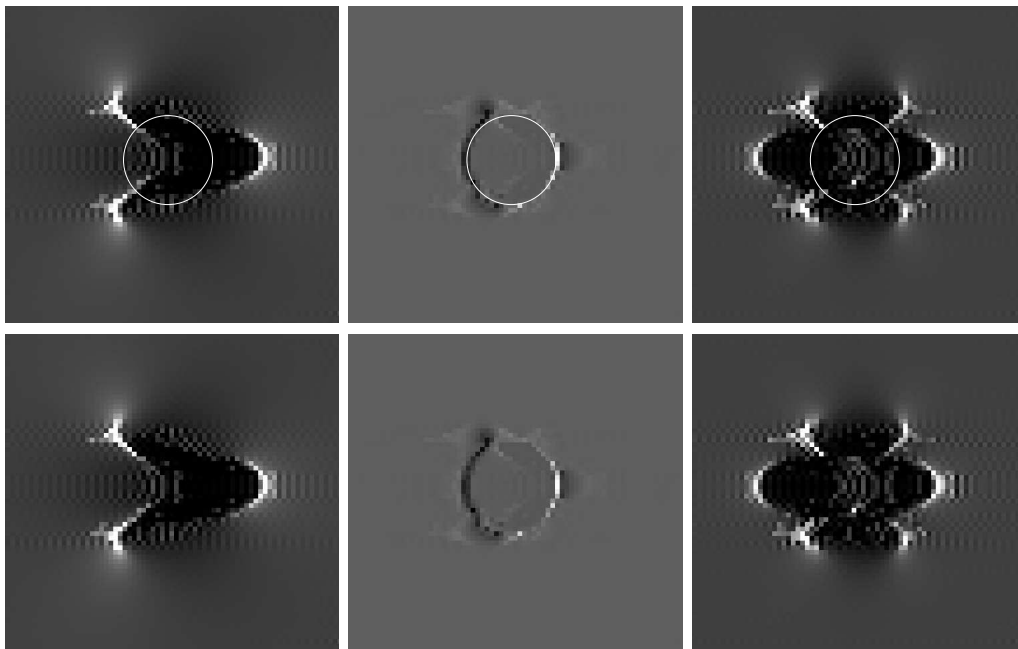


**Figure 3.25:** Left: Forward simulation using the Fourier transform method; Middle: corrected image with spatial correction; Right: corrected image with frequency correction. In the top images the real cylinder is indicated by a white circle.



### 3.8 Subsumption

Now the basic numerical techniques required for this work are known. It has been shown that the Fourier transformation is the preferred method for the calculation of the magnetic field both in terms of accuracy and CPU time. All further numerical evaluations will therefore concentrate on this method.

A new phase unwrapping algorithm has been presented and shown to deliver good results applied to experimental data. Finally two correction procedures for the removal of geometrical distortions were proposed and tested. Both were able to reproduce the main geometry of the object. Nevertheless, the spatial domain procedure is regarded as superior because of its high speed.



## 4 Experimental results

After some insight into the theoretical background and an introduction of the used numerical methods, experimental data is needed to validate the numerical results. In this chapter the basic experimental procedures as well as related technical aspects will be explained. Furthermore, the acquired data is evaluated concerning the major questions of this work.

### 4.1 Experimental setup

The experiments were performed on a Siemens Magnetom Symphony 1.5 T whole-body system (Siemens Medical Solutions, Erlangen, Germany) equipped with a hyperthermia radio-frequency treatment system [15].

For temperature measurements MR compatible temperature probes (Bowman thermistors; BSD Medical Corp.) were used. Processing the MR data to map temperatures was accomplished with the software platform AMIRA (Indeed Visual Concepts, Berlin, Germany). As imaging objects two different phantoms were built to meet the special requirements for this project (Fig. 4.1). The first, afterwards referenced as phantom film can, consisted of a water filled round plastic box (inner diameter 18.9 cm) with an air filled film can (inner diameter 3 cm) glued to the bottom in the centre of the box. The second, afterwards referenced as phantom condom, was built up out of a rectangular plastic box (bottom: (22×16)cm, top: (25.4×19.5)cm) with an air filled condom glued to the bottom in the approximate centre of the box. In contrast to the film can in phantom 1 the condom could move freely because only one end was connected to the box.



**Figure 4.1:** Left: water filled phantom consisting of a round plastic box (diameter 18.9cm), inside an air filled film can (inner diameter 3cm) is glued to the bottom of the box; Right: water filled phantom consisting of a rectangular plastic box (bottom: (22×16)cm, top: (25.4×19.5)cm) where an air filled condom is glued to the bottom, but can move freely inside the water.

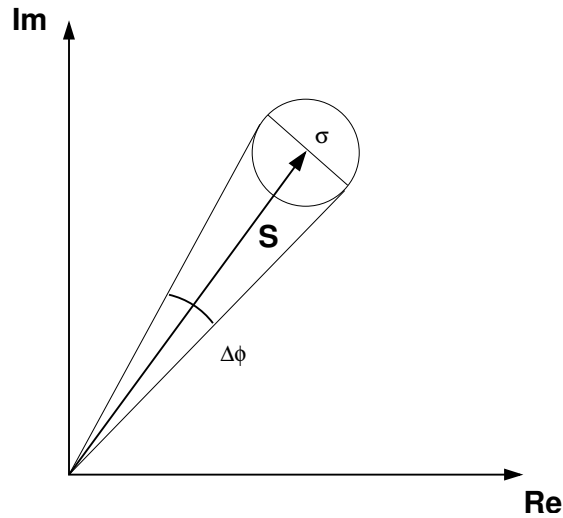


**Figure 4.2:** Connection between the standard deviation of the noise and the phase precision.

The aim of this experimental work can be divided into two parts.

- Delivering images as a basis for the numerical simulations
- Examination of susceptibility induced artifacts and temperature changes

For these purposes the following strategies were used:

- Imaging with constant temperature and high signal-to-noise-ratio for comparison with the numerical results
- Different fillings of the cylinder
- Filling the phantoms with hot water and observe the cooling process.
- Using different combinations of two echo times
- Using different image resolutions
- Imaging with constant temperature over several time steps

## 4.2 Technical aspects

### 4.2.1 Signal-to-noise-ratio

For the acquisition of the temperature images the same sequences as for the usual hyperthermia treatment were used. A  $T_1$  weighted turbo spin echo ( $TE = 12\text{ms}$ ,  $TR = 701\text{ms}$ , slice thickness  $5\text{mm}$ , matrix  $256 \times 256$ , 5 averages) with varying field of view was used for

the localisation of the temperature probes and the geometric proportions. The temperature information was extracted out of the phase images of a double echo gradient echo sequence (TR=600ms) with the help of an AMIRA module.

For the validation of the numerical results the signal-to-noise-ratio (SNR) had to be taken into account. If we want to detect very small phase changes we need a very good SNR. Figure 4.2 shows the correlation between the variance of the signal due to noise  $\sigma$  and the phase resolution  $\Delta\varphi$ . For small  $\sigma$  and the signal strength  $S$  the relation

$$\Delta\varphi = \sigma \cdot S \quad (4.2.1)$$

holds. The SNR of an image is given by

$$\text{SNR} = \frac{\bar{S}_{\text{signal}}}{\sigma} = \frac{\sum_{\text{ROI}} \left( \frac{S_{\text{signal}}}{N_{\text{ROI}}} \right)}{\sqrt{\frac{\sum_{\text{ROI}} (S_{\text{noise}} - \bar{S}_{\text{noise}})^2}{N_{\text{ROI}}}}}, \quad (4.2.2)$$

where  $\bar{S}_{\text{signal}}$  denotes the average value of the signal intensity within the region of interest (ROI) with good signal properties, i.e. few noisy pixels, and  $\sigma$  contains the standard deviation of the intensity within a noisy ROI. Comparison with (4.2.1) gives us the relationship between the achievable phase precision and the SNR of the acquired image.

$$\Delta\varphi \propto \frac{1}{\text{SNR}}. \quad (4.2.3)$$

If we now consider a magnetic field deviation of approximately  $10^{-7}$  T this leads to a minimum phase precision of approximately 0.1 rad. Hence, a correct evaluation of these effects requires a resolution of (0.01 – 0.05) rad and consequently a minimum SNR of 50-100. There are several ways to improve the SNR, among which are special choices of receiving coils, changes in pixel size as well as image averaging.

Up to now a simple body coil was used for the experiments. Even though it covers a big area and gives a very homogeneous signal the intensity is relatively poor. Hence, for further experiments a birdcage head coil was used which is especially designed for the geometry of the head being comparable to the shape of the phantom film can. The SNR increases with growing voxel size. Unfortunately this also lowers the resolution which is essential in the vicinity of the cylinder wall. Therefore the achievable gain using this option is rather limited. For the last possibility, several images of the same object are acquired and averaged to give the final image. If we repeat a measurement  $N_{\text{acq}}$  times we get for the signal and the noise

$$\bar{S}_{\text{av}} = \frac{1}{N_{\text{acq}}} \sum_{\text{acq}} \bar{S} \quad , \quad \sigma_{\text{av}} = \frac{\sigma}{\sqrt{N_{\text{acq}}}}.$$

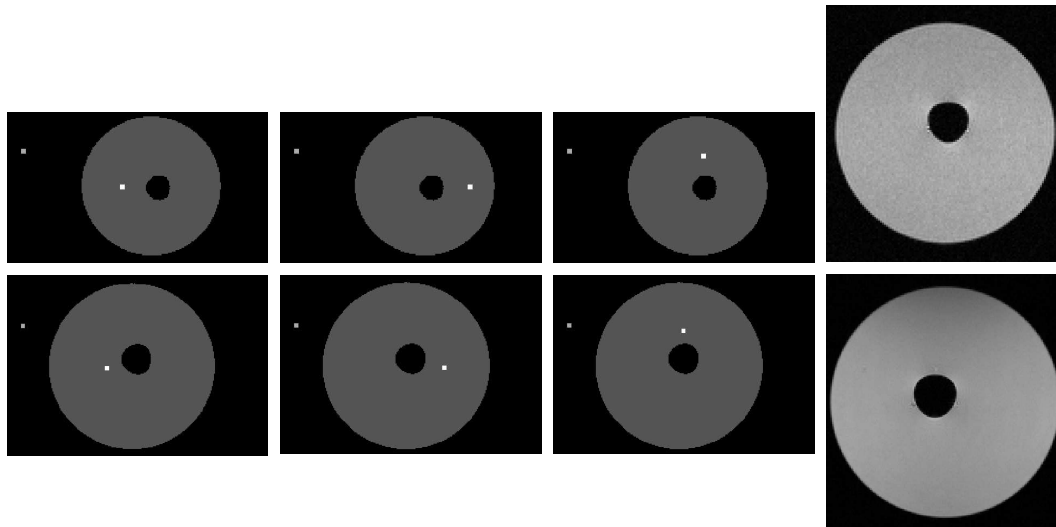


**Figure 4.3:** ROIs for the calculation of the SNR. Top: TR=600ms, FOV:  $(400 \times 200) \text{mm}^2$ , 16 slices à 8mm, no averages, body coil; SNR from left to right: 60,56,61; Bottom: TR=600ms, FOV:  $(280 \times 192) \text{mm}^2$ , 10 slices à 5.5mm, 2 averages, head coil; SNR from left to right: 117,105,118.

In total this leads to an increase in SNR by a factor of  $\sqrt{N_{\text{acq}}}$  but also to a longer scan time. The changed gradient echo sequence (TR=600ms, FOV:  $(280 \times 192) \text{mm}^2$ , 10 slices à 5.5mm, 2 averages, head coil) showed a sufficient SNR for detailed phase measurements (Fig. 4.3).

#### 4.2.2 Readout bandwidth

The image distortions are mainly dependent on the change in the magnetic field due to susceptibility differences and on the readout gradient (2.5). As we cannot influence the susceptibility distribution, we have to focus on the gradients. Changing the readout bandwidth is one possibility to alter the gradient. Figure 4.4 shows the effect of different readout gradients and bandwidths. Obviously, the same pixel size is achievable with different gradient strengths as well as with different bandwidths. Therefore, an increased readout bandwidth should have the same effect as an increased gradient and lead to less distortions (Fig. 4.5). Unfortunately this effect is also accompanied by a decrease in SNR. Nevertheless this approach can be useful to determine the true geometry of the imaged object which is crucial for the correct calculation of the magnetic field.

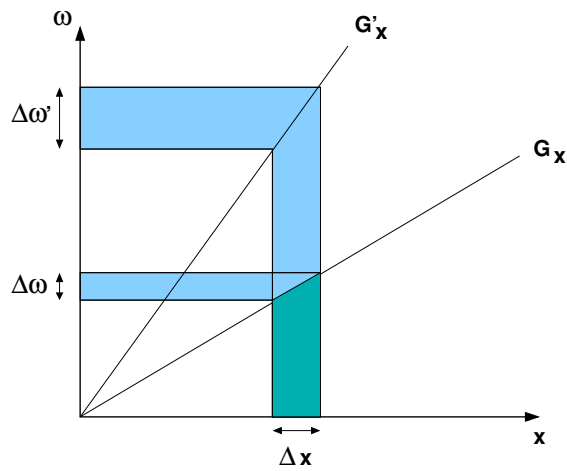


**Figure 4.4:** Connection between readout gradient  $G_x$ , readout bandwidth  $\Delta\omega$  and resolution in the readout direction  $\Delta x$ . Obviously, an increased readout bandwidth has the same effect as an increased readout gradient.

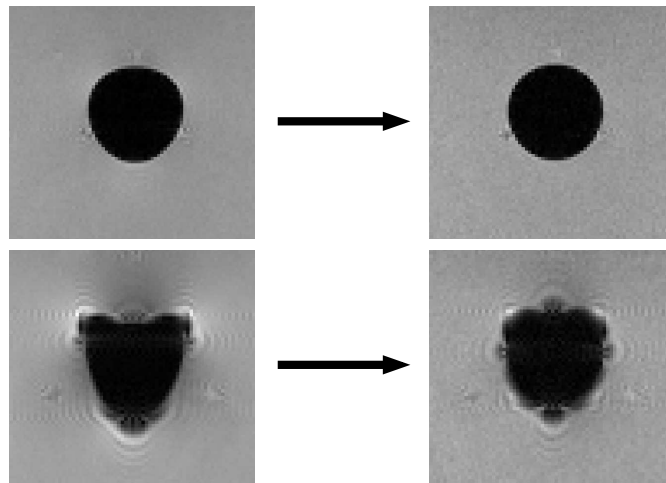


**Figure 4.5:** Gradient echo images of the phantom film can be acquired with different readout bandwidths (TR=600ms, TE=3.77ms, FOV:(280×192)mm<sup>2</sup>, 10 slices à 5.5mm); Left: 260Hz/pixel; Right: 930Hz/pixel; Top: air-filled cylinder( $\chi = 0.38 \cdot 10^{-6}$ ); Bottom: cylinder filled with a Magnevist-solution (Schering GmbH,  $\chi \approx 50 \cdot 10^{-6}$ ).

### 4.2.3 Different susceptibilities

For the observation of image distortions the phantom film can with different cylinder materials was used. As the objective of the experiments was to examine the influence of air-filled areas in the human body mostly an air-filling was used. The susceptibility and its temperature dependence are known from literature [41]. The area around the cylinder was always filled by normal water whose susceptibility value is also known in detail (2.8.8). As a second cylinder filling a Magnevist-solution (Schering GmbH) was used. The determination of its susceptibility was difficult because its dependency on the actual concentration of the Magnevist-solution and the added water volume. The commonly available Magnevist-solution has a molar susceptibility of  $\chi_{Magn}^m = 2.7 \cdot 10^{-2} \text{mol}^{-1}$  and contains  $n_{Magn} = 0.5 \text{mol}$  pure Magnevist per litre. This solution was diluted such that we took  $(9.5 \pm 0.5) \text{ml}$  Magnevist-solution and filled the rest of the cylinder with ordinary water. Thus, the susceptibility of the solution can be calculated knowing the diameter and height of the cylinder

$$\begin{aligned} d &= (2.9 \pm 0.05) \text{cm} \\ h &= (4.4 \pm 0.1) \text{cm} \\ V_{\text{cyl}} &= \frac{\pi d^2}{4} h = (29.1 \pm 1.7) \text{cm}^3 \\ V_{\text{Magn}} &= (9.5 \pm 0.5) \text{cm}^3 \\ V_{\text{water}} &= (19.6 \pm 2.2) \text{cm}^3 \end{aligned}$$

as the weighted sum of the susceptibilities of the commercial Magnevist solution and of the added water.

$$\begin{aligned} \chi_{\text{sol}} &= \frac{V_{\text{Magn}}}{V_{\text{cyl}}} \cdot \chi_{\text{Magn}} + \frac{V_{\text{water}}}{V_{\text{cyl}}} \cdot \chi_{\text{water}} = 35.8 \cdot 10^{-6} \\ \chi_{\text{Magn}} &= n_{\text{Magn}} \cdot V_{\text{Magn}} \cdot \chi_{\text{Magn}}^m \end{aligned}$$

The uncertainty for the susceptibility can be estimated by standard error analysis

$$\begin{aligned} \Delta \chi_{\text{sol}} &= \left| \frac{2V_{\text{Magn}}}{V_{\text{cyl}}} n_{\text{Magn}} \chi_{\text{Magn}}^m \Delta V_{\text{Magn}} \right| + \left| - \left( \frac{V_{\text{Magn}}^2}{V_{\text{cyl}}^2} n_{\text{Magn}} \chi_{\text{Magn}}^m + \frac{V_{\text{water}}}{V_{\text{cyl}}^2} \chi_{\text{water}} \right) \Delta V_{\text{cyl}} \right| \\ &\quad + \left| \frac{\Delta V_{\text{water}}}{V_{\text{cyl}}} \chi_{\text{water}} \right| = 1.7 \cdot 10^{-6} \end{aligned}$$

leading to the final result

$$\chi_{\text{sol}} = (35.8 \pm 1.7) \cdot 10^{-6}. \quad (4.2.4)$$



| step | time     | $T_{\text{film can}} [^{\circ}\text{C}]$ | time     | $T_{\text{condom}} [^{\circ}\text{C}]$ |
|------|----------|------------------------------------------|----------|----------------------------------------|
|      | 00:00:00 | 45.0                                     | 00:00:00 | 44.5                                   |
| 1    | 00:05:08 | 42.4                                     | 00:06:17 | 43.2                                   |
| 2    | 00:10:16 | 40.5                                     | 00:12:34 | 42.0                                   |
| 3    | 00:15:24 | 38.9                                     | 00:18:52 | 41.0                                   |
| 4    | 00:20:32 | 37.5                                     | 00:25:09 | 40.0                                   |
| 5    | 00:25:40 | 36.1                                     | 00:31:27 | 39.1                                   |
| 6    |          |                                          | 00:47:45 | 38.2                                   |
| 7    |          |                                          | 00:44:02 | 37.4                                   |
| 8    |          |                                          | 00:50:20 | 36.6                                   |
| 9    |          |                                          | 00:56:37 | 35.9                                   |

**Table 4.1:** Temperature as a function of time measured by temperature probes inside the phantoms

## 4.3 Evaluation of the imaging series

### 4.3.1 Temperature dependency of the image artifacts

As already mentioned in Sect. (2) the PRF method is only suitable for the calculation of temperature differences. Therefore the evaluation of a time series requires a reference point for the temperature.

Theoretically the resulting temperature differences should be independent of this choice. Practically we also have to take into account changes in the geometry, produced for example by any kind of motion between successive image acquisitions. Figure 4.6 shows images of the phantom film can acquired over a range of 26 minutes. The calculated temperature information is shown with respect to the first time step as reference (top), the last time step as reference (bottom), respectively. Note that for this cooling process the first time step shows the highest temperature. For comparison the temperature was also measured by a temperature probe inside the water (Tab. 4.1). For both image series the reference image is not shown as it does not include any temperature changes.

A comparison of both image sequences shows no remarkable change in the size of the artifacts produced by the air in the central area. As the film can was a rigid body this is not surprising because displacements of the air-water boundary were impossible. To examine motion of the object and changes of the shape of the air-water interface, next we consider the phantom condom (Fig. 4.1) for which the temperature change with time can be found in Tab. 4.1. For the sake of clarity only the time steps 1,3,5 and 9 are shown as image (Fig. 4.7). Here we can find slight differences between the two rows. Obviously, the artifacts induced by the object are growing with increasing time distance with respect to the reference image (Fig. 4.8). This leads to an arrow-like artifact around the condom which become the more pronounced, the longer the time differences with respect to the reference image are. This effect is not really surprising because the method requires the geometry of the object to be constant in time. Of course a moving object cannot fulfil this. Even though this effect is relatively small

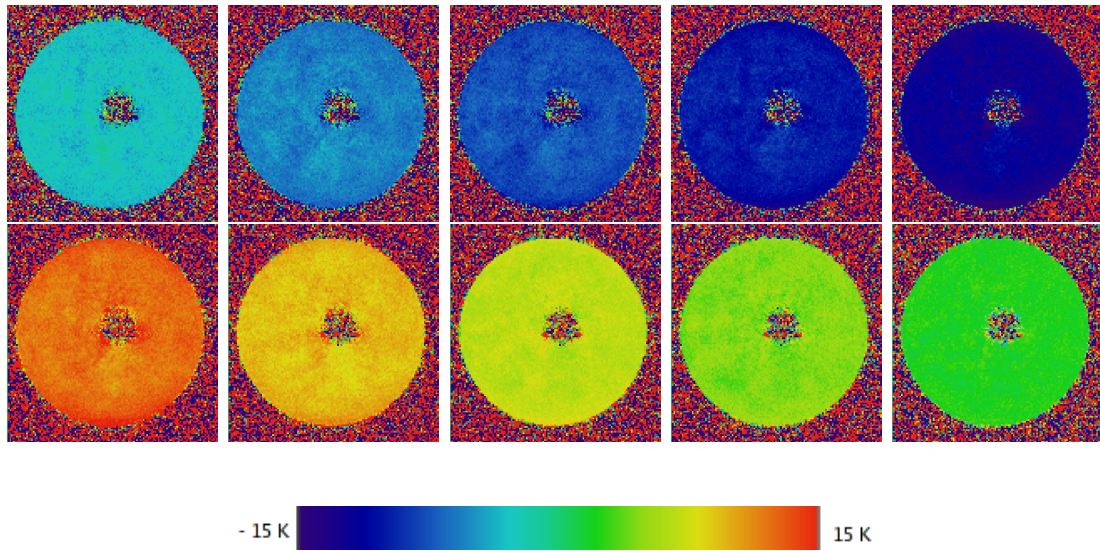


**Figure 4.6:** Double echo gradient echo images ( $TE = (5.48/20)$ ms,  $TR=600$ ms, 16 slices à 8mm, matrix  $(128 \times 256)$ , FOV:  $(200 \times 400)$ mm<sup>2</sup>, coronar) of the phantom film can; top: first time step as reference, bottom: last time step as reference.

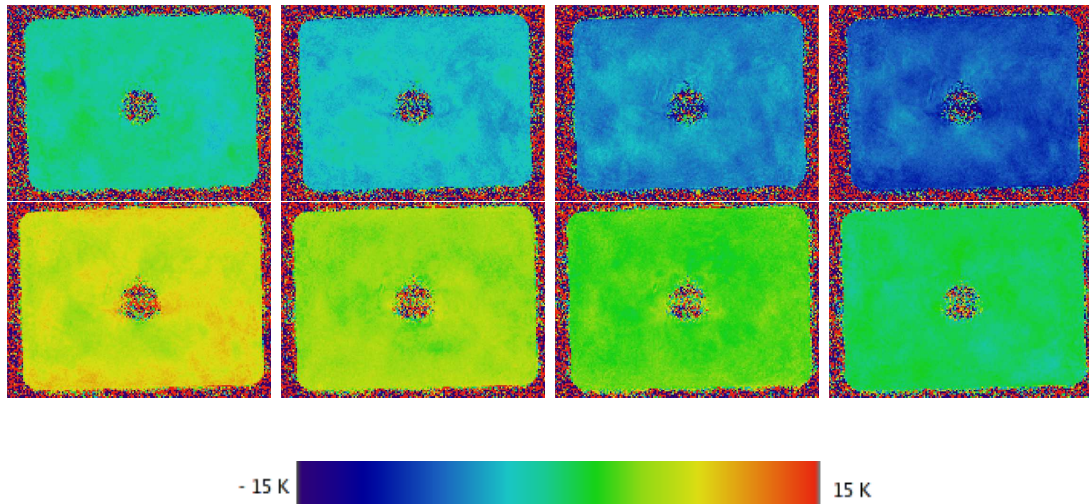


**Figure 4.7:** Double echo gradient echo images ( $TE = (5.48/20)$ ms,  $TR=600$ ms, 16 slices à 8mm, matrix  $(176 \times 256)$ mm<sup>2</sup>, FOV:  $(275 \times 400)$ mm<sup>2</sup>, coronar) of the phantom condom; top: first time step as reference, bottom: last time step as reference.

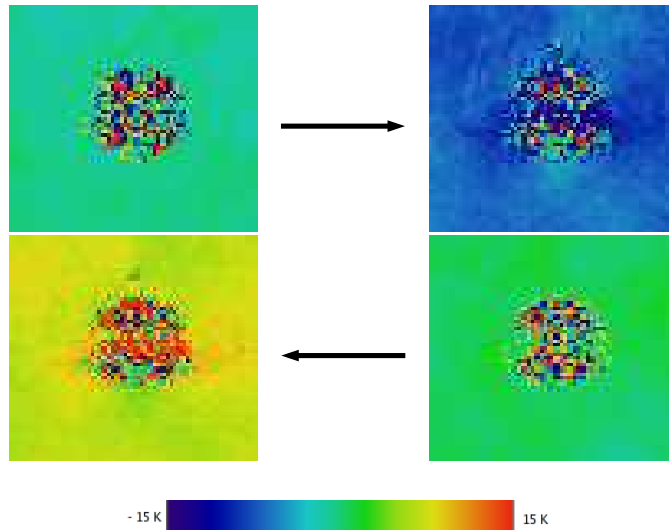


**Figure 4.8:** Zoom into the central region of the first and the last image of each row in Fig. 4.7. Apparently the size of the artifact increases with growing time difference with respect to the reference image and develops an arrow like shape; top: first image as reference, bottom: last image as reference.

it allows for a principle distinction. This way, we can examine, if artifacts are related to temperature or just arise from other sources like inter-acquisitional motion and the resulting mismatching between successive acquisitions and the reference image.

While these results indicate a connection between the matching with the reference image and the size of the artifacts, influences of the changing temperature cannot be completely precluded. Therefore a second experiment without active temperature change was performed (Fig. 4.9). The first two rows show temperature images of phantom film can (first row) and phantom condom (second row) calculated with the last image as reference. The same images are displayed in the last two rows but with the first image as reference. Immediately one can see the effect of motion in the images of the phantom condom. The induced artifacts obviously grow with increasing time difference between the actual and the reference image and form cones of rays around the moving cylinder. In contrast, the images of the phantom film can show almost no distortions. As there is no influence of temperature any more we can conclude that mismatching effects due to inter-acquisitional motion of the object have dominated the formation of image artifacts in our experimental setup. Another interesting aspect in these images is that despite the constant temperature a change in colour is visible. The cause for this is the existence of a main magnetic field drift  $B_D$  which is increasing with imaging time and was not corrected in these experiments. This topic will be further discussed in Sect. (5.2.2).

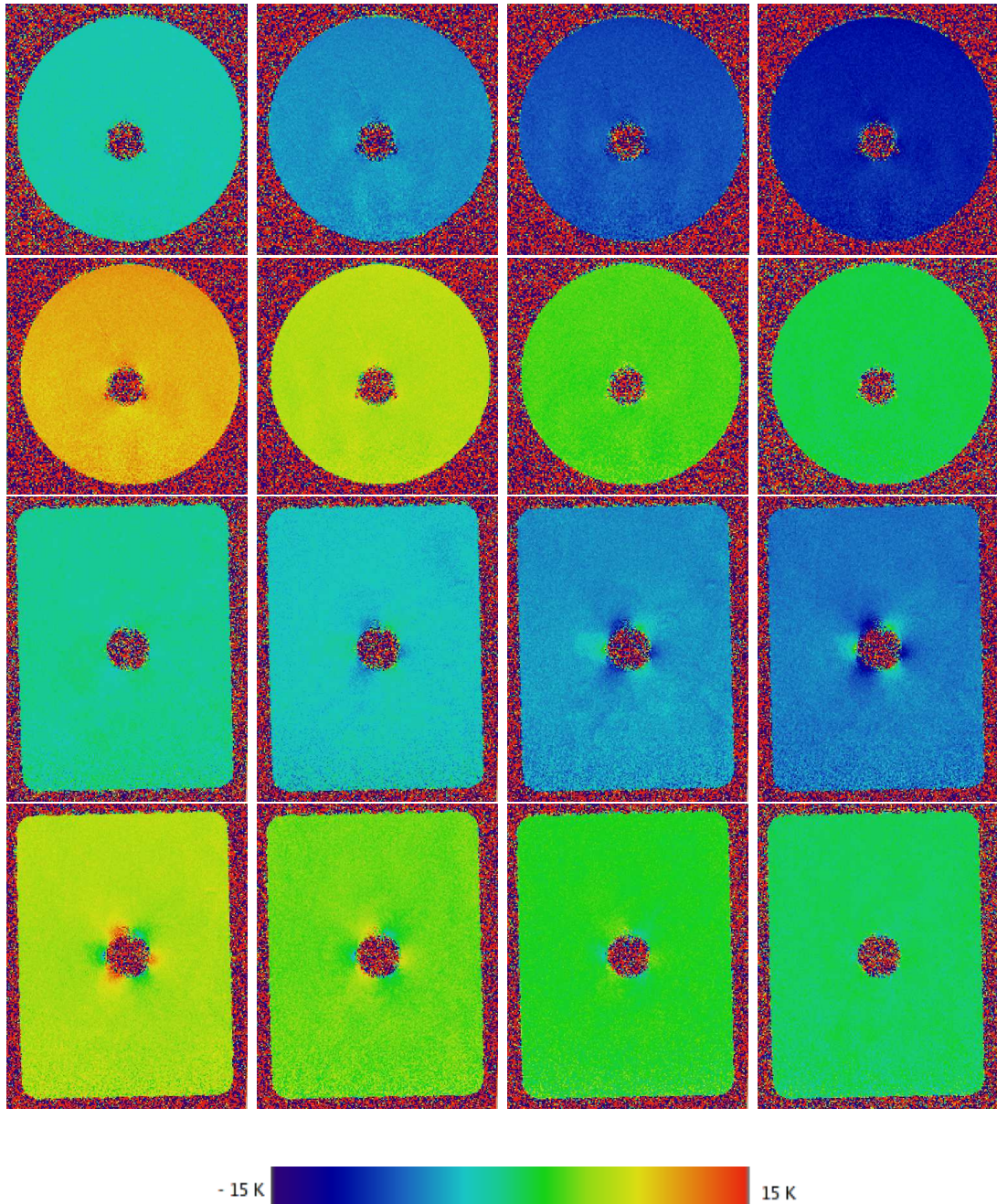


**Figure 4.9:** Double echo gradient echo images ( $TE = (5.48/20)$ ms,  $TR=600$ ms, 16 slices à 8mm, coronar) for constant temperature; First and second row: phantom film can, matrix  $176 \times 256$ , FOV of  $(192 \times 280)$ mm<sup>2</sup>, temperature  $(21.2 \pm 0.3)$  °C, first (first row) and last (second row) images as temperature reference; Third and fourth row: phantom condom, matrix  $192 \times 256$ , FOV  $(210 \times 280)$ mm<sup>2</sup>, temperature  $(21.1 \pm 0.2)$  °C, first (third row) and last (fourth row) images as reference.

| condom   | time     | T <sub>128</sub> [°C] | time     | T <sub>192</sub> [°C] | time     | T <sub>256</sub> [°C] |
|----------|----------|-----------------------|----------|-----------------------|----------|-----------------------|
|          | 00:00:00 | 41.5                  | 00:00:00 | 41.7                  | 00:00:00 | 42.1                  |
|          | 00:03:23 | 40.8                  | 00:03:23 | 41.2                  | 00:03:23 | 41.5                  |
|          | 00:06:46 | 40.2                  | 00:06:47 | 40.4                  | 00:06:46 | 40.8                  |
|          | 00:10:09 | 39.7                  | 00:10:10 | 39.9                  | 00:10:09 | 40.0                  |
|          | 00:13:32 | 39.0                  | 00:13:33 | 39.2                  | 00:13:32 | 39.5                  |
|          | 00:16:55 | 38.4                  | 00:16:56 | 38.6                  | 00:16:55 | 39.0                  |
| film can | time     | T <sub>128</sub> [°C] | time     | T <sub>192</sub> [°C] | time     | T <sub>256</sub> [°C] |
|          | 00:00:00 | 40.1                  | 00:00:00 | 41.3                  | 00:00:00 | 41.6                  |
|          | 00:04:02 | 38.7                  | 00:04:02 | 39.7                  | 00:04:02 | 40.2                  |
|          | 00:08:04 | 38.2                  | 00:08:04 | 38.5                  | 00:08:04 | 39.0                  |
|          | 00:12:05 | 37.2                  | 00:12:05 | 36.7                  | 00:12:06 | 37.5                  |
|          | 00:16:07 | 35.9                  | 00:16:07 | 35.6                  | 00:16:07 | 36.5                  |
|          | 00:20:09 | 35.3                  | 00:20:09 | 35.6                  | 00:20:09 | 36.0                  |

**Table 4.2:** Top: Temperature inside the phantom condom measured by a temperature probe; Bottom: Temperature inside the phantom film can measured by a temperature probe.

### 4.3.2 Influence of the image resolution on image artifacts and temperature information

In the performed examination, for clinical daily work time is an important factor. Therefore, it is desirable to shorten the acquisition time of an image for example by reducing the matrix size. Of course, this will also impair the image quality. But does it also influence image artifacts and temperature resolution? Figure 4.10 shows the same temperature development for quadratic matrix sizes of 128, 192 and 256 for a cooling process over approximately 20 minutes (Tab. 4.2). The first three rows show images of the phantom film can, whereas the last three rows display acquisitions of the phantom condom. An obvious difference is of course the lower image quality with decreasing resolution. The images with matrix size 128 cannot even resolve the cylinder boundary properly. Besides that there seems to be no correlation between the artifact size due to mismatching effects and the resolution. Consider a longer time series, this behaviour changes. In Fig. 4.11 a cooling process over 1h with the condom phantom is displayed (Tab. 4.3). Here, we can see clearly that the artifacts due to motion of the condom are growing with increasing time. The fact that this effect only occurs on very long time scales indicates that the effect is small compared to the influence of motion as seen before.

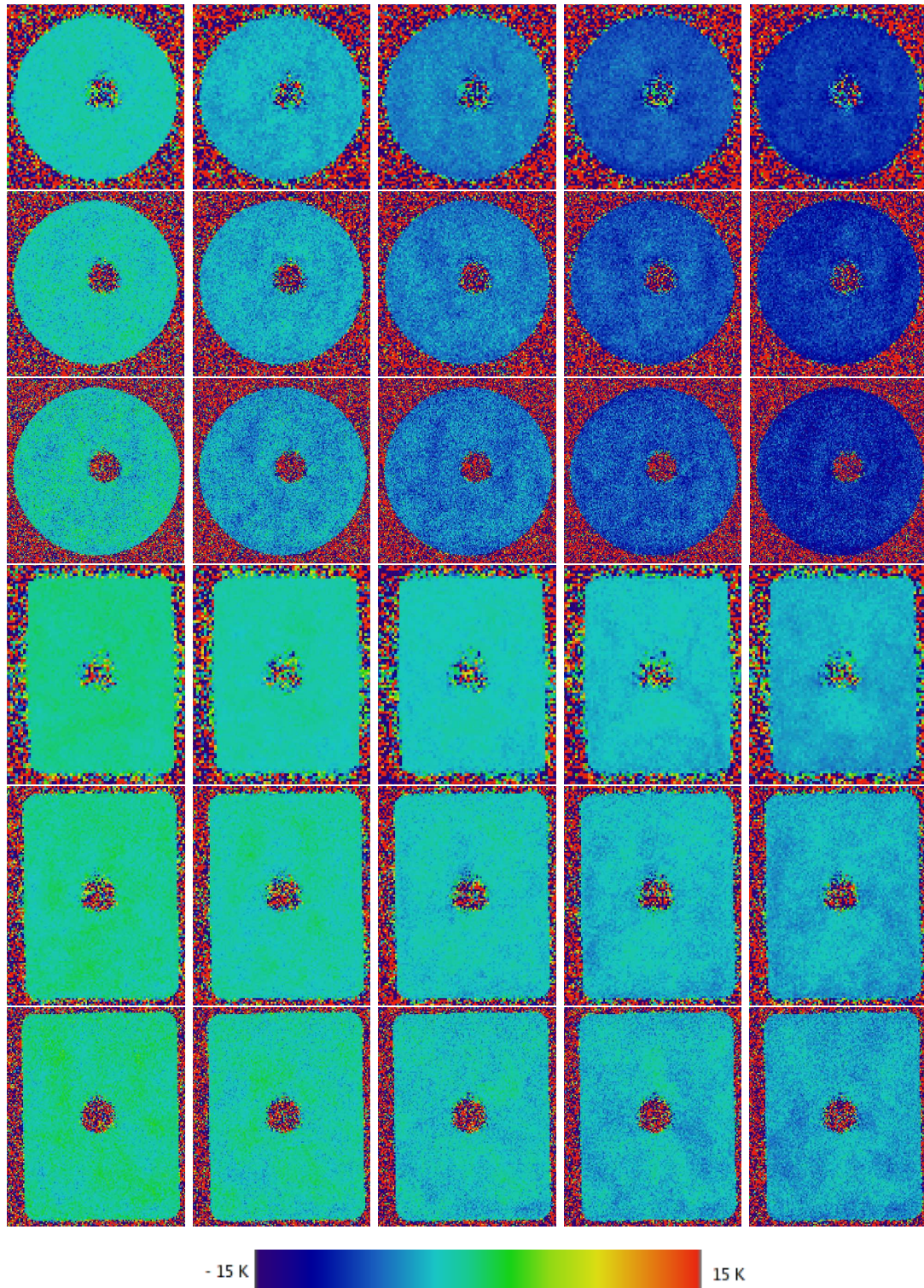


**Figure 4.10:** Double echo gradient echo images ( $TE = (5.48/20)\text{ms}$ ,  $TR=600\text{ms}$ , 16 slices à 5.5mm,  $FOV=(168 \times 300)\text{mm}^2$ , coronar) for a cooling process over 20 minutes (Tab. 4.2). Two different phantoms and three different image resolutions were used; first three rows: phantom film can (matrix:  $88 \times 128$ ,  $128 \times 192$ ,  $176 \times 256$ ); last three rows: phantom condom (matrix:  $72 \times 128$ ,  $112 \times 192$ ,  $144 \times 256$ ).

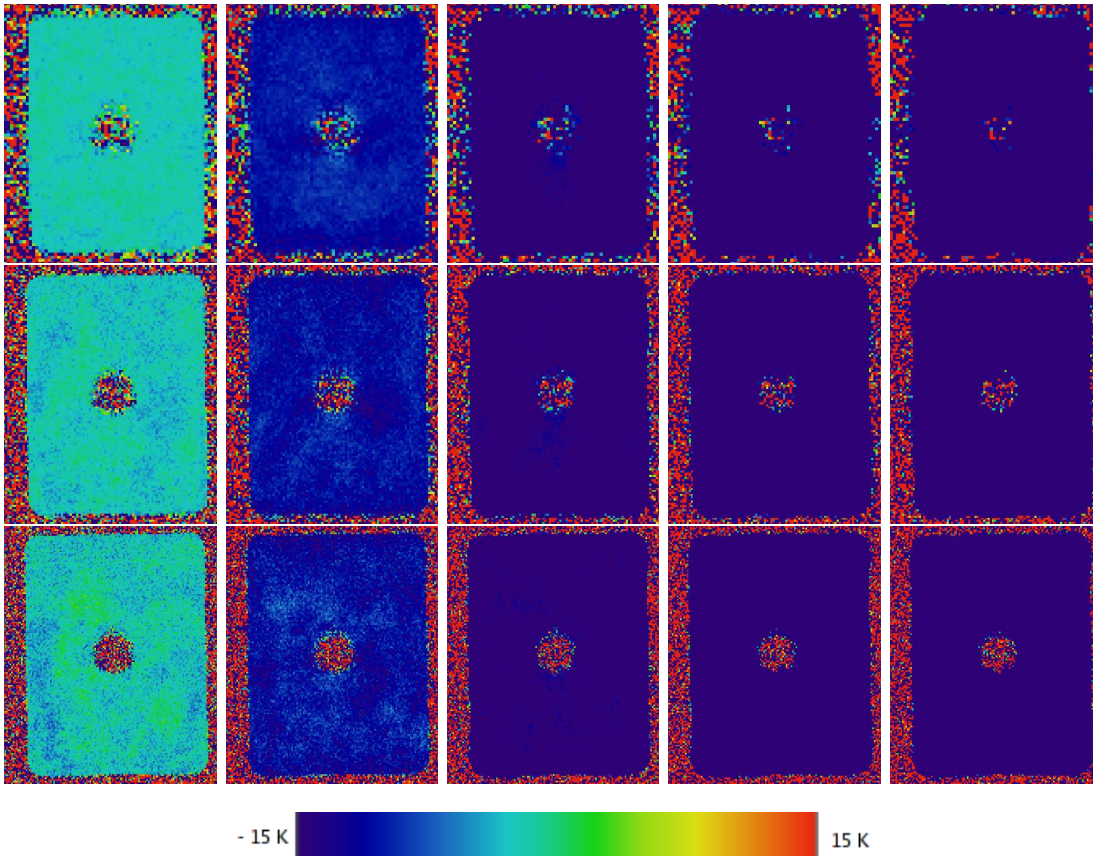


**Figure 4.11:** Double echo gradient echo images ( $TE=(5.48/20)$ ms,  $TR=600$ ms, 16 slices à 5.5mm,  $FOV=(168\times 300)$ mm<sup>2</sup>, coronar) for a cooling process over approximately 1 h (Tab. 4.3). For the phantom condom three different image resolutions were used:  $72\times 128$ ,  $112\times 192$ ,  $144\times 256$ .

| time     | $T_{128}$ [°C] | time     | $T_{192}$ [°C] | time     | $T_{256}$ [°C] |
|----------|----------------|----------|----------------|----------|----------------|
| 00:00:00 | 55.1           | 00:00:00 | 55.7           | 00:00:00 | 56.1           |
| 00:03:24 | 53.3           | 00:03:23 | 54.2           | 00:03:23 | 54.6           |
| 00:16:56 | 48.6           | 00:16:56 | 49.0           | 00:16:55 | 49.6           |
| 00:30:29 | 44.7           | 00:30:29 | 45.2           | 00:30:28 | 45.5           |
| 00:44:02 | 41.5           | 00:44:01 | 41.7           | 00:44:01 | 42.1           |
| 01:00:57 | 38.4           | 01:00:57 | 38.6           | 01:00:56 | 39.0           |

**Table 4.3:** Time dependence of water temperature for measurements with different image sizes using temperature probes.

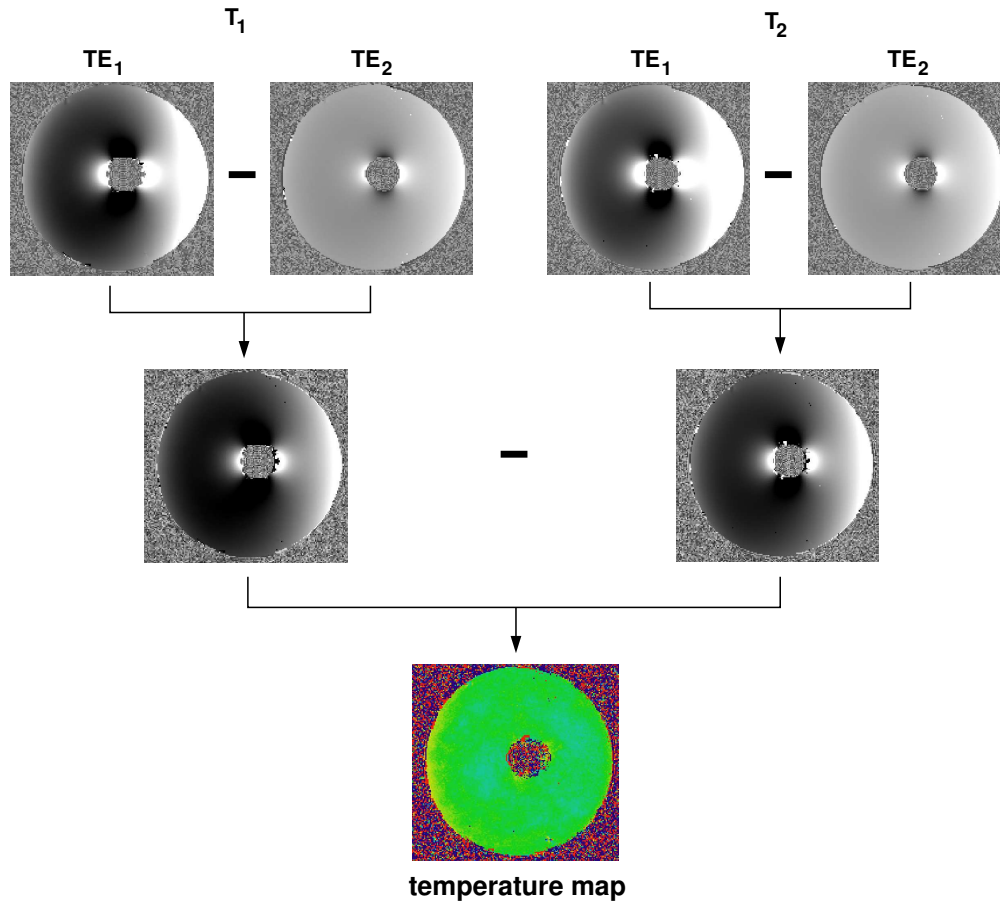
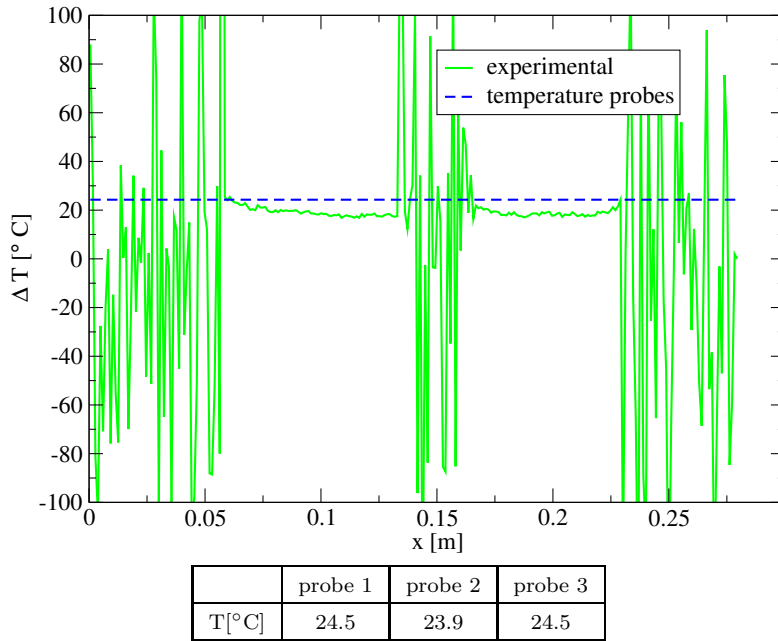


Figure 4.12: Calculation of the temperature difference with the PRF double echo method.

### 4.3.3 Comparison between experimental acquired temperature maps and temperature probes

The usual way to acquire temperature maps with MRI was outlined in Sect. (2.6.3). The phantom film can was filled with hot water to image the cooling process over 20 time steps. Using the knowledge from Sect. (4.2.1), double echo gradient echo images with high SNR were acquired every 3min 30s. The real temperature development was monitored by three MR compatible temperature probes inside the water-filled box (Fig. 4.13, Tab. 4.4). For comparison the temperature difference between the first and the last image was calculated. For this purpose the two phase images with different echo times but equal temperature were subtracted. The actual temperature difference between the two acquisitions is given by the subtracted phase images for the two different temperatures (Fig. 4.12). The right hand side of Fig. 4.14 shows the resulting temperature differences for a cut through the centre of the cylinder along the  $x$ -axis. Compared to the





**Figure 4.14:** Comparison between the experimental acquired temperature difference and the measured temperature difference along a line through the centre of the cylinder for  $y=\text{const}$  and after 70min of cooling. The measured temperatures for the three different probes are given in the table below.

averaged temperature probe measurements of  $(24.3 \pm 0.1)^\circ\text{C}$ , here the calculated results generally underestimate the temperature by approximately  $6^\circ\text{C}$  in the inner parts of the box and  $3^\circ\text{C}$  in the outer parts. Figure 4.16 shows a histogram of the temperature distribution throughout the whole centre slice after 70min of cooling. As some of the pixels show peak values of up to  $6700^\circ\text{C}$  and down to  $-1000^\circ\text{C}$  an upper and lower threshold of  $0^\circ\text{C}$  and  $40^\circ\text{C}$  were set. As a result 4080 pixels were discarded. The remaining 14914 pixels showed an averaged temperature value of  $19.00^\circ\text{C}$  with a standard deviation  $\sigma = 1.37^\circ\text{C}$ . These values are also in agreement with the observed profile from Fig. 4.14. According to the observations in Sect. (4.3.1) artifacts in temperature images arise from a bad matching between the actual and the reference image due to inter-acquisitional motion. Figure 4.15 also shows an increasing deviation with growing time difference to the reference image. As an effect the experimental and measured temperatures for the first data point almost coincide within the margins of error whereas the last data point shows a deviation of  $5^\circ\text{C}$  compared to the measurements of the temperature probes.

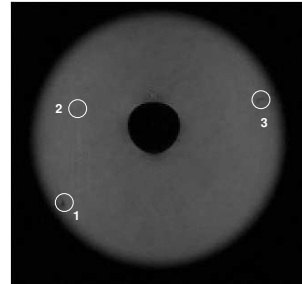


**Figure 4.13:** Position of the temperature probes inside the water-filled box of the phantom film can.

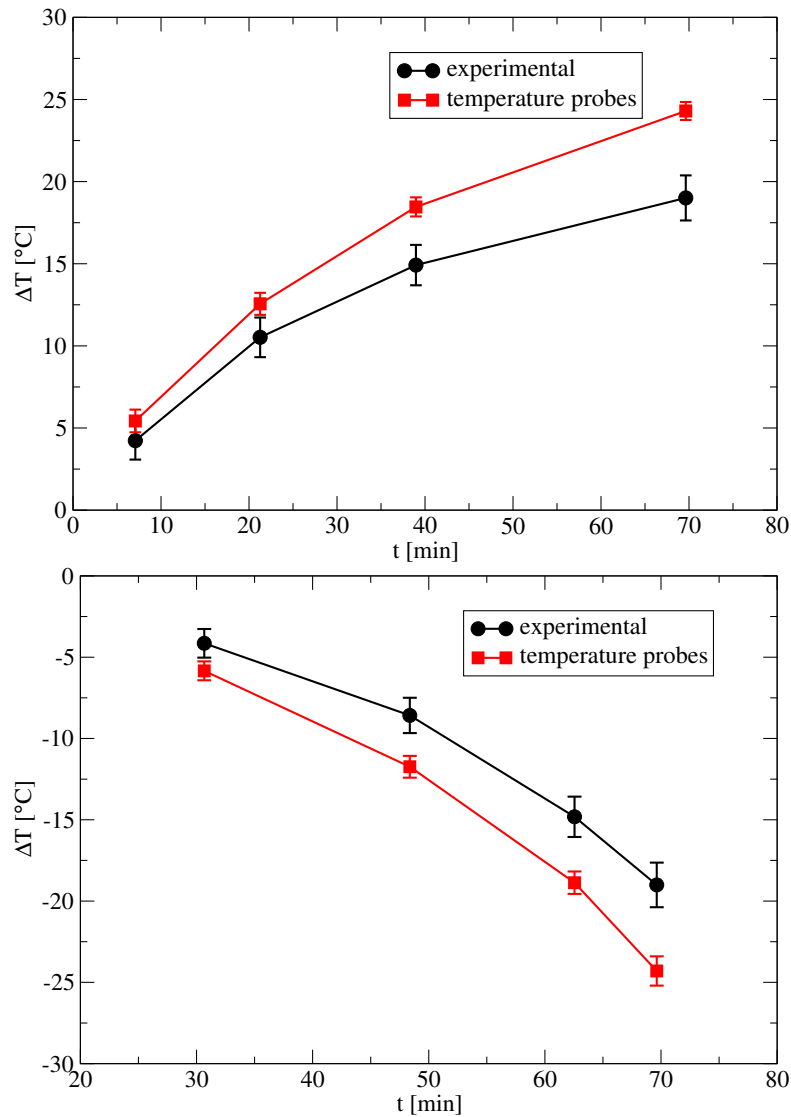


**Figure 4.15:** Temperature development with time for the temperatures measured by temperature probes and for the experimentally acquired data. Top: first image as reference; Bottom: last image as reference.

The comparison between the results for different reference images also proves that this effect is not related to the temperature itself but as already mentioned is caused by mismatching. In this particular case the mismatch gets worse with increasing time. The calculated temperatures are also influenced by a change in the thermal load of the shim-coils leading to a temperature dependent drift of the main magnetic field. It has been reported that this is usually the main source for temperature errors in the absence of motion [14]. As outlined in Sect. (2.8) magnetic field inhomogeneities caused by susceptibility changes also lead to false temperature measurements. A further discussion

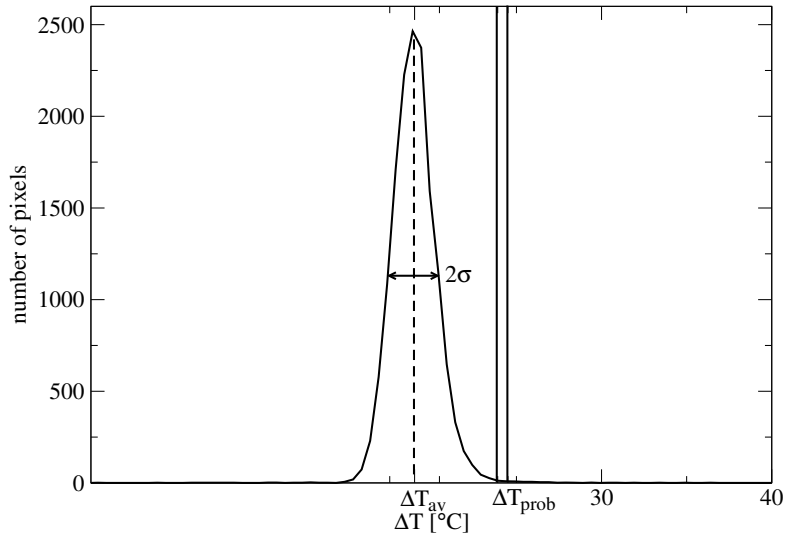


**Figure 4.16:** Histogram of the temperature distribution in the middle slice for a cooling process after 70min. 4080 pixels were discarded because they showed temperatures below  $0^{\circ}C$  or above  $40^{\circ}C$ . The remaining 14914 pixels had an averaged temperature value of  $19.01^{\circ}C$  with a standard deviation  $\sigma = 1.37^{\circ}C$ .

of both effects will be given in Sect. (5.2.2). Finally, an inhomogeneous temperature distribution and cooling process within the box will also lead to deviations from the expected results. These variations only have a minor influence but can be monitored by the standard deviation of the temperatures measured by the temperature probes.

| time     | T probe 1[°C] | T probe 2[°C] | T probe 3[°C] | $\bar{T}$ [°C] |
|----------|---------------|---------------|---------------|----------------|
| 00:00:00 | 55.7          | 54.2          | 55.8          | 55.23          |
| 00:03:33 | 53.0          | 51.6          | 52.9          | 52.50          |
| 00:07:05 | 50.2          | 49.0          | 50.2          | 49.70          |
| 00:10:38 | 48.3          | 47.2          | 48.5          | 48.00          |
| 00:14:10 | 46.3          | 45.0          | 46.3          | 45.87          |
| 00:17:43 | 44.8          | 43.6          | 45.1          | 44.50          |
| 00:21:16 | 43.0          | 41.9          | 43.1          | 42.67          |
| 00:24:48 | 41.9          | 40.7          | 41.9          | 41.50          |
| 00:28:21 | 40.4          | 39.3          | 40.5          | 40.07          |
| 00:31:53 | 39.4          | 38.3          | 39.5          | 39.07          |
| 00:35:26 | 38.2          | 37.1          | 38.3          | 37.87          |
| 00:38:58 | 37.1          | 36.1          | 37.1          | 36.77          |
| 00:42:31 | 36.4          | 35.5          | 36.4          | 36.10          |
| 00:46:03 | 35.5          | 34.5          | 35.4          | 35.13          |
| 00:49:36 | 34.8          | 33.8          | 34.8          | 34.47          |
| 00:53:08 | 33.9          | 33.0          | 34.0          | 33.63          |
| 00:56:41 | 33.4          | 32.5          | 33.4          | 33.10          |
| 01:00:13 | 32.7          | 31.7          | 32.7          | 32.37          |
| 01:06:06 | 31.7          | 30.8          | 31.7          | 31.40          |
| 01:09:38 | 31.2          | 30.3          | 31.3          | 30.93          |

**Table 4.4:** Time dependence of the water temperatures measured by the temperature probes.

## 4.4 Subsumption

In this chapter the experimental setup and applied sequences were explained. The influence of quantities like the SNR, the readout bandwidth and the susceptibility of the imaged objects on the image quality was discussed to find optimal imaging parameters. Finally a detailed examination of the acquired temperature series has proven that the observed artifacts mainly arise from inter-acquisitional motion and the resulting bad matching between successive temperature images. A direct correlation between the size of the artifacts and the temperature could not be detected. Similarly a decrease in resolution did not have any severe impact on the artifact strength. The comparison of temperature maps acquired by the proton resonance frequency method with temperatures measured by temperature probes showed large deviations. This can be explained by temperature dependent magnetic field shifts  $B_D$  as well as by susceptibility induced magnetic field inhomogeneities  $\Delta B$ .

# 5 Results

After the basic theoretical, numerical and experimental aspects of this work have been described, this chapter will compare the different methods for several applications and rate their suitability.

## 5.1 Comparison between numerical and experimental results

### 5.1.1 Magnetic field

The results for magnetic field distortions from numerical simulations using the Fourier transform technique and from experimentally acquired phase maps are compared in Fig. 5.1. The magnetic field which has been calculated from just one phase map shows a field shift which is generally increased by approximately  $3\mu\text{T}$  and evolves differently with growing distance from the cylinder. This is not surprising because this phase map also contains effects of the magnetic field shimming prior to the measurement. That is why, according to the proposal in [36], another experiment was implemented in which the water filled box was imaged both with an air-filled cylinder in the centre and with a water-filled cylinder. The resulting images were subtracted to obtain the field only due to the cylinder alone (Fig. 5.2). In contrast to the first case these results are in good agreement with the simulation.

The same experiment was carried out with the Magnevist-solution described in Sect. (4.2.3) ( $\chi = (35.8 \pm 1.7) \cdot 10^{-6}$ ) inside the cylinder (Fig. 5.3). The large uncertainty in the determination of the susceptibility of the Magnevist-solution leads to deviations of up to  $8 \cdot 10^{-7} \text{ T}$  between the simulated and the experimental magnetic field. This is because the calculated magnetic field is proportional to the susceptibility change at the border of the cylinder. Hence it is very sensitive to susceptibility deviations. There is also a small shift between the two records. The exact position of the cylinder could not be determined exactly because of the large distortions in this area. Nevertheless the deviation is at maximum only  $5\mu\text{T}$  directly at the edge of the cylinder.

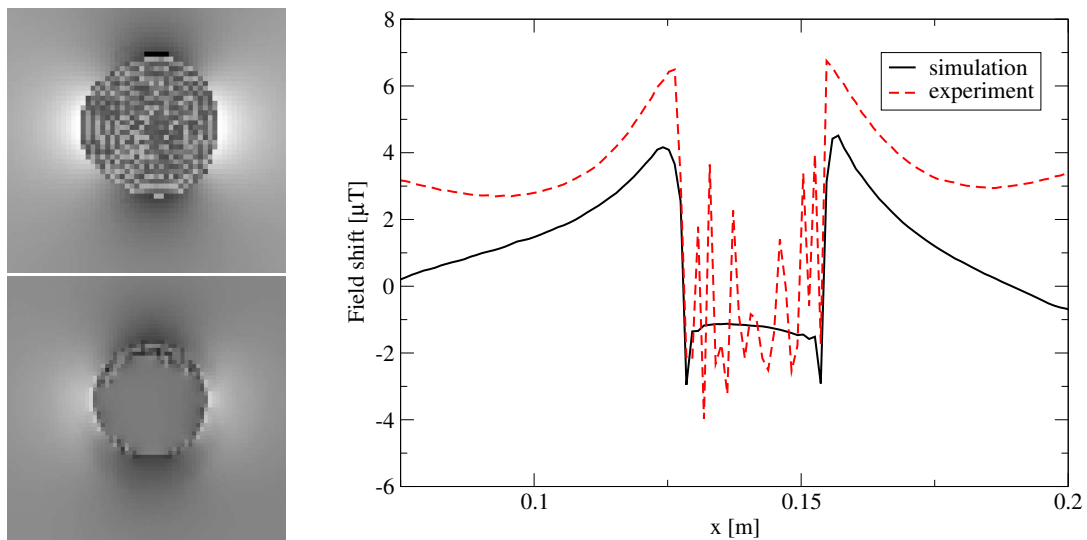


**Figure 5.1:** Left: Magnetic field of an air-filled cylinder from an experimental acquired phase image ( $TE = 3.77\text{ms}$ ,  $TR=600\text{ms}$ , 10 slices à  $5.5\text{mm}$ ,  $FOV:(280 \times 192)\text{mm}^2$ , matrix:  $256 \times 176$ , 2 averages) (top) and simulated using Fourier transform techniques (bottom); Right: Cut through the centre of the cylinder along the readout direction  $x$ .

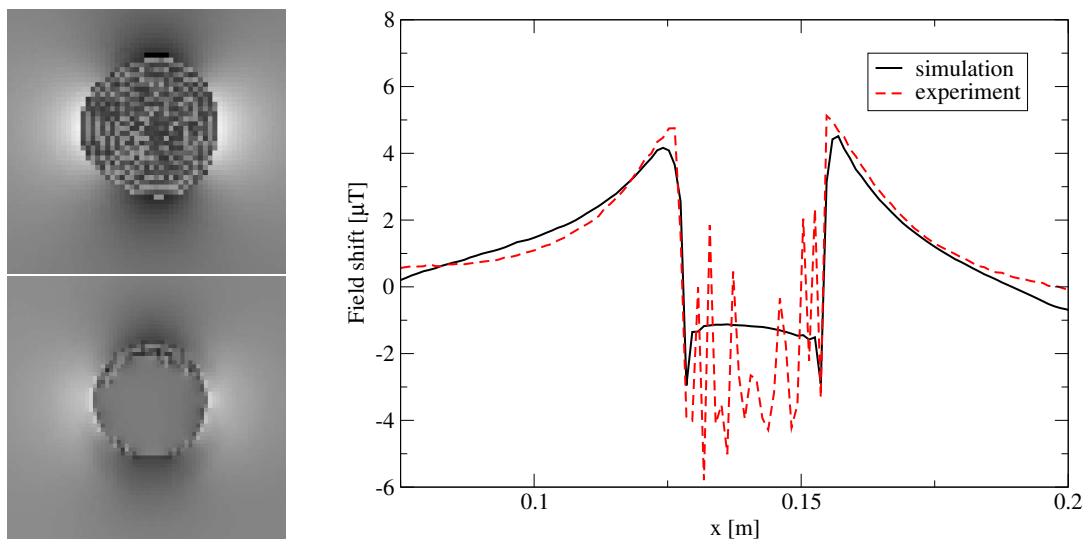


**Figure 5.2:** Left: Magnetic field of an air-filled cylinder from phase which was calculated by subtracting two phase images, with and without disturbing object ( $TE = 3.77\text{ms}$ ,  $TR=600\text{ms}$ , 10 slices à  $5.5\text{mm}$ ,  $FOV:(280 \times 192)\text{mm}^2$ , matrix:  $256 \times 176$ , 2 averages) (top) and simulated using Fourier transform techniques (bottom); Right: Cut through the centre of the cylinder along the readout direction  $x$ .

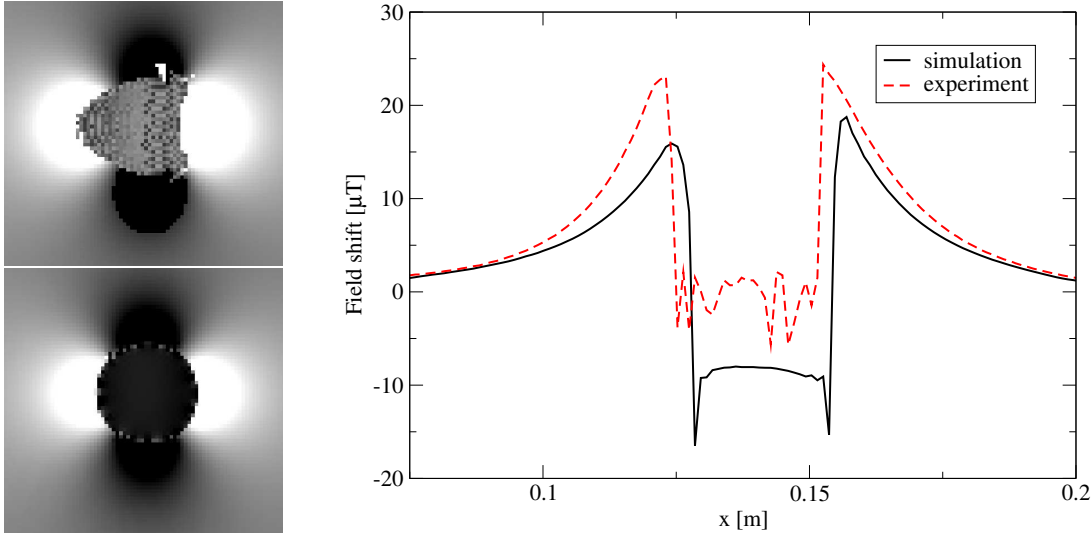


**Figure 5.3:** Left: Magnetic field of an cylinder filled with Magnevist-solution that was derived from phase values which were calculated by subtracting two phase images, with and without disturbing object ( $TE = 3.77/10.8\text{ms}$ ,  $TR=600\text{ms}$ , 10 slices à  $5.5\text{mm}$ ,  $FOV:(280 \times 192)^2\text{mm}$ , matrix: $256 \times 176$ , 2 averages) (top) and simulated using Fourier transform techniques (bottom); Right: Cut through the centre of the cylinder along the readout direction  $x$ .

## 5.2 Correction of temperature maps

### 5.2.1 Validation of the correction algorithm

In Sect. (2.8) the influence of magnetic field inhomogeneities on temperature maps and one possible correction method have been introduced. By applying the developed and validated methods for the determination of the magnetic field deviation we can now estimate the resulting effects. We will both determine the difference between two phase maps simulated without taking into account the field deviations due to different susceptibilities and in consideration of these effects including the temperature dependence of  $\chi$ . As a first test we apply a radial temperature gradient of

$$T_2(\vec{r}) = 10^\circ\text{C} - \frac{R}{20} \cdot \sqrt{(\vec{r} - \vec{r}_0)^2} \text{ } ^\circ\text{C}$$

to a constant temperature of  $37^\circ\text{C}$ . Here  $R$  denotes the size of the heated area ( $R = 1.925\text{cm}$ ) and  $\vec{r}_0$  marks the centre of the simulated area. Figures 5.4 and 5.5 compare the temperature correction both for the assumption of a linear temperature dependence of  $\chi$  and for the true relationship. The absolute value of the maximum deviation for the linear assumption is in the range of 2% which corresponds to the statement in [37] where an effect of less than 5% was observed. Both methods are comparable for this setup with pure water. Figures 5.6 and 5.7 show the same temperature distribution with changed setup. In this case an air-filled cylinder of radius  $1.5\text{cm}$  in the centre is surrounded by water. The correction procedure is carried out as before with the same

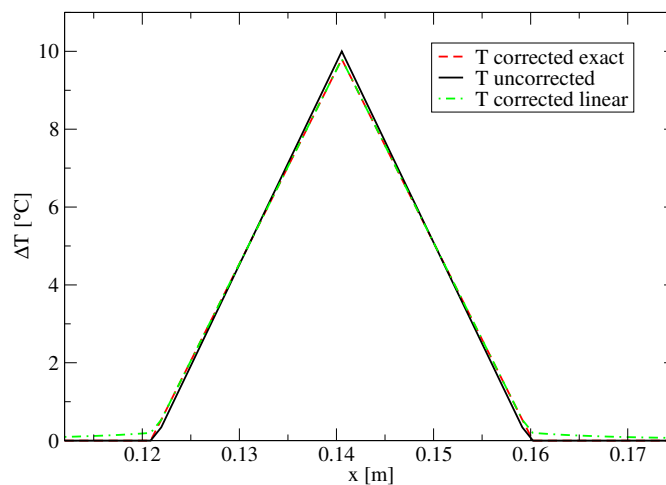


**Figure 5.4:** Comparison between the acquired temperature maps for a forward pass with correct temperature dependence of the susceptibilities, for the correction procedure with assumed linear temperature dependence of  $\chi$  and for the uncorrected case. The medium is water.

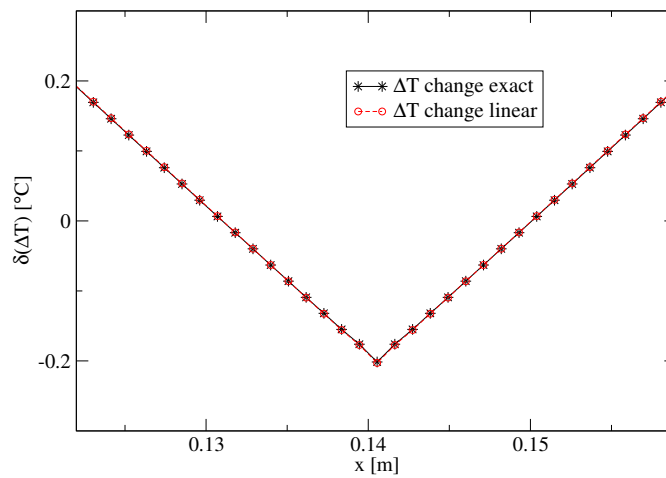


**Figure 5.5:** Difference between corrected and uncorrected temperature differences  $\delta(\Delta T)$  for the forward pass with correct temperature dependence of the susceptibilities and the correction procedure with assumed linear temperature dependence of  $\chi$ . The medium is water.



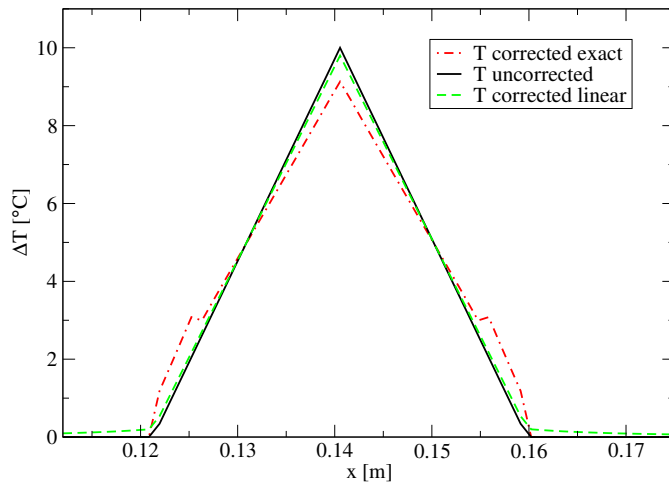


**Figure 5.6:** Comparison between the acquired temperature maps for a forward pass with correct temperature dependence of the susceptibilities, for the correction procedure with assumed linear temperature dependence of  $\chi$  and for the uncorrected case. The medium is water with an air-filled cylinder of radius 1.5 cm in the centre.

assumed value for  $\frac{\partial\chi}{\partial T} = -1.23 \cdot 10^{-9}(\text{°C})^{-1}$ . For comparison the corrected temperature map is calculated under consideration of the exact temperature dependence of  $\chi$ . Compared to the latter case, the temperature correction for the linear temperature dependence of  $\chi$  remains unchanged at approximately 2%. In contrast to that the exact calculation shows much higher deviations. Especially in the vicinity of the air-filled cylinder the corrections are of the order of 10%, which is not surprising due to the drastic susceptibility change. Obviously the assumption of  $\frac{\partial\chi}{\partial T} = \text{const}$  is not applicable to air (2.8.9) and leads to a noticeable underestimation of the resulting temperature which is not negligible.

The applied tests also prove that both field deviations and the temperature dependence of the susceptibility have to be considered if we want to determine temperature maps with high accuracy.

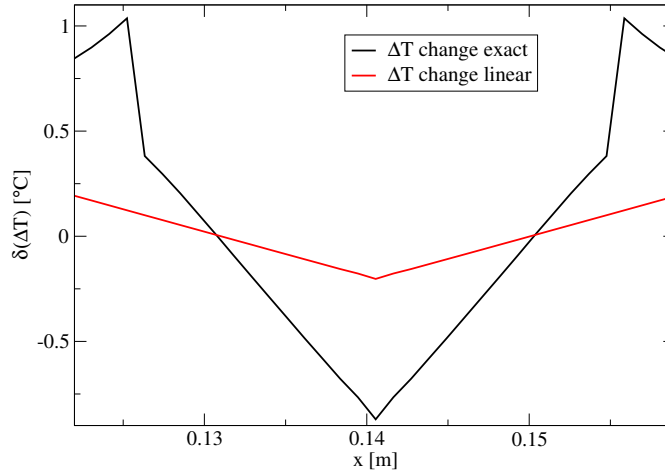


**Figure 5.7:** Difference between corrected and uncorrected temperature differences  $\delta(\Delta T)$  for the forward pass with correct temperature dependence of the susceptibilities and the correction procedure with assumed linear temperature dependence of  $\chi$ . The medium is water with an air-filled cylinder of radius 1.5 cm in the centre.

### 5.2.2 Application to experimental data

The effects of magnetic field inhomogeneities on temperature maps have been derived in Sect. (2.8) and the proposed correction procedure was validated for simple test cases in the previous section. Furthermore, the comparison between experimentally acquired temperature maps and measured temperatures showed deviations in the range of 12–20% (4.3.3). Consequently, it is still to be shown whether the correction for magnetic field inhomogeneities can remove the remaining deviations. For this purpose we use the acquired data already presented in Sect. (4.3.3) and concentrate on the temperature map acquired after 70min of cooling. As a first step, the correction procedure will be applied in a forward pass to observe the development of the correct measured temperatures in comparison to the calculated temperature maps (Fig. 5.8).

Obviously, this correction alone is not able to remove the present deviations between measurements and calculations. Rather, the correction leads to an increased temperature whereas the calculated temperatures underestimate the true temperature. On the other hand, it was discovered that the main source of temperature deviations arises from a temperature dependent drift of the main magnetic field. Of course this effect is difficult to characterise and should be corrected properly as proposed in [14]. There fatty reference areas are used for drift correction as the proton resonance frequency of fat is insensitive to temperature changes. Consequently the visible shifts are only an effect of the main magnetic field drift. Also without this somehow complicated procedure an estimate of the resulting shift can help to clarify whether this is the source of the observed temperature errors. For this purpose we assume a magnetic field drift of  $B_D = 8 \cdot 10^{-9} \text{ T m}^{-1} \text{ K}^{-1}$  which leads to a reasonable field change of  $\Delta B_D = 2 \cdot 10^{-7} \text{ T}$  in the centre of the magnet bore. This is also comparable with the magnitude of the magnetic field inhomogeneities

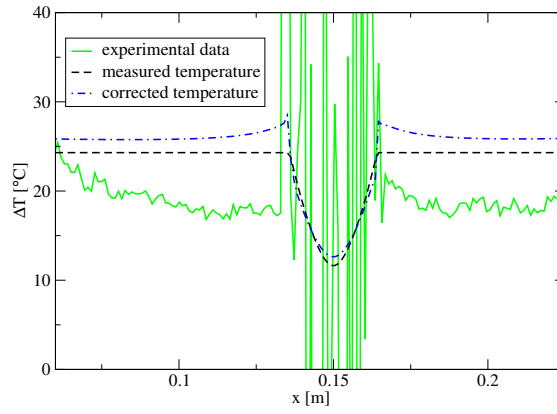


**Figure 5.8:** Comparison between measured temperatures, calculated temperatures and the simulated disturbed temperatures based on a forward pass.

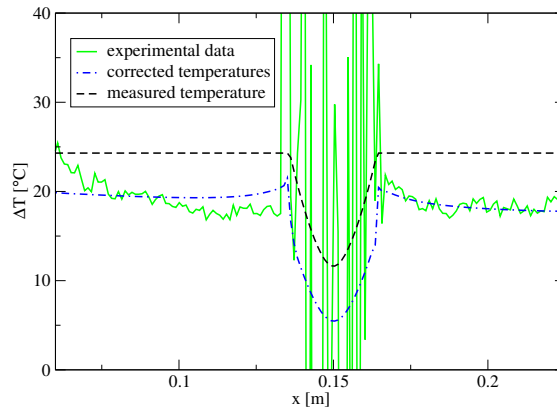


**Figure 5.9:** Comparison between measured temperatures, calculated temperatures and the simulated disturbed temperatures based on a forward pass including a magnetic field drift of  $8 \cdot 10^{-9} \text{ Tm}^{-1} \text{ K}^{-1}$ .

being in the order of  $(10^{-7} - 10^{-6}) \text{ T}$ . The achieved results in Fig. 5.9 demonstrate that the magnitude of the calculated temperature is reproducible if we consider both magnetic field deviations due to susceptibility changes and the temperature dependent magnetic field drift.



## 6 Conclusions

In this work, the main effects leading to image artifacts in magnetic resonance imaging as well as possible correction procedures, especially concerning magnetic resonance temperature imaging, have been investigated. The experimental methods have been described concerning both basic technical details as well as evaluations of the acquired data. For the application of MR temperature monitoring in the clinical practice, it has been shown that the quality of the acquired temperature information is not deteriorated by a smaller image resolution within reasonable limits. This can be used to shorten the acquisition times and hence to improve the temporal resolution of the time series. Furthermore, no evidence for the temperature dependence of the artifact size could be found. However, the matching between the present and the reference image is a crucial factor being very sensitive to inter-acquisitional motion. The comparison of temperature maps acquired with the proton resonance frequency method with temperatures measured with temperature probes showed large deviations which can be explained by a temperature-induced drift of the main magnetic field and the influence of susceptibility induced magnetic field inhomogeneities.

This knowledge about the causes and effects of image artifacts was applied to develop different correction procedures. As the magnitude of the magnetic field inhomogeneities is a crucial point within all these procedures, the main emphasis was on the search for both effective and precise determination methods of these magnetic field inhomogeneities. Two major directions were followed of which the first one relies on experimentally acquired phase images to extract the field deviations. As this procedure requires phase unwrapping, an algorithm was developed which was especially tailored for the given problem of phantoms with air-fillings. The second approach applies numerical techniques to solve Laplace's equation. Here, two different methods, namely the Fourier transform method and the finite volume method, were applied and benchmarked for accuracy and performance. The Fourier transform technique was shown to be superior in both aspects thus being the ideal approach for the numerical determination of the magnetic field inhomogeneities. It allows for online calculation and correction of image artifacts within a reasonable time. Its drawback is that it requires the knowledge of the exact susceptibility distribution within the body, which is difficult to determine. However, for moderate accuracy a discrimination between tissue and air is sufficient [35].

Based on the knowledge of the magnetic field inhomogeneities two different procedures for the correction of geometric distortions were developed. The application to distorted images revealed the advantages of the correction in the spatial domain compared to the algorithm working in the frequency domain. While the second procedure could not improve the image quality despite the long computing times the spatial correction was able to recover the basic geometry of the disturbed object very fast. Nevertheless, the

reconstruction of the image intensity remains difficult, being an inverse problem. For the application to surgical treatment planning, this is already sufficient as the main emphasis is on the definition of the geometries within the body.

As the geometrical distortions are less pronounced for air-filled cavities, the direct influence of magnetic field inhomogeneities on temperature maps was studied more closely yielding a possible correction procedure. The applied procedure works only in a homogeneous medium with magnetic properties similar to that of water. Applications to cases with large susceptibility differences such as air-water could not reproduce the correct temperature development. The forward application of the exact algorithm to measured temperature data in combination with an estimated magnetic field drift term was able to recover the results acquired in temperature measurements with the proton resonance frequency method. Even though the exact temperature profile could not be simulated, the absolute temperature range was in good agreement with the experimental data.

In conclusion, we can state that the developed techniques are able to improve the image quality and the accuracy of temperature measurements. Further improvements are possible by various means. As already mentioned, the precise definition of the object geometry for the numerical calculation of the magnetic field inhomogeneities is crucial but also difficult. This problem can be solved by the acquisition of an additional image with high readout bandwidth and hence less distortions. This decreases the signal-to-noise-ratio but helps to identify the basic structure of the imaged object. One method which is completely free of susceptibility induced distortions is computer tomography which delivers very precise information about the shape of the objects. We have proposed an experimental and numerical approach to determine the magnetic field deviation, both of which have their advantages and disadvantages. A combination of both, using the experimental acquired phase maps as input for the numerical solution seems promising. For severe distortions an iteration scheme is possible, but computational costly.

Apart from this, the problem concerning the mismatching between the actual and the reference image during a time temperature series remains, depending mainly on inter-acquisitional motion of the imaged object. An online motion correction is possible for instance by using an image catalogue in which the whole spectrum of motion present in the imaged object is covered. During the temperature measurements the actual image is compared with this catalogue, searching for the best reference image. As this is done online no additional post-processing is required.

The final results of this work demonstrate that the combined application of analytical, experimental and numerical techniques is very powerful and allows for the development of correction procedures for MR image artifacts.

# A Determination of the magnetic field at the position of the nucleus for simple geometries

For the magnetic field at the location of the nucleus (2.7.1) and (2.7.2) are valid

$$\begin{aligned}
 \vec{B}_{\text{nuc}}(\vec{r}) &= \vec{B}_{\text{ext}}(\vec{r}) + \vec{B}_{\text{scr}}(\vec{r}) + \vec{B}_{\text{lor}}(\vec{r}) \\
 &= \mu_0 (1 + \chi(\vec{r})) \left( \vec{H}_0(\vec{r}) + \vec{h}_{\text{in}}(\vec{r}) + \vec{h}_{\text{obj}}(\vec{r}) \right) + \vec{B}_{\text{scr}}(\vec{r}) + \vec{B}_{\text{lor}}(\vec{r}) \\
 &= \vec{B}_0(\vec{r}) + \vec{b}_{\text{in}}(\vec{r}) + \vec{b}_{\text{obj}}(\vec{r}) + \vec{B}_{\text{scr}}(\vec{r}) + \vec{B}_{\text{lor}}(\vec{r})
 \end{aligned} \tag{A.0.1}$$

with  $\vec{b}_{\text{in}}(\vec{r}) = \mu_0 (1 + \chi(\vec{r})) \vec{h}_{\text{in}}(\vec{r})$  and  $\vec{b}_{\text{obj}}(\vec{r}) = \mu_0 (1 + \chi(\vec{r})) \vec{h}_{\text{obj}}(\vec{r})$ .

## A.1 Homogeneous sphere

Laplace's equation will now be solved for a sphere (radius  $a$ , permeability  $\mu_i$  and susceptibility  $\chi_i$ ) in a surrounding medium of permeability  $\mu_e$  and susceptibility  $\chi_e$  (Fig. A.1) according to [30] and [11]. The external field is given by  $\vec{B}_0 = (0, 0, B_0)$ . As known from magnetostatics [21]

$$\vec{B}_{\text{ext}}(\vec{r}) = \mu_0 (\vec{H}_{\text{ext}}(\vec{r}) + \vec{M}(\vec{r}))$$

As  $\vec{M}(\vec{r})$  is constant within the cylinder, we can define a magnetostatic potential  $\vec{H}_{\text{ext}}(\vec{r}) = -\vec{\nabla}\Phi_m(\vec{r})$  so that

$$\vec{\Delta}\Phi_m(\vec{r}) = -\vec{\nabla} \cdot \vec{M}(\vec{r}) \tag{A.1.1}$$

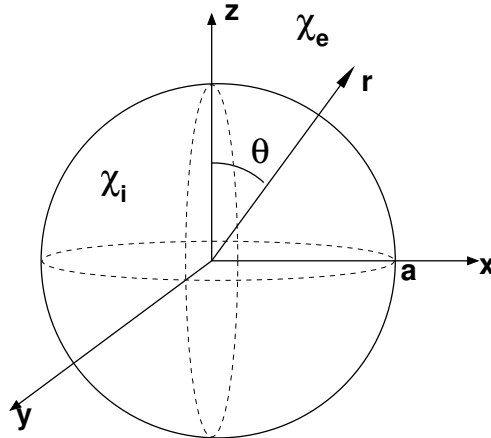


**Figure A.1:** Geometry of the posed problem. A sphere of susceptibility  $\chi_i$  and radius  $a$  is surrounded by air ( $\chi_e \approx 0$ ).

This can be solved by multipole expansion where the indices  $i$  and  $e$  denote the inner

and outer solutions

$$\Phi_{m,i}(\vec{r}) = \sum_{l=0}^{\infty} \left( A_l r^l + B_l r^{-(l+1)} \right) P_l(\cos \theta) \quad (\text{A.1.2})$$

$$\Phi_{m,e}(\vec{r}) = \sum_{l=0}^{\infty} \left( C_l r^l + D_l r^{-(l+1)} \right) P_l(\cos \theta) \quad (\text{A.1.3})$$

Now we have to consider certain boundary conditions for our solution

1. The solution at infinity can be approximated by the undisturbed case given by

$$\begin{aligned} \lim_{r \rightarrow \infty} \vec{B}_{\text{ext},i}(\vec{r}) &= \vec{B}_0 \\ \lim_{r \rightarrow \infty} \Phi_{m,e}(\vec{r}) &= -\frac{B_0}{\mu_0 \mu_e} z = \frac{B_0}{\mu_0 \mu_e} r \cos \theta \end{aligned} \quad (\text{A.1.4})$$

Thus 
$$C_l = \begin{cases} -\frac{B_0}{\mu_0 \mu_e} & , (l = 1) \\ 0 & , (l \neq 1) \end{cases}$$

2. The solution has to be regular for  $r \rightarrow 0$ . Consequently,  $B_l = 0$  holds for all  $l$ .
3. The normal component of  $\vec{B}(\vec{r})$  has to be continuous at the surface, that means

$$\begin{aligned} -\mu_i \frac{\partial \Phi_{m,i}(\vec{r})}{\partial r} \Big|_{r=a} &= -\mu_e \frac{\partial \Phi_{m,e}(\vec{r})}{\partial r} \Big|_{r=a} \\ -\mu_i \sum_{l=0}^{\infty} A_l l a^{l-1} P_l(\cos \theta) &= \mu_e \sum_{l=0}^{\infty} D_l (l+1) a^{-(l+2)} P_l(\cos \theta) - \frac{B_0}{\mu_0} \\ \mu_i A_1 &= \mu_e \left( -\frac{B_0}{\mu_0 \mu_e} - \frac{2D_1}{R^3} \right) \quad (A_1 = D_1 = 0 \forall l \neq 1) \end{aligned} \quad (\text{A.1.5})$$

4. The tangential component of  $\vec{H}(\vec{r})$  has to be continuous leading to

$$\begin{aligned} -\frac{1}{a} \frac{\partial \Phi_{m,i}(\vec{r})}{\partial \theta} \Big|_{r=a} &= -\frac{1}{a} \frac{\partial \Phi_{m,e}(\vec{r})}{\partial \theta} \Big|_{r=a} \\ -\frac{1}{a} \sum_{l=0}^{\infty} A_l a^l &= -\frac{1}{a} \sum_{l=0}^{\infty} C_l a^l + D_1 a^{-(l+1)} = \frac{B_0}{\mu_0 \mu_e} - \sum_{l=0}^{\infty} D_l a^{-(l+2)} \\ A_1 &= -\frac{B_0}{\mu_0 \mu_e} + \frac{D_1}{R^3} \quad (A_1 = D_1 = 0 \forall l \neq 1) \end{aligned} \quad (\text{A.1.6})$$

From (A.1.5) and (A.1.6) follows

$$D_1 = \frac{B_0(\mu_i - \mu_e)a^3}{\mu_0 \mu_e (2\mu_e + \mu_i)} \quad (\text{A.1.7})$$

$$A_1 = -\frac{B_0}{\mu_0 \mu_e} \left( 1 + \frac{\mu_e - \mu_i}{2\mu_e + \mu_i} \right) = -\frac{B_0}{\mu_0 \mu_e} \frac{3\mu_e}{2\mu_e + \mu_i} \quad (\text{A.1.8})$$



Together with (A.1.7) and (A.1.8) we can now derive the expression for the magnetostatic potential.

$$\Phi_{\text{m,i}}(\vec{r}) = - \left( \frac{3\mu_e}{2\mu_e + \mu_i} \right) \frac{B_0}{\mu_0\mu_e} r \cos \theta = - \left( \frac{3\mu_e}{2\mu_e + \mu_i} \right) \frac{B_0}{\mu_0\mu_e} z \quad (\text{A.1.9})$$

$$\begin{aligned} \Phi_{\text{m,e}}(\vec{r}) &= - \frac{B_0}{\mu_0\mu_e} r \cos \theta + \left( \frac{\mu_i - \mu_e}{\mu_i + 2\mu_e} \right) \frac{B_0 a^3}{\mu_0\mu_e r^2} \cos \theta \\ &= - \frac{B_0}{\mu_0\mu_e} z + \left( \frac{\mu_i - \mu_e}{\mu_i + 2\mu_e} \right) \frac{B_0}{\mu_0\mu_e} a^3 \frac{z}{r^3} \end{aligned} \quad (\text{A.1.10})$$

The magnetic induction inside and outside the sphere is given by the definition of the magnetostatic potential  $\vec{B}_{\text{ext,i}}(\vec{r}) = -\mu_0\mu\vec{\nabla} \cdot \Phi_{\text{m,i}}$ ,  $\vec{B}_{\text{ext,e}}(\vec{r}) = -\mu_0\mu\vec{\nabla} \cdot \Phi_{\text{m,e}}$ .

$$\begin{aligned} (B_{\text{ext,i}})_x &= 0 \\ (B_{\text{ext,i}})_y &= 0 \\ (B_{\text{ext,i}})_z &= B_0 \frac{3\mu_i}{2\mu_e + \mu_i} \\ (B_{\text{ext,e}})_x &= -B_0 \frac{\mu_e - \mu_i}{\mu_i + 2\mu_e} a^3 \frac{xz}{r^5} \\ (B_{\text{ext,e}})_y &= -B_0 \frac{\mu_e - \mu_i}{\mu_i + 2\mu_e} a^3 \frac{yz}{r^5} \\ (B_{\text{ext,e}})_z &= B_0 \left( 1 - \frac{\mu_e - \mu_i}{\mu_i + 2\mu_e} a^3 \frac{2z^2 - x^2 - y^2}{r^5} \right) \end{aligned} \quad (\text{A.1.11})$$

According to (A.0.1) the final solution for the field at the location of the nucleus including the results of (A.1.11) is given by

$$\begin{aligned} (B_{\text{nuc,i}})_x &= (b_{\text{in}})_x \\ (B_{\text{nuc,i}})_y &= (b_{\text{in}})_y \\ (B_{\text{nuc,i}})_z &= B_0 \frac{3\mu_i}{2\mu_e + \mu_i} + (b_{\text{in}})_z - B_0 \left( \sigma + \frac{2}{3}(\mu_i - 1) \right) \\ (B_{\text{nuc,e}})_x &= -B_0 \frac{\mu_e - \mu_i}{\mu_i + 2\mu_e} a^3 \frac{xz}{r^5} + (b_{\text{in}})_x \\ (B_{\text{nuc,e}})_y &= -B_0 \frac{\mu_e - \mu_i}{\mu_i + 2\mu_e} a^3 \frac{yz}{r^5} + (b_{\text{in}})_y \\ (B_{\text{nuc,e}})_z &= B_0 \left( 1 - \frac{\mu_e - \mu_i}{\mu_i + 2\mu_e} a^3 \frac{2z^2 - x^2 - y^2}{r^5} \right) + (b_{\text{in}})_z - B_0 \left( \sigma + \frac{2}{3}(\mu_e - 1) \right) \end{aligned} \quad (\text{A.1.12})$$

## A.2 Homogeneous cylinder

In the case of a homogeneously cylinder with a  $\ll L$  and susceptibility  $\chi_i$  in a medium of susceptibility  $\chi_e$  (Fig. A.2) we can distinguish between two major geometrical settings. For the external magnetic field parallel to the axis of the cylinder ( $\vec{B}_0(\vec{r}) = (0, 0, B_0)$ ), corresponding to  $\theta = 0$ , we can deduce the following very simple solutions for the resulting field [11]:

$$\begin{aligned}\vec{B}_{\text{ext},e}(\vec{r}) &= (1 + \chi_e)B_0\vec{e}_z + \vec{b}_{\text{in}}(\vec{r}), \\ \vec{B}_{\text{ext},i}(\vec{r}) &= (1 + \chi_i)B_0\vec{e}_z + \vec{b}_{\text{in}}(\vec{r}).\end{aligned}$$

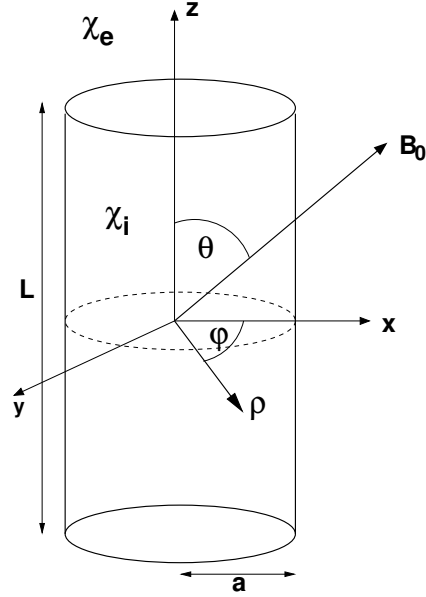


Figure A.2

According to (A.0.1) we can derive the total magnetic field felt by the nucleus.

$$\begin{aligned}(B_{\text{nuc},i})_x &= (b_{\text{in}})_x \\ (B_{\text{nuc},i})_y &= (b_{\text{in}})_y \\ (B_{\text{nuc},i})_z &= (1 + \chi_i)B_0 + (b_{\text{in}})_z - B_0 \left( \sigma + \frac{2}{3}\chi_i \right) \\ (B_{\text{nuc},e})_x &= (b_{\text{in}})_x \\ (B_{\text{nuc},e})_y &= (b_{\text{in}})_y \\ (B_{\text{nuc},e})_z &= (1 + \chi_e)B_0 + (b_{\text{in}})_z - B_0 \left( \sigma + \frac{2}{3}\chi_e \right)\end{aligned}\tag{A.2.1}$$

If we consider the case with the external magnetic field perpendicular to the axis of the cylinder ( $\vec{B}_0(\vec{r}) = (B_0, 0, 0)$ ), corresponding to  $\theta = \pi/2$ , the solution requires a more general ansatz. That is why we will now go back to the solution of Laplace's equation in cylindrical coordinates [39].

### Solution of Laplace's equation in cylindrical coordinates

In cylindrical coordinates the Laplace equation reads:

$$\vec{\Delta}\Phi(\vec{r}) = \frac{1}{\rho} \frac{\partial}{\partial \rho} \left( \rho \frac{\partial \Phi(\vec{r})}{\partial \rho} \right) + \frac{1}{\rho^2} \frac{\partial^2 \Phi(\vec{r})}{\partial \varphi^2} + \frac{\partial^2 \Phi(\vec{r})}{\partial z^2} = 0. \quad (\text{A.2.2})$$

Separation of variables leads to the expression  $\Phi(\rho, \varphi, z) = R(\rho)Q(\varphi)Z(z)$ . Assuming the functional dependencies

$$Q(\varphi) \sim e^{\pm i n \varphi} \quad (n = 0, 1, 2, \dots) \quad (\text{A.2.3})$$

$$Z(z) \sim e^{kz} \quad (\text{A.2.4})$$

allows for the derivation of an differential equation for  $R(\rho)$

$$\rho \frac{d}{d\rho} \left( \rho \frac{dR}{d\rho} \right) + (k^2 \rho^2 - n^2) R = 0. \quad (\text{A.2.5})$$

In the general case the solution of these equations is given by Bessel- and Neumann-functions  $R_n(k\rho) = A_n J_n(k\rho) + B_n N_n(k\rho)$ , where  $J_n$  is the Bessel-function of  $n^{\text{th}}$  order and  $N_n$  the Neumann-function of  $n^{\text{th}}$  order. Thus we get

$$\Phi(r, \varphi, z) \sim \sum_{m,n} [A_{mn} J_n(k_{mr}) + B_{mn} N_n(k_{mr})] e^{\pm i n \varphi} e^{\pm k_m z}. \quad (\text{A.2.6})$$

In the case of cylindrical symmetry the solution has to be independent of  $z$  and we get  $k = 0$ . Thus, (A.2.5) simplifies to

$$\rho \frac{d}{d\rho} \left( \rho \frac{dR}{d\rho} \right) - n^2 R = 0.$$

A separate treatment of the term with  $n = 0$  yields expressions for  $R_n(\rho)$  and  $Q_n(\varphi)$

$$R_n(\rho) = \begin{cases} A_0 + B_0 \ln \rho & , \quad (n=0) \\ A_n \rho^n + B_n \frac{1}{\rho^n} & , \quad (n=1,2,3,\dots) \end{cases}$$

$$Q_n(\varphi) = \begin{cases} C_0 [+D_0 \varphi] & , \quad (n=0) \\ C_n \cos n\varphi + D_n \sin n\varphi & , \quad (n=1,2,3,\dots) \end{cases}$$

The final solution for the magnetostatic potential is defined by the cylindrical harmonics

$$\Phi(r, \varphi) = A_0 + B_0 \ln \rho + \sum_{n=1}^{\infty} \left[ A_n \rho^n + B_n \frac{1}{\rho^n} \right] [C_n \cos n\varphi + D_n \sin n\varphi]. \quad (\text{A.2.7})$$

Now we are able to find the solution for the perpendicular case [30]. Again we have to consider the boundary conditions from Sect. A.1.

• 1:

$$\begin{aligned}\Phi_i(\vec{r}) &= \sum_{n=0}^{\infty} [C_n \rho^n \cos(n\varphi) + E_n \rho^n \sin(n\varphi)] \\ \Phi_e(\vec{r}) &= \sum_{n=0}^{\infty} [D_n \rho^{-n} \cos(n\varphi) + F_n \rho^{-n} \sin(n\varphi)] - \frac{B_0}{\mu_0 \mu_e} \rho \cos \varphi\end{aligned}\quad (\text{A.2.8})$$

• 3:

$$\begin{aligned}-\mu_0 \mu_i \left. \frac{\partial \Phi_i(\vec{r})}{\partial \rho} \right|_{\rho=a} &= -\mu_0 \mu_e \left. \frac{\partial \Phi_e(\vec{r})}{\partial \rho} \right|_{\rho=a} \\ -\mu_0 \mu_i (C_1 \cos \varphi + E_1 \sin \varphi) &= \mu_0 \mu_e (D_1 a^{-2} \cos \varphi - F_1 a^{-2} \sin \varphi) + B_0 \cos \varphi\end{aligned}\quad (\text{A.2.9})$$

• 4:

$$\begin{aligned}\left. \frac{\partial \Phi_i(\vec{r})}{\partial \varphi} \right|_{\rho=a} &= \left. \frac{\partial \Phi_e(\vec{r})}{\partial \varphi} \right|_{\rho=a} \\ -C_1 a \sin \varphi + E_1 a \cos \varphi &= -D_1 a^{-1} \sin \varphi + F_1 a^{-1} \cos \varphi + \frac{B_0}{\mu_0 \mu_e} a \sin \varphi\end{aligned}\quad (\text{A.2.10})$$

It follows that  $E_1 = F_1 = 0$  and with (A.2.9) and (A.2.10) we finally get

$$C_1 = -\frac{2B_0}{\mu_0(\mu_i + \mu_e)}, \quad D_1 = \frac{B_0 a^2 (\mu_i - \mu_e)}{\mu_0 \mu_e (\mu_e + \mu_i)}.\quad (\text{A.2.11})$$

That leads to an expression for the magnetostatic potential with  $x = \rho \cos \varphi$  and  $y = \rho \sin \varphi$

$$\begin{aligned}\Phi_i(\vec{r}) &= C_1 \rho \cos \varphi = -\frac{2B_0}{\mu_0(\mu_i + \mu_e)} \rho \cos \varphi = -\frac{2B_0}{\mu_0(\mu_i + \mu_e)} x \\ \Phi_e(\vec{r}) &= D_1 \frac{\cos \varphi}{\rho} - B_0 \rho \cos \varphi = \frac{B_0}{\mu_0 \mu_e} \left( \frac{\mu_i - \mu_e}{\mu_i + \mu_e} a^2 \frac{\cos \varphi}{\rho} - \rho \cos \varphi \right) \\ &= \frac{B_0}{\mu_0 \mu_e} \left( \frac{\mu_i - \mu_e}{\mu_i + \mu_e} a^2 \frac{x}{x^2 + y^2} - x \right).\end{aligned}\quad (\text{A.2.12})$$

The final solution for inside  $\vec{B}_{\text{ext},i}$  and outside the cylinder  $\vec{B}_{\text{ext},e}$  can be found by applying the definition of the magnetostatic potential

$$\begin{aligned}
(B_{\text{ext},i})_x &= \frac{2\mu_i}{\mu_i + \mu_e} B_0 + (b_{\text{in}})_x \\
(B_{\text{ext},i})_y &= (b_{\text{in}})_y \\
(B_{\text{ext},i})_z &= (b_{\text{in}})_z \\
(B_{\text{ext},e})_x &= B_0 - B_0 a^2 \frac{(\mu_i - \mu_e)}{(\mu_i + \mu_e)} \frac{(y^2 - x^2)}{\rho^4} + (b_{\text{in}})_x \\
(B_{\text{ext},e})_y &= B_0 a^2 \frac{(\mu_i - \mu_e)}{(\mu_i + \mu_e)} \frac{2xy}{\rho^4} + (b_{\text{in}})_y \\
(B_{\text{ext},e})_z &= (b_{\text{in}})_z \quad .
\end{aligned} \tag{A.2.13}$$

The result can be seen as a superposition of the fields with and without the cylinder placed in the medium with susceptibility  $\chi_e$ . The latter was calculated by solving Laplace's equation.

$$\vec{B}_{\text{ext}}(\vec{r}) = (1 + \chi_e) \vec{B}_0(\vec{r}) + \vec{B}_{\text{cyl}}(\vec{r})$$

Following this ansatz combined with (A.0.1) we obtain the total field present at the location of the considered nucleus including the effect of the sphere of Lorentz.

$$\begin{aligned}
(B_{\text{nuc},i})_x &= B_0 + \frac{3\chi_e - \chi_i + 2\chi_i\chi_e}{6 + 3\chi_i + 3\chi_e} B_0 - B_0\sigma + (b_{\text{in}})_x \\
(B_{\text{nuc},i})_y &= (b_{\text{in}})_y \\
(B_{\text{nuc},i})_z &= (b_{\text{in}})_z \\
(B_{\text{nuc},e})_x &= B_0 + B_0 a^2 \frac{(\chi_i - \chi_e)}{(2 + \chi_i + \chi_e)} \frac{(x^2 - y^2)}{\rho^4} + \frac{1}{3}\chi_e B_0 - B_0\sigma + (b_{\text{in}})_x \\
(B_{\text{nuc},e})_y &= B_0 a^2 \frac{(\chi_i - \chi_e)}{(2 + \chi_i + \chi_e)} \frac{2xy}{\rho^4} + (b_{\text{in}})_y \\
(B_{\text{nuc},e})_z &= (b_{\text{in}})_z \quad .
\end{aligned} \tag{A.2.14}$$



## B Gradients

For the correction methods mentioned in Sect. (3.6) the exact strength of the spatial encoding gradients have to be known. They were acquired with the help of the program IDEA provided by the manufacturer Siemens medical solutions which offers the possibility to simulate MR sequences including the gradient properties. Tables B.1 and B.2 show the resulting values for the gradients for different acquisition parameters including changing readout bandwidth to reduce susceptibility artifacts by increasing the readout gradient.

| FOV readout [mm] | FOV phase [%] | resolution | number of slices | slice thickness [mm] | R-grad [mT/m] | P-grad [mT/m] | S-grad [mT/m] |
|------------------|---------------|------------|------------------|----------------------|---------------|---------------|---------------|
| 400              | 50            | 256        | 16               | 8                    | $\pm 3.91$    | 5.33          | -5.28         |
| 400              | 50            | 128        | 16               | 8                    | $\pm 1.96$    | 2.76          | -7.54         |
| 400              | 68.8          | 256        | 16               | 8                    | $\pm 3.91$    | 5.33          | -5.28         |
| 400              | 68.8          | 128        | 16               | 8                    | $\pm 1.96$    | 2.76          | -7.54         |
| 280              | 75            | 256        | 16               | 8                    | $\pm 5.59$    | 8.45          | -5.28         |
| 280              | 75            | 128        | 16               | 8                    | $\pm 2.80$    | 4.16          | -7.54         |
| 280              | 50            | 256        | 21               | 10                   | $\pm 5.59$    | 8.45          | -4.23         |
| 280              | 50            | 128        | 21               | 10                   | $\pm 2.80$    | 4.16          | -6.03         |
| 300              | 100           | 256        | 16               | 5.5                  | $\pm 5.22$    | 7.11          | -7.69         |
| 300              | 100           | 128        | 16               | 5.5                  | $\pm 2.61$    | 3.68          | -10.96        |
| 300              | 68.8          | 256        | 16               | 5.5                  | $\pm 5.22$    | 7.11          | -7.69         |
| 300              | 68.8          | 192        | 16               | 5.5                  | $\pm 3.91$    | 5.49          | -10.96        |
| 300              | 68.8          | 128        | 16               | 5.5                  | $\pm 2.61$    | 3.68          | -10.96        |

**Table B.1:** Gradient strengths for all three encoding directions for different sequence parameters and a constant readout bandwidth of 260Hz/pixel.

| readout BW [Hz/pixel] | FOV readout [mm] | FOV phase [%] | matrix | number of slices | slice thickness [mm] | R-grad [mT/m] | P-grad [mT/m] | S-grad [mT/m] |
|-----------------------|------------------|---------------|--------|------------------|----------------------|---------------|---------------|---------------|
| 300                   | 280              | 68.8          | 256    | 16               | 8                    | -5.59/6.45    | -10.13/8.45   | -5.28/3.96    |
| 340                   | 280              | 68.8          | 256    | 16               | 8                    | -5.59/7.36    | -9.02/8.45    | -4.60/3.96    |
| 380                   | 280              | 68.8          | 256    | 16               | 8                    | -5.59/8.22    | -8.52/8.45    | -4.30/3.96    |
| 420                   | 280              | 68.8          | 256    | 16               | 8                    | -5.59/8.92    | -8.20/8.45    | -4.11/3.96    |
| 480                   | 280              | 68.8          | 256    | 16               | 8                    | -5.59/10.23   | -7.56/8.45    | -3.74/3.96    |
| 530                   | 280              | 68.8          | 256    | 16               | 8                    | -5.59/11.34   | -7.11/8.45    | -3.48/3.96    |
| 340                   | 400              | 50.0          | 256    | 16               | 8                    | -3.91/5.15    | -6.32/5.33    | -4.60/3.96    |
| 420                   | 400              | 50.0          | 256    | 16               | 8                    | -3.91/6.25    | -5.74/5.33    | -4.11/3.96    |
| 530                   | 400              | 50.0          | 256    | 16               | 8                    | -3.91/7.94    | -4.98/5.33    | -3.48/3.96    |

**Table B.2:** Gradient strengths for all three encoding directions for different sequence parameters and a changing readout bandwidth.





# Bibliography

- [1] S. Balac, H. Benoit-Cattin, T. Lamotte, and C. Odet. Analytic solution to boundary integral computation of susceptibility induced magnetic field inhomogeneities. *Math. Comp. Model.*, 39:437–455, 2004.
- [2] A. Bartholet, J. Goudemant, and S. Laurent. Spin transition molecular materials: intelligent contrast agents for magnetic resonance thermometry. *Proc. Int. Soc. Magn. Res. Med.*, 8, 2000.
- [3] C.T.W. Moonen B.D. De Senneville, B. Quesson. Magnetic resonance temperature imaging. *Int. J. Hyperthermia*, 21(6):515–531, 2005.
- [4] R. Bhagwandien, M.A. Moerland, C.J.G. Bakker, R. Beersma, and J.J.W. Lagendijk. Numerical analysis of the magnetic field for arbitrary magnetic susceptibility distributions in 3d. *Magn. Res. Im.*, 12:101–107, 1994.
- [5] S. Chavez, Q.-S. Xiang, and L. An. Understanding phase maps in MRI: A new cutline phase unwrapping method. *IEEE Trans. Med. Im.*, 21(8), 2002.
- [6] R.L. Levin D. Le Bihan, J. Delannoy. Temperature mapping with mr imaging of molecular diffusion:application to hyperthermia. *Radiology*, 43:901–904, 1989.
- [7] John de Poorter. Noninvasive mri thermometry with the proton resonance frequency method:study of susceptibility effects. *Magn. Res. Med.*, 34:359–367, 1995.
- [8] R.J. Dickenson, A.S. Hall, A.J. Hind, and I.R. Young. Measurement of changes in tissue temperature using MR imaging. *J. Comp. Assist. Tomogr.*, 10:468–472, 1986.
- [9] W.C. Dickenson. The time average magnetic field at the nucleus in nuclear magnetic resonance experiments. *Phys. Rev.*, 81:717–731, 1950.
- [10] I.S. Duff. *MA28-a set of FORTRAN subroutines for sparse unsymmetric linear equations*. Technical Report AERE R8730,HMSO, London, 1977.
- [11] E.M.Haacke, R.W. Brown, and R.Venkatesan M.R. Thompson. *Magnetic Resonance Imaging:Physical principles and sequence design*. Wiley and sons, New York, 1999.
- [12] R.P. Feynman, R.P. Leighton, and M. Sands. *The Feynman Lectures on Physics Vol.2*. Addison Wesley, 1975.
- [13] S. Fossheim, K. Il’yasov, and U. Wiggen. Paramagnetic liposomes as thermosensitive probes for mri in vitro feasibility studies. *Proc. Int. Soc. Magn. Res. Med.*, 7:725, 1999.

- [14] J. Gellermann, W. Wlodarczyk, A. Feussner, H. Faehling, J. Nadobny, B. Hildebrandt, R. Felix, and P. Wust. Methods and potentials of magnetic resonance imaging for monitoring radiofrequency hyperthermia in a hybrid system. *Int. J. Hyperthermia*, 21(6):497–513, 2005.
- [15] J. Gellermann, W. Wlodarczyk, H. Ganter, J. Nadobny, H. Faehling, M. Seebass, R. Felix, and P. Wust. A practical approach to thermography in a hyperthermia/magnetic resonance hybrid system: validation in a heterogeneous phantom. *I.J. Oncology, Biology, Physics*, 61(1), 2005.
- [16] J. Gellermann, W. Wlodarczyk, B. Hildebrandt, H. Ganter, A. Nicolau, B. Rau, W. Tilly, H. Faehling, J. Nadobny, R. Felix, and P. Wust. Noninvasive magnetic resonance thermography of recurrent rectal carcinoma in a 1.5 tesla hybrid system. *Cancer Research*, 65(13):58:72–80, 2005.
- [17] E.L. Hahn. Spin echoes. *Phys. Rev.*, 80:580–594, 1950.
- [18] A.S. Hall, P.V. Prior, I.R. Young, and R.J. Dickenson. Observation by MR imaging of in vivo temperature changes induced by radiofrequency hyperthermia. *J. Comp. Assist. Tomogr.*, 14:430–436, 1990.
- [19] J.C. Hindman. Proton resonance shift of water in the gas and liquid states. *J. Comp. Phys.*, 4(12), 1966.
- [20] <http://www.netlib.org>.
- [21] J.D. Jackson. *Classical Electrodynamics*. Wiley and sons, New York, 1998.
- [22] R. Bowtell J.P. Marques. Application of a fourier-based method for rapid calculation of field inhomogeneity due to spatial variation of magnetic susceptibility. *Conc. Magn. Res. B*, 25:65–78, 2005.
- [23] K.M. Koch, X. Papademetris, D.L. Rothman, and R.A. De Graaf. Rapid calculations of susceptibility-induced magnetostatic field perturbations for in vivo magnetic resonance. *Phys. Med. Biol.*, 51:6381–6402, 2006.
- [24] Antero Koivula. *Magnetic resonance image distortions due to artificial macroscopic objects*. PhD thesis, Department of Diagnostic Radiology, University of Oulu, Finland, 2002.
- [25] L. Li and Z.J. Wang. Magnetic susceptibility quantitation with mri by solving boundary value problems. *Med. Phys.*, 30(3)(No.3), 2003.
- [26] H.A. Lorentz. *The theory of Electrons and its application to the phenomena of light and heat*. New York:Dover, 1915.
- [27] K.M. Lüdeke, P. Röschmann, and R. Tischler. Susceptibility artefacts in NMR imaging. *J. Comp. Phys.*, 72(8):4429, 1980.

- [28] J.A. Den Boer M.T. Vlaardingerbroek. *Magnetic resonance Imaging*. Springer Verlag, Berlin/Heidelberg, 1996.
- [29] D.L. Parker. Applications of NMR in hypothermia: An evaluation of the potential for localized tissue heating and non-invasive temperature monitoring. *IEEE Trans. Eng. Biomed.*, 31:161, 1984.
- [30] J.M. Peeters. *Analysis and exploitation of field imperfections in magnetic resonance imaging*. PhD thesis, University of Utrecht, 2006.
- [31] R.D. Peters, R.S. Hinks, and R.M. Henkelman. Heat-source orientation and geometry dependence in proton-resonance frequency shift magnetic resonance thermometry. *Magn. Res. Med.*, 41:909–918, 1999.
- [32] J.S. Philo and W.M. Fairbank. Temperature dependence of the diamagnetism of water. *J. Comp. Phys.*, 72(8):4429, 1980.
- [33] M.D. Pritt and J.S. Shipman. Least-squares two-dimensional phase unwrapping using fft's. *IEEE Trans. Geosc. Rem. Sens.*, 32(3), 1994.
- [34] B. Quesson, J.A. de Zwart, and C.T.W. Moonen. Magnetic resonance temperature imaging for guidance of thermotherapy. *J. Magn. Res. Im. Ser.B*, 12:525–533, 2000.
- [35] R. Birgkart S. Burkhardt, A. Schweikard. Numerical determination of the susceptibility caused geometric distortions in mri. *Med. Image Anal.*, 7(3):221–236, 2003.
- [36] R. Salomir, B. D. de Senneville, and C.T.W. Moonen. A fast calculation method for magnetic field inhomogeneity due to an arbitrary distribution of bulk susceptibility. *Conc. Magn. Res. B*, 19B(1):26–34, 2003.
- [37] R. Salomir, J.A. De Zwart, F.C. Vimeux, B.Quesson, and C.T.W. Moonen. Temperature-induced changes in magnetic susceptibility in local hyperthermia:correction of mr thermometry. *Proc. Int. Soc. Magn. Res. Med.*, 8, 2000.
- [38] K. Sekihara, M. Kuroda, and H. Kohno. Image restoration from non-uniform magnetic field influence for direct fourier nmr imaging. *Phys. Med. Biol.*, 29:15–24, 1984.
- [39] Bo E. Sernelius. Laplace and poisson's equation. Linkoeeping Institute of Technology, Department of Physics, Lecture notes.
- [40] S.M.-H. Song, S. Napel, N.J. Pelc, and G.H. Glover. Phase unwrapping of MR phase images using poisson equation. *IEEE Trans. Im. Proc.*, 4(5), 1995.
- [41] H. Uetake, N. Hirota, J. Nakagawa, Y. Ikezoe, and K. Kitazawa. Thermal convection control by gradient magnetic field. *J. Appl. Physics*, 87(No.9), 2000.

- [42] J. Nadobny and W. Wlodarczyk, L. Westhoff, and J. Gellermann. A clinical water-coated antenna applicator for mr-controlled deep-body hyperthermia: A comparison of calculated and measured 3-d temperature data sets. *IEEE Trans. Eng. Biomed.*, 52(3), March 2005.
- [43] W. Wlodarczyk, M. Hentschel, P. Wust, R. Noeske, and N. Hosten. Comparison of four magnetic resonance methods for mapping small temperature changes. *Phys. Med. Biol.*, 44:607–624, 1999.
- [44] P. Wust, J. Gellermann, C. Harder, W. Tilly, B. Rau, S. Dinges, P. Schlag, V. Budach, and R. Felix. Rationale for using invasive thermometry for regional hyperthermia of pelvic tumors. *I.J. Oncology, Biology, Physics*, 41(5):1129–1137, 1998.
- [45] P. Wust, J. Gellermann, M. Seebass, H. Faehling, P. Turner, W. Wlodarczyk, J. Nadobny, B. Rau, B. Hildebrandt, A. Oppelt, P.M. Schlag, and R. Felix. Teilkörperhyperthermie mit einem radiofrequenz-multiantennen-applikator unter on-line kontrolle in einem 1,5 t mr-tomographen. *Fortschr Röntgenstr.*, 175:1–12, 2003.
- [46] L. Ying, Z.-P. Liang, D.C. Munson Jr., R. Koetter, and B.J. Frey. Unwrapping of MR phase images using a random field model. *IEEE Trans. Med. Im.*, 25(1), 2006.

# Acknowledgements

At the very end of this work I would like to express a word of gratitude to all the people who helped in one way or the other that this work came to an successful ending. First of all this concerns my supervisor Dr. Ralf Schneider who showed a lot of patience during our discussions and was always able to give the missing link. Furthermore I want to thank Dr. Johanna Gellermann from the university hospital Charité in Berlin for her support especially concerning the experimental work and her great ideas in the field of phantom design.

Also I am very grateful for the discussions with my boy friend who helped me to see the topic from an external point of view.

Finally, my thanks go to all group members both in Greifswald and in Berlin for always being helpful and patient and for giving useful hints concerning the final version of this work.



Name, Vorname: Hey, Silke  
geboren: 24.06.1983  
Matrikelnummer: 110672  
Korrespondenzanschrift: Kieselhausenstraße 3c, 09117 Chemnitz

Ernst-Moritz-Arndt Universität Greifswald  
Zentrales Prüfungsamt  
Rubenowstraße 2, 17487 Greifswald  
Bearbeiterin: Frau Sanne - 86-1288

### **Erklärung zur Diplomarbeit**

Ich versichere, dass ich die anliegende Diplomarbeit mit dem Thema:

**“Magnetic resonance imaging as an instrument for temperature measurements during cancer treatment”**

selbständig verfasst und keine anderen Hilfsmittel als die angegebenen verwendet habe. Die Stellen, die anderen Werken dem Wortlaut oder dem Sinne nach entnommen sind, habe ich in jedem Falle durch Angaben der Quelle, auch der Sekundärliteratur, als Entlehnung kenntlich gemacht.

Greifswald, 6. Juli 2007

Hey, Silke